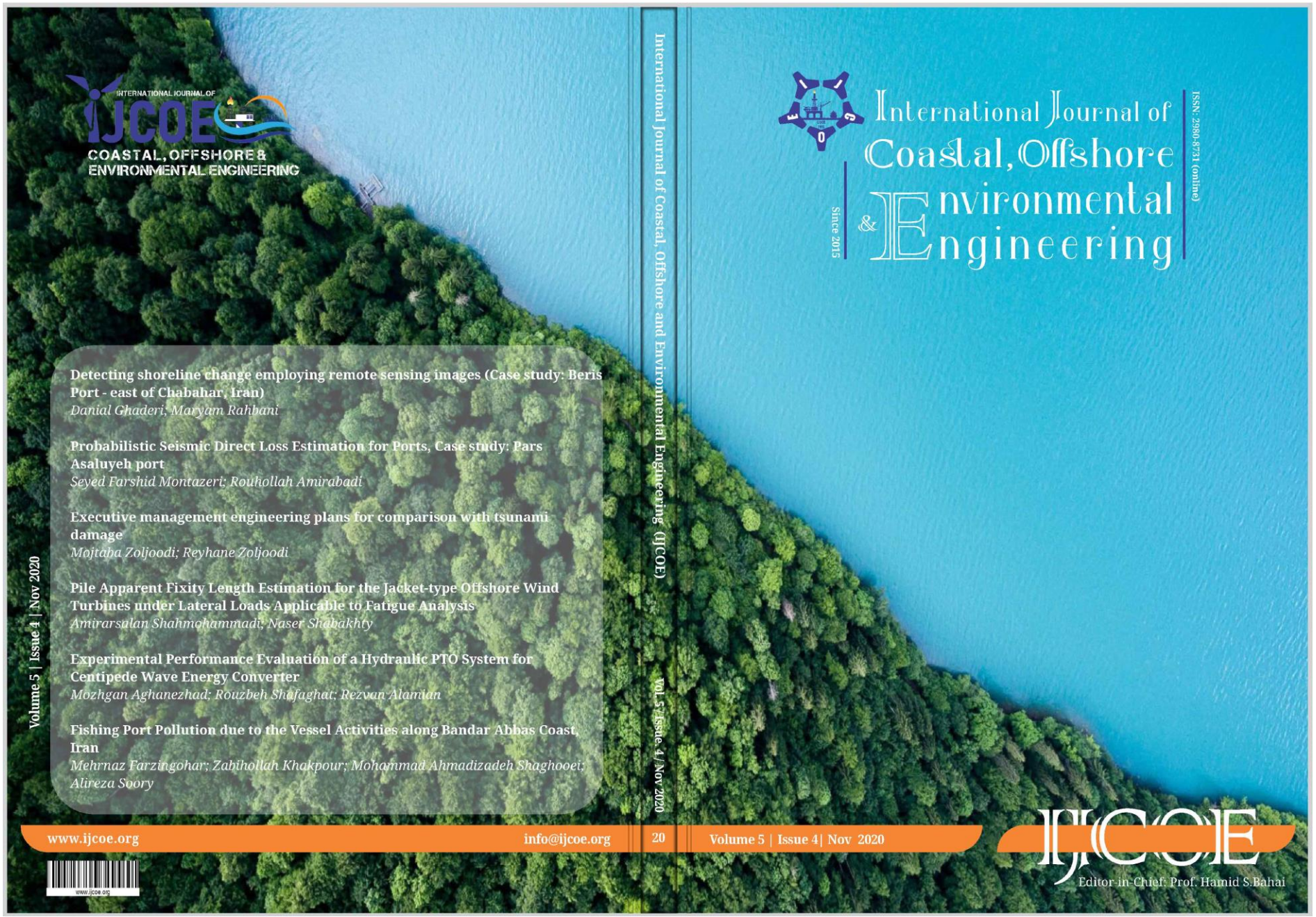

INTERNATIONAL JOURNAL OF
IJCOE
COASTAL, OFFSHORE & ENVIRONMENTAL ENGINEERING

Volume 5 | Issue 4 | Nov 2020

www.ijcoe.org info@ijcoe.org

International Journal of Coastal, Offshore and Environmental Engineering (IJCOE) Vol. 5 | Issue. 4 | Nov 2020

International Journal of
Coastal, Offshore & Environmental Engineering
Since 2015
ISSN: 2980-8731 (online)

Volume 5 | Issue 4| Nov 2020

IJCOE

Editor-in-Chief: Prof. Hamid S.Bahai

International Journal of Coastal, Offshore & Environmental Engineering
Since 2015
ISSN: 2980-8721 (online)

In The Name of God

Message from the Editor-in-Chief

The IJCOE journal office was established in 2015,and its first issue was published in 2016. TheIJCOE covers a wide range of research in thefields of oceanography & ocean technology, aswell as marine industries & marine engineering.The editorial board of IJCOE consists of nearly130 of the greatest scientists and researchersfrom over 30 countries worldwide, and thejournal's review board comprises 1,000 membersfrom all five continents. The membership andapplication process for joining the editorial andreview boards of this journal is ongoing. IJCOE isa research-academic quarterly journal that haspublication and distribution permissions fromthe Press Organization and permission topublish scientific-research articles from theMinistry of Science, Research, and Technology(MSRT) with an "A" rating. It also holds a "Q1"rating from the ISC institute with an impactfactor (IF) of approximately 0.43 and isconsidered a "core journal" (prestigious andoutstanding journal). IJCOE is an open-accessjournal and allows the download and receipt ofaccepted articles in full text for free. It respectsand adheres to copyright and COPE regulations.The journal's office operates 24/7, providingservices to researchers. In addition to publishinga regular quarterly journal, IJCOE has 16 specialissues on specific topics in preparation. It alsoprovides conditions for publishing specializedbooks, references, and handbooks. Moreover, itis ready to cooperate with the secretariats ofreputable international conferences to publishtheir selected and outstanding articles. IJCOEevaluates, appraises, and publishes books,articles, and the scientific achievements andfindings of esteemed researchers and scientistsworldwide who are innovating and conductingin-depth research in the "important and strategicfield of the maritime technology & Oceanengineering." It welcomes any form of jointcooperation with universities, research institutes,and related research centers at the national,regional, and international levels, and extends ahand for collaboration.

Classification of Editorial Board in IJCOE

Editor-in-Chief

Director-in-Chief

Deputy Editor

Executive Managers

English Text Editor

Technical Editor

International Editorial Board

National Editorial Board

Editorial Board Associate

Editorial Board Assistant

Guest Editorial Board

Advisory Board

Administrative Coordinator

Honorary Board Member

Methodology Advisor

Author Benefits

- Open Access
- Rapid Publication
- Thorough Peer-Review
- No Copyright Constraints
- Coverage by Leading Indexing Services
- Discounts On Article Processing Charges (APC)
- No Space Constraints, No restriction on the maximum length of the papers, number of figures or colors

INTERNATIONAL JOURNAL OF IJCOE COASTAL, OFFSHORE & ENVIRONMENTAL ENGINEERING

Aims of IJCOE

Hydrodynamics

Marine equipment

Structural mechanics

Ocean environmental predictions

Stochastic calculations Experimental

Automatic Control of Marine Systems

Scope of IJCOE

Marine Hazards

Ocean Acoustics

Naval Architecture

Ocean Engineering

Coastal Engineering

Marine Meteorology

Marine Earth Sciences

Underwater Technology

Marine Renewable Energy

Polar & Arctic Engineering

Marine Renewable Energy

Marine Geography & Geodesy

Marine Environmental Engineering

Automatic Control of Marine Systems

Hydro Physics & Physical Oceanography

Type of papers

- Case Studies
- Book Reviews
- Review Article
- Letters to the Editor
- Methodology Papers
- Editorials and Commentaries
- Response or Rejoinder Papers
- Perspective or Opinion Papers
- Conceptual or Theoretical Papers
- Meta-Analysis and Systematic Reviews
- Short Communications or Brief Reports
- Research Articles (Original Research Papers)

Scientific Research Journal

Ministry of Science, Research And Technology (MSRT)

Jurnal Ranking 2023: A

Ministry Of Science, Research And Technology (ISC)

Citation Impact 2022: 0.429

Quartile 2022 : Q1

Core Collection

IJCOE is a Member of

Cantact Us

Office 1 | Research Institute of Meteorology and Atmospheric Science

Address | Tehran, Shahid Kharrazi Highway, Pajoohesh Blvd, Research Institute of Meteorology and Atmospheric Science, Sand and Dust Storm International Research Center (SDS-IRC), No. 13, 1st floor.

Phone | +982144787652

Postal code | 13611-14977

website | www.rimac.ac.ir

Office 2 | Iranian National Institute for Oceanography and Atmospheric Science

Address | Tehran, Dr. Fatemi Gharbi St., Shahid Etemadzade St., No. 3, third floor.

Phone | +982166944873

Postal code | 13389 – 14118

website | www.inio.ac.ir

Email | Info@ijcoe.org

Website | www.ijcoe.org

Follow Us

www.ijcoe.org

INTERNATIONAL JOURNAL OF IJCOE COASTAL, OFFSHORE & ENVIRONMENTAL ENGINEERING

Volume & Issue:

Volume 5, Issue 4, November 2020

Number of Articles: 6

Content

INTERNATIONAL JOURNAL OF
COASTAL & OFFSHORE ENGINEERING
IJCOE Vol.5/No. 4/Winter 2020 (1-8)

Available online at: www. Ijcoe.org

Detecting shoreline change employing remote sensing images (Case study: Beris Port - east of Chabahar, Iran)

Danial Ghaderi [1], Maryam Rahbani [2*]

[1] Ph.D. student, Faculty of Marine Science and Technology, University of Hormozgan, Bandar Abbas 79131, Iran; danialghaderi.phd@hormozgan.ac.ir
[2] Associate Professor, Faculty of Marine Science and Technology, University of Hormozgan, Bandar Abbas 79131, Iran; maryamrahbani@yahoo.com*

ARTICLE INFO

Article History:
Received: 10 Apr. 2020
Accepted: 25 Jun. 2020

Keywords:
Beris Port
DSAS
remote sensing
shoreline change

ABSTRACT

Coastal areas are one of the most crucial and important area in each country. They are also one the most dynamics area, which undergo significant changes in relatively short periods. Protecting coastlines from erosion and/or sedimentation thus, is one of the most important duties in each country. In this study, shoreline change in the Beris Port - east of Chabahar, Iran, was investigated using remote sensing technique and DSAS tools. Beris Port is located 85 km east of Chabahar, on the Makran coast. Landsat 8 and 5 satellite images were used to detect shoreline change, due to the port's construction date, satellite imagery of 1988, 1990, 2014 and 2019 was used. Using the NSM, SCE, EPR and LRR statistical indexes of the DSAS tool, erosion and accretion rates were calculated in for the area. According to the LRR index, the lowest shoreline change rate is -1.51 m/year and is detected to be to the east of port. The highest rate of shoreline change is 7.44 m/year at the port. According the results, the main reason for this high rate of change is the location of the port, which is in the area perpendicular to its neighborhood coastal area, which causes to trap the current in this area to increase its dynamic activities. Shortly speaking, it was found that the accretion is dominant in port Beris and east of the port is the zone with least amount of accretion.

1. Introduction

Coastal areas are dynamic systems with relatively fragile feature. They are affected by many natural and human changes. The most important natural processes that change coastal morphology are, wave, wind, nearshore current, and tide [1,2]. Besides, human processes like coastal engineering activities could cause massive erosion and accretion on the coastal area. Constricting sea walls and breakwaters are those activities which cause the advancement of the shoreline artificially by land reclamation, and the removal of beach material from the coastline is an aspect of retreating coast [3].

Hence the management of coastal areas requires knowledge of the underlying processes of shoreline variability in the medium, inter-annual and decadal time scales [4]. Coastline change is considered one of the most dynamic processes in coastal area. It has become important to map the coastline change as an input data for coastal hazard assessment. Besides, it should be noted that coastal protection might conflict with current land use and economic development activities [5]. There are many change detection techniques currently in use [6]. Using remote sensing and satellite imagery is one of the low-cost and easy methods in coastline detection [7]. Van and Binh (2008), described an application of satellite remote sensing technology and GIS to detect and analyze the spatial changes as well as quantify the result of shoreline change in Cuu Long estuary. Van Cuong et al (2015) using the Shoreline Video Assessment Method (SVAM) applied by satellite images assessed the conditions of the mangrove forest and mainland coastline of the Kien Giang province. Maiti and Bhattacharya (2009), using remote sensing and satellite imagery, studied 113.5 km of coast adjacent to Bay of Bengal in eastern India, for the time interval of 1973 to 2003 [8]. Do et al (2018) used satellite-derived shorelines of NorthHolland coast. They studied the rate of shoreline change calculating volumes of coastal sediments. Nassar et al (2019) recorded shoreline change along the North Sinai coast in Egypt using

geographic information system and digital shoreline analysis system (DSAS) during the elapsed period from 1989 to 2016 [9].

East of Chabahar coastal zone is an important area, and is used for various activities as transportation, fishing and commercial activities, specifically in Beris port. This port, located in southeast of Iran, 85 km east of Chabahar, is one example of the ports constructed in a crenulate-shaped bay. The construction of Beris Fishery Port was finished in 1994. The port has a basin of 25 ha area [10]. The port is suffering from two mechanisms of sedimentation, that is, sedimentation at the head of the main breakwater and remarkable change of shoreline position at the back of the secondary breakwater [11,9]. In addition, construction of the port caused the coastline undergoes significant changes.

In this research, using satellite images and remote sensing, the shoreline is detected and the rate of shoreline change is calculated using the Digital Shoreline Analysis System (DSAS) technique [12].

2. Materials and methods

2.1 Study area

Area under investigation is located east of Chabahar coast, southeast of Iran, along the northern coasts of the Gulf of Oman. Main focus of this study is on the Beris fishery port at 25.147° N latitude and 61.176° E longitude (Figure 1), This fishing port is located 85 km east of Chabahar [10]. Since the study area is quite long, it was considered to divide it into three adjacent zones of A, B and C, they are shown in Figure 1 as parts A, B and C respectively. Zone A is in the western of the Beris port, Zone B is at the middle and contains Beris port, and Zone C is in the eastern of the port.

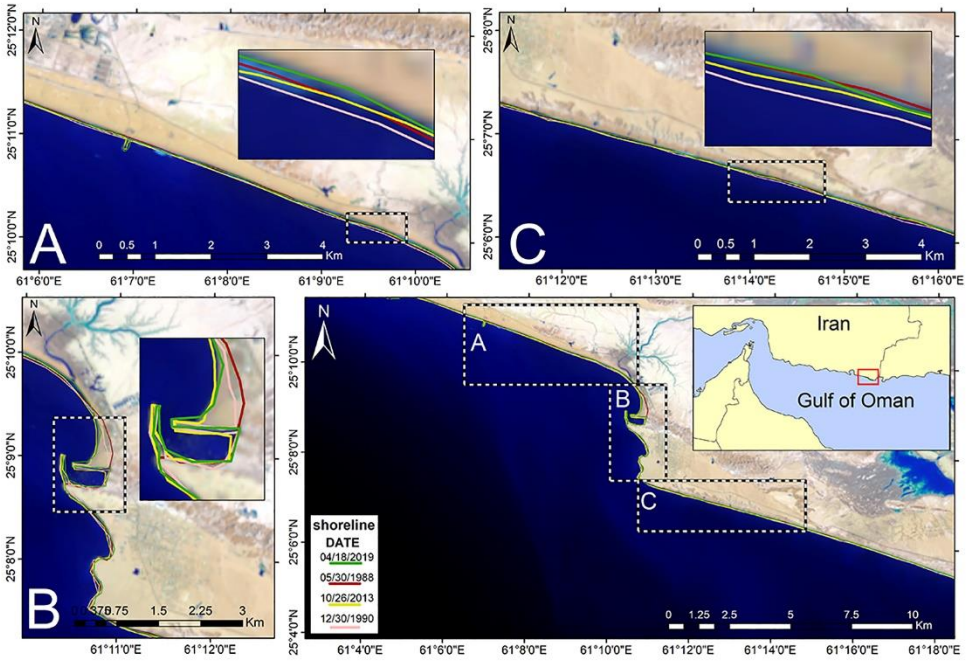

Figure 1: Map of study area in the east of Chabahar- Iran

The area includes approximately 50 km of coastline. This region is adjacent to the Gulf of Oman and is influenced by the Indian Ocean. Tidal condition is mesotidal type and semidiurnal with a range of approximately 1.66 m (Figure 2A). The wind rose of this region indicates domination of wind from the northeast. The average wind speed is about 3.8 m/s and the highest recorded speed is 6.1 m/s (Figure 2B).

According to studies carried out in the Beris Port, the main reason for sediment transport in the area is regional currents. According to literature, areas most affected by sedimentation are the head of the main breakwater and the back of the secondary breakwater [10].

Sayehbani and Ghaderi [13] developing a numerical model of MIKE21, studied the pattern of current and wave around this port. Figure 3 shows the pattern of waves and currents around the Beris port conducted by them. It can be seen that in the back of the main breakwater, the wave height and current velocity are relatively low (sign 2 in left and right side image). However, in the eastern part of the port relative strong current is observable (sign 3 in left side image). They also suggested strong sedimentation in the area which might be detectable by comparing satellite images of different years.

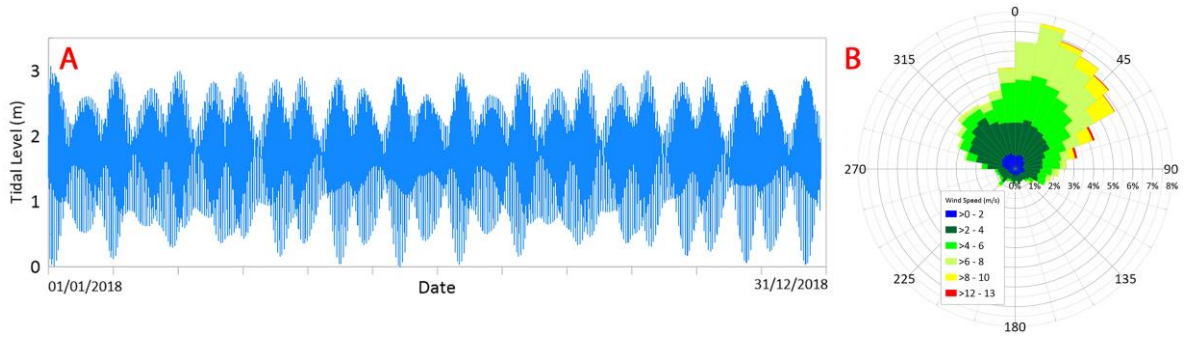

Figure 2: Tidal level (m) in Beris Port from 01/01/2018 – 31/12/2018, taken from National Cartographic Center of Iran (A). Wind rose of the east of Chabahar from 01/01/2018 – 31/12/2018, taken from ECMWF [14] (B)

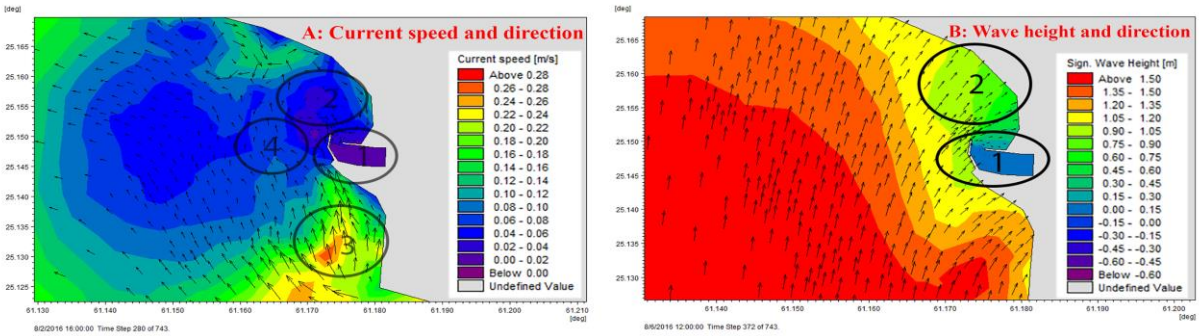

Figure 3: Patterns of wave and current around the Beris port. A) Current speed and direction, B) wave height and direction [13]

2.1 Shoreline detection

2.1.1 Data sources

To monitor shoreline change, georeferenced satellite images from Landsat OLI/TIRS and TM of the years 1988, 1990, 2014 and 2019 were used (Table 1). The logic behind the selection of these years are discussed as follow. Cloud cover causes the loss of important signs in the satellite images. Thus, the main concern for choosing the years was the clarity of the images from clouds. Year 2019 was chosen as the latest coastline records. The closest year (with good clarity images) with at least 5 year interval of the latest change was the year 2014. The first cloud-free image recorded after the construction of the Baris Port was belonged to the year 1990, and the last cloud-free recorded image before the construction of the Port was the year 1988. Landsat satellite imagery with a resolution of 30 meters is the most important tool for investigating shoreline changes [15].

Table 1: Details of data used in this study

Satellite data	Path/Row	Year of acquisition	Resolution (pixel size) (m)	Zone
Landsat 8 OLI/TIRS	156/43	18/04/2019	30	A, B, C
Landsat 8 OLI/TIRS	156/43	22/05/2014	30	A, B, C
Landsat 5 TM	156/43	20/05/1990	30	A, B, C
Landsat 5 TM	156/43	30/05/1988	30	A, B, C

OLI, operational land imager; TIRS, thermal infrared sensor; TM, thematic mapper

2.1.2 Image processing

Image processing involves several steps including geometric, radiometric and atmospheric correction. Using available satellite and aerial imagery, and selection control points in the area, geometric correction is prepared by software ENVI 5.3. Prominent geomorphologic features and river channels where selected as control points. The coordinate system of images has been transformed into Universal Transverse Mercator (UTM). Radiometric and atmospheric correction includes subtraction of the atmospheric contribution, reduction of illumination, viewing angles and terrain effects, and sensor calibration [16,17,18]. These steps are performed using tools in ENVI 5.3 software [7,17,19].

2.1.3 Shoreline Extraction

A sophisticated way to distinguish the border between sea and land is the usage of satellite images with different frequency bonds. In general, water can absorb most near-infrared and mid-infrared radiation. Thus, its reflection is almost zero at these frequencies, while, everything except water are rather reflective. According to this concept, infrared band images can be used as criterion to distinguish the shoreline.

A common method for Landsats image processing, which is also employed by Niya et.al (2013) is the usage of the band ratio [20]. In this method binary-image-1 is generated using the ratio of Band2/Band4 and Band2/Band5. Afterwards, binary-image-2 is developed using the histogram threshold based on band 5. Image-3 is generated by multiplying the two binary images of 1 and 2, in which the deviation between the sea and the land is clearly distinguishable [19,20]. It should be noted that in Landsat 8 the number of bands are different from previous Landsats. That is; bands 2, 4 and 5 are respectively 3, 5, and 6 [21,17]. The final

step involves converting raster images to vector. Afterwards, those modified images are imported to the ArcGIS software to extract the shoreline.

2.2 Shoreline changes assessment

By determining the shoreline variation along transects, changes in the coast and rate of change are measured. For this purpose, a baseline can be created along the shoreline at desired distance, then several transects perpendicular to the baseline would be created with arbitrary distances from one another [22,23]. There are several statistical methods for calculating rate of shoreline change, of which the most common are end-point rate (EPR) and linear-regression rates (LRR) [24]. EPR is simply the rate determined calculating the distance between the oldest and most recent shorelines. LRR is the result of estimating the average rate of changes of shoreline positions over the time [22,12].

In this study, to identify changes in the shoreline by statistical methods, DSAS tool developed by USGS for ArcGIS software is used. There are five steps to use a DSAS tool including: shorelines preparation, baseline creation, transects generation, computation of distances between baseline and shorelines at each transect, and computation of rate of shoreline change (Figure 4) [12]. In this study, in addition to EPR and LRR, SCE and NSM are calculated. The net shoreline movement (NSM) is the distance between the oldest and the youngest shorelines for each transect. The shoreline change envelope (SCE) value represents the greatest distance detected between all the shorelines among all intersects regardless time [12], which means SCE reports a distance in meters. The EPR index is the outcome of dividing the distance of shoreline movement (NSM) by the time elapsed between the oldest and the most recent shoreline [12]. A linear regression rate-of-change statistic can be determined by fitting a least-squares regression line to all shoreline points for a transect. The regression line is placed so that the sum of the squared residuals (determined by squaring the offset distance of each data point from the regression line and adding the squared residuals together) is minimized. The linear regression rate is the slope of the line [12]. Figure 4 shows how these indexes can be calculated. The LRR index has following features: (1) the data can be used irrespective of trend or accuracy, (2) the method is purely computational, (3) the calculation is based on accepted statistical concepts, and (4) the method is easy to employ [25,24].

In this study, the length of shoreline is 48.2 km (according to the measurements of the year 2019), 485 transects are selected with 50 m intervals. This interval value is selected considering the resolution of the images. The coastline is then subdivided into three zones A, B and C (Figure 1), with 184, 132 and 169 transects, respectively. The first transect is located at the western side of zone A, and the last is at the eastern side of zone C. It should be mentioned that 4 transects of zone A, and 18 transects of zone B has been eliminated due to the coastal constructions (Figure 5). It is also necessary to mention that zone B is almost perpendicular to Zones A and C (see Figure 1).

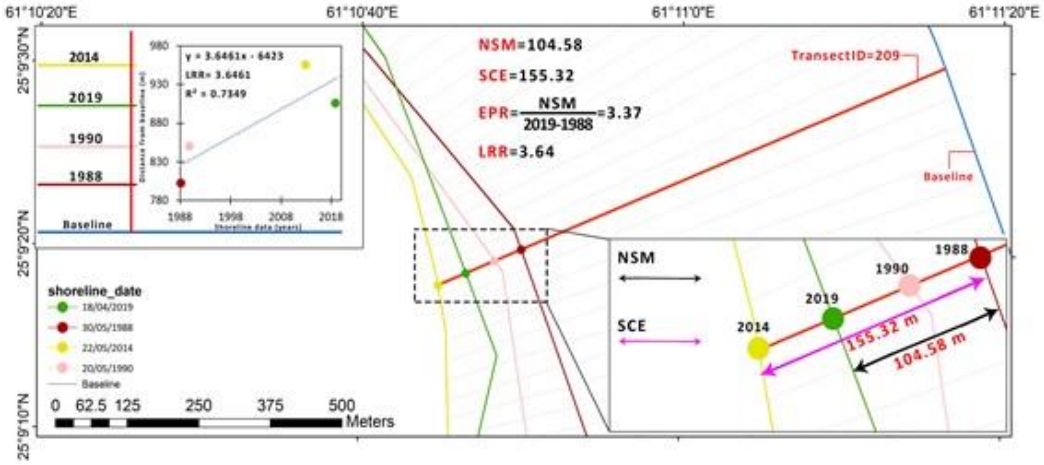

Figure 4: Schematic of the calculation of indexes; NSM, SCE, EPR and LRR in transects 209

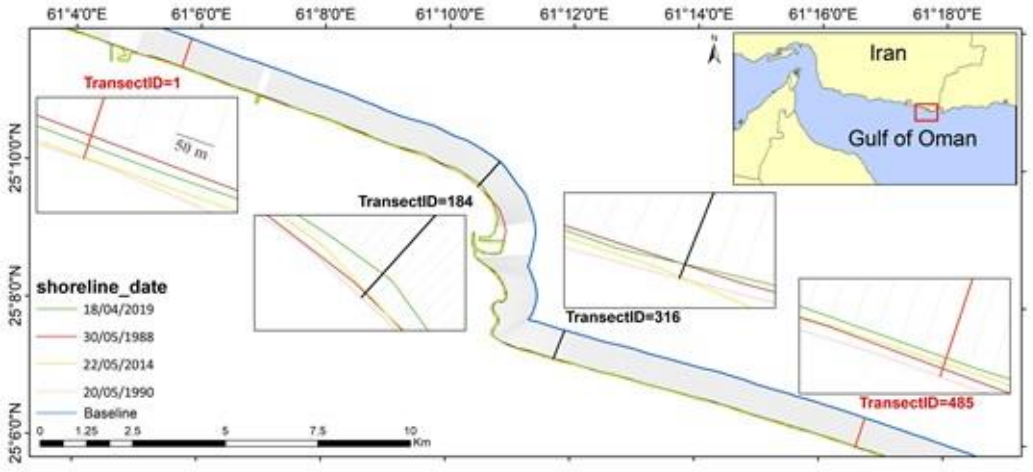

Figure 5: Location of transects, baseline and shoreline for 2019, 2014, 1990 and 1988

3. Results and Discussion

After selecting transects, values of SCE, NSM, EPR, and LRR index are calculated using DSAS tool. Analyzing these indexes, the amount of erosion or accretion in each transect is calculated. Figure 6 shows the shoreline changes from 1988 to 2019 with respect to the two SCE and NSM indexes. The SCE index shows the most changes made regardless data history. Therefore, the SCE index does not show the difference of erosion or accretion, and is always a positive number. As shown in Figure 6, most of the shoreline change occurred west of the Beris Port; areas of significant variation are marked with a dashed square. Due to the characteristic of the SCE index, values close to zero shows minor changes of the shoreline during the period of investigation. During this period the smallest change along the shoreline occurred close to the Beris Port (about 250 m east). The NSM index can indicate the amount of erosion/accretion by evaluating the distance between the oldest and the youngest shorelines. Figure 6 shows that most of the accretion occurred approximately 241 m west of the Beris Port, and the highest erosion occurred at a transect ID 204 (about 89.79 m). By comparing the SCE and NSM index, the type of changes (erosion or accretion) between 1988 and 2019 can be determined.

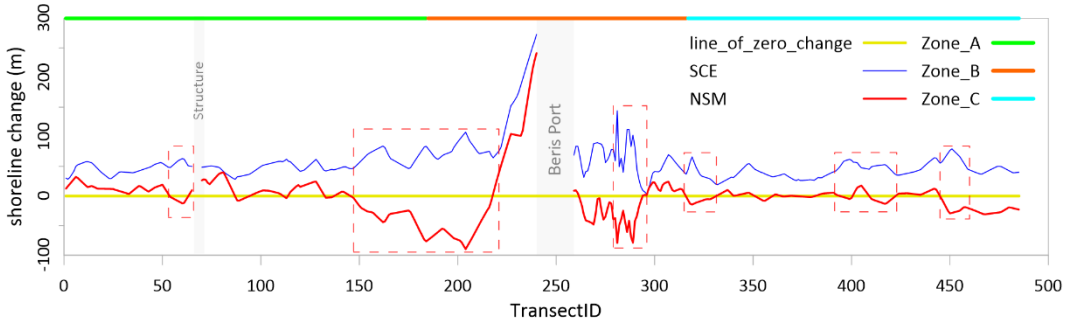

Figure 6: Shoreline change by SCE and NSM index in zone A, B and C during the period 1988 and 2019

The EPR and LRR index can be used to obtain the rate of shoreline changes between 1988 and 2019. Figure 7 shows the annual variation of these two indexes along the shoreline. Generally speaking, the highest and lowest rate of change is observed on the west and east side of the port respectively. There is also aforementioned point of about 250 meters west of the port with the low late of change.

Figure 8 shows the comparison between the two statistical methods of EPR and LRR. Good correlation between EPR and LRR can be observed for zones A and B (Figure 8(a) and 8(b)) with the $R^2 = 0.95$ and 0.96 respectively. In zone C however, weak correlation between the two statistical methods is detected with R2 of 0.61 (Figure 8(c)). One reason for the weak correlation between the two indexes in zone C could be the negligible change between the oldest (1988) and newest (2019) shoreline. It should be noted that it might be considerable variation in shoreline between 1988 and 2019, which is neglected by considering ERP, while LRR index considers the variation between these two years. This can explain the weak result of R2 for Zone C.

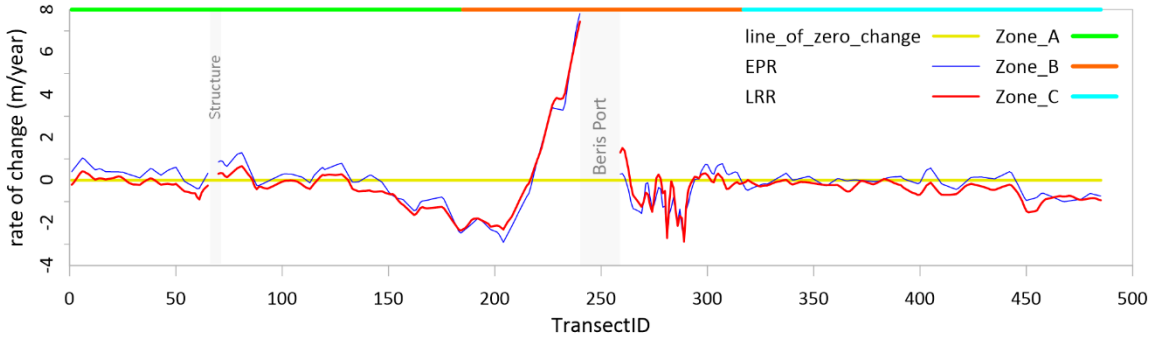

Figure 7: Rate of shoreline change by EPR and LRR index in zone A, B and C during the period from 1988 to 2019

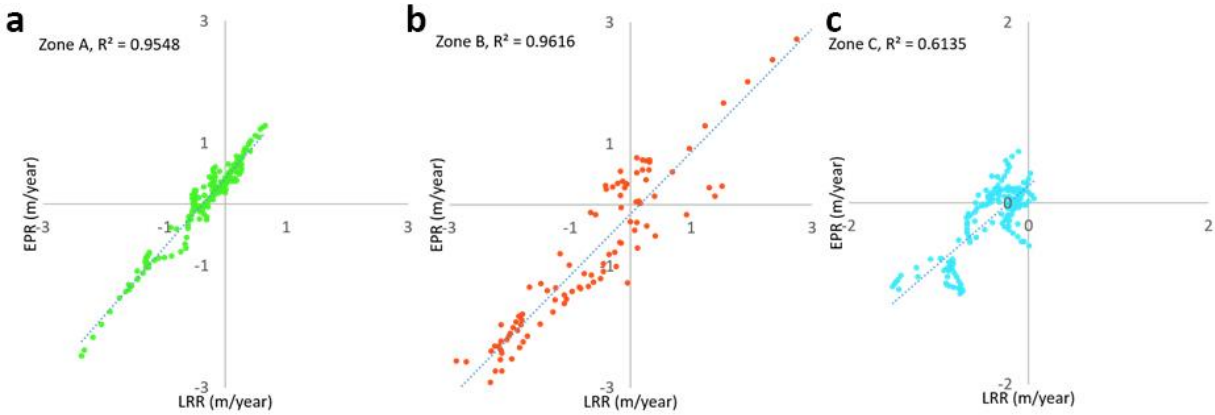

Figure 8: Comparison of shoreline rates (m/year) obtained by different statistical methods (EPR and LRR) in zone A, B and C

Evaluating the results, it was found that LRR index is the most suitable index for describing the erosion and accretion process in all three zones. Table 2 shows the rate of change along the shoreline statistically (m/year) for three zones A, B and C for the duration 1988 to 2019. Figure 9 to 11 show all transects of zone A, B, and C respectively. They are colored according to the LRR value; red means erosion and green means accretion. In the areas near the Beris Port, the maximum erosion rate is 20.36 m and the maximum accretion rate is 0.66 m. Erosion is dominant process in the zone A. On the east side of the structure however, accretion is dominated (Figure 9). Zone B has the highest accretion (7.44 m/year); this is especially evident in the vicinity of western Beris Port (Figure 10). The dominant process in coastline zone C is erosion (Figure 11), but the erosion rate is slower than the other two zones (0.43 m/year in average).

Table 2: Shoreline changes rate (m/year) in three zones A, B and C from 1988 to 2019

Zone	Minimum	Maxim	Average	Standard deviation
A	-2.36	0.66	-0.33	0.60
B	-2.88	7.44	0.058	2.04
C	-1.51	0.06	-0.43	0.35

Figure 9 to 11 are also contain averaged wind speed over the sea, which is presented as a colored area, and a direction. It can be seen that the averaged-speed is about 3.1 to 3.7 m/s in all of the zones, which is in coincidence with results of Figure 2. However, its direction in all three zons is northwest, which is not the same with results presented in Figure 2. This direction of wind can be a factor responsible for circulation observed in Figure 3 in vicinity of Beris Port. This is the area with the highest sedimentation (Figure 10). This means that constructing Beris Port is the main reason for sedimentation in the area. In the zone C (Figure 11) the direction of the current is parallel to the coastline with 3.2 m/s speed. It is therefore, expected uniform erosion or sedimentation along the coast, which can be observed in Figure 11.

It should also be noted that the configuration of coastline zones A and C are almost east-west, while coastline of zone B is almost north-west. This different configuration causes different response of zone B to the dynamic processes such as wind and current. Since this area is perpendicular to the two other Zones, the current could be trapped there and causes circulation as suggested by Sayehbani and Ghaderi (2019). Besides, constructing Beris Port in this zone can be count as another destructive factor for increment in sedimentation and/or erosion there.

According to the ECMWF wind data, the mean annual wind speed in the zone A and B is 3.7 m/s and its predominant direction is southeast (Figure 9,10). The current status of zone A is in the east-west direction. However, near the port of Beris (east of zone A), there is a cycle opposite to the current direction (most erosion occurred in this area). In zone B, due to the Beris port construction, the direction of current is opposite to the main direction in the area (Figure 3A), so this current causes accretion near the port. Zone C has the same wind direction as other zones, but its speed is slightly lower; approximately 3.2 m/s (Figure 11). The

direction of current in this area is also parallel to the coastline.

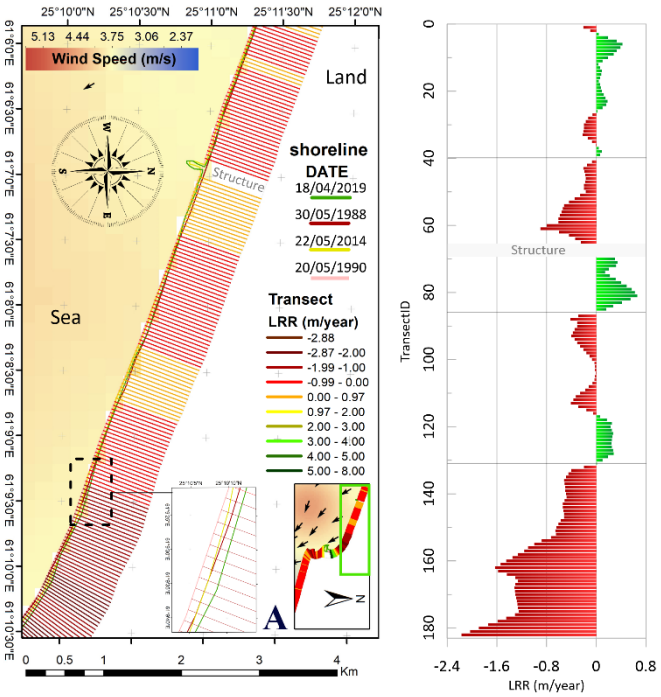

Figure 9: Shoreline evolution between 1988 and 2019 by LRR in zone A. Note: In this figure the dominant wind direction and direction are also shown in the area

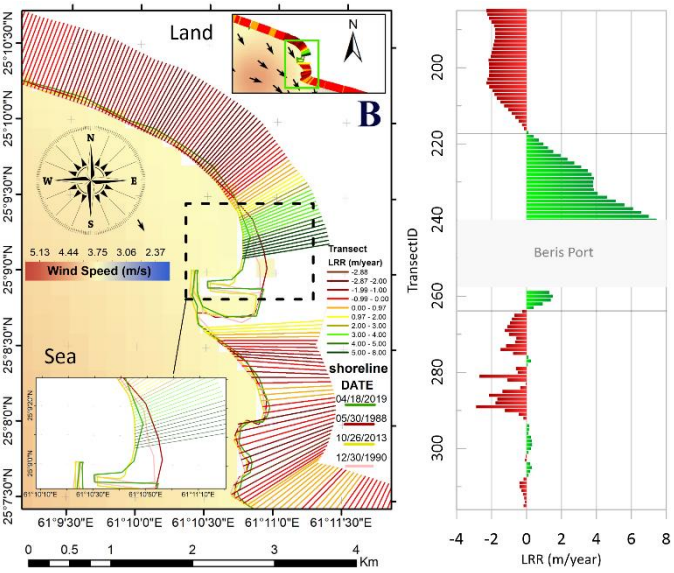

Figure 10: Shoreline evolution between 1988 and 2019 by LRR in zone B. Note: In this figure the dominant wind direction and direction are also shown in the area

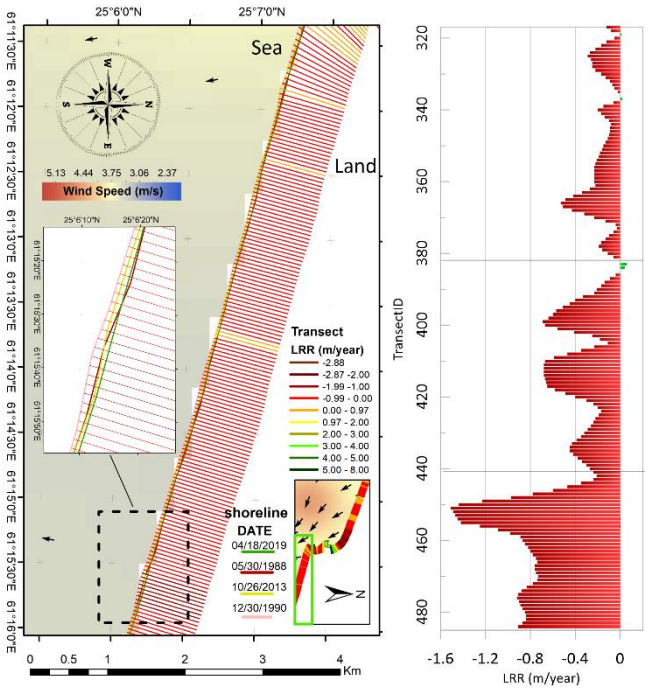

Figure 11: Shoreline evolution between 1988 and 2019 by LRR in zone C. Note: In this figure the dominant wind direction and direction are also shown in the area

4. Conclusion

Images derived from Landsat 8 and 5 of the years 1988, 1990, 2014 and 2019 has been used to assess the rate of erosion/sedimentation along the coastline of Beris east of Chabahar, in Iran. The highest shoreline change (erosion-accretion) was recorded as 7.44 m/year adjacent to the west of the port of Beris and -2.88 m/year at the east of the port (approximately 1500 m from the port of Brice). It was specifically found that the area close to the port of Brice suffers from erosion-accretion rate at most. The direction of the wind, the shape of the coastline, and the pattern of current in the area can be count as the factors responsible for shoreline change. The direction of wind is almost the same in the whole area, while due to the location of Beris port, which its coastline is perpendicular to the adjacent zones, this port is affected by erosion/accretion at most. This can increase the effect of wind and current on this coastline. Also due to the construction of the port, the local current is affected, which can also be accounted as a factor for increasing the rate of change in shoreline. In the western part of the port; after shoreline erosion, the sedimentation took place at the vicinity of the secondary breakwater of the port. Also, in the eastern part erosion occurs due to the shape of the coastline and high current velocity.

5. References

1- Parthasarathy K, Deka PC (2019) *Remote sensing and GIS application in assessment of coastal vulnerability and shoreline changes*: a review. ISH J. Hydraul. Eng., 1-13.

2- Van TT, Binh T. T (2008) *Shoreline change detection to serve sustainable management of coastal zone in Cuu Long Estuary*. Paper presented at the

International Symposium on Geoinformatics for Spatial Infrastructure Development in Earth and Allied Sciences.

3- Bird ECF, Ongkosongo OS (1980) *Environmental changes on the coasts of Indonesia*: UNU.

4- Oost A, Hoekstra P, Wiersma A, Flemming B, Lammerts E, Pejrup M, Bartholdy J (2012), *Barrier island management: Lessons from the past and directions for the future*. Ocean Coast Manage, 68, 18-38.

5- Van Cuong C, Russell M, Brown S, & Dart P (2015) *Using Shoreline Video Assessment for coastal planning and restoration in the context of climate change in Kien Giang, Vietnam*. Ocean Sci J, 50(2), 413-432.

6- Marfai MA, Almohammad H, Dey S, Susanto B, King L (2008) *Coastal dynamic and shoreline mapping: multi-sources spatial data analysis in Semarang Indonesia*. Environ Monit Assess, 142(1-3), 297-308.

7- Do AT, de Vries S, Stive MJ (2018) *The Estimation and Evaluation of Shoreline Locations, Shoreline-Change Rates, and Coastal Volume Changes Derived from Landsat Images*. J Coastal Res.

8- Maiti S, Bhattacharya AK (2009) *Shoreline change analysis and its application to prediction: A remote sensing and statistics based approach*. Mar Geol, 257(1-4), 11-23.

9- Nassar K, Mahmod W E, Fath H, Masria A, Nadaoka K, Negm A (2019) *Shoreline change detection using DSAS technique: Case of North Sinai coast, Egypt*. Mar Georesour Geotechnol, 37(1), 81-95.

10-Ardani S, Soltanpour M (2015) *Modelling of sediment transport in Beris fishery port*. CEIJ, 48(1), 69-82.

11- Hajivalie F, Soltanpour M (2007) *Beris fishing port, interfering in the equilibrium shape of a bay*. In Coastal Engineering 2006: (In 5 Volumes) (pp. 3843-3850): World Scientific.

12- Thieler ER, Himmelstoss EA, Zichichi JL, Ergul A (2009) *The Digital Shoreline Analysis System (DSAS) version 4.0-an ArcGIS extension for calculating shoreline change (2331-1258).* Retrieved from

13- Sayehbani M, Ghaderi D (2019) *Numerical Modeling of Wave and Current Patterns of Beris Port in East of Chabahar-Iran*. IJCOE, 3, 21-29.

14- Berrisford P, Dee D, Poli P, et al (2011) *The ERA-Interim archive, version 2.0*.

15- Blodget H, Taylor P, Roark J (1991) *Shoreline changes along the Rosetta-Nile Promontory: Monitoring with satellite observations*. Mar Geol, 99(1-2), 67-77.

16- Lillesand T, Kiefer RW, Chipman J (2015) *Remote sensing and image interpretation*; John Wiley & Sons.

17- Louati M, Saïdi H, Zargouni F (2015) *Shoreline change assessment using remote sensing and GIS techniques: a case study of the Medjerda delta coast*, Tunisia. Arabian J Geosci, 8(6), 4239-4255.

18- Mather PM, Koch M (2011) *Computer processing of remotely-sensed images: an introduction*; John Wiley & Sons.

19- Masria A, Nadaoka K, Negm A, Iskander M (2015) *Detection of shoreline and land cover changes around Rosetta promontory, Egypt, based on remote sensing analysis*. Land, 4(1), 216-230.

20- Niya AK, Alesheikh AA, Soltanpor M, Kheirkhahzarkesh MM (2013) *Shoreline change mapping using remote sensing and GIS*. IJRSA, 3(3), 102-107.

21- Kuleli T (2010) *Quantitative analysis of shoreline changes at the Mediterranean Coast in Turkey*. Environ Monit Assess, 167(1-4), 387-397.

22- Chand P, Acharya P (2010) *Shoreline change and sea level rise along coast of Bhitarkanika wildlife sanctuary, Orissa: an analytical approach of remote sensing and statistical techniques*. IJGGS, 1(3), 436.

23- Emran A, Rob MA, Kabir MH, Islam MN (2016) *Modeling spatio-temporal shoreline and areal dynamics of coastal island using geospatial technique*. MESE, 2(1), 4.

24- Dolan R, Fenster MS, Holme SJ (1991) *Temporal analysis of shoreline recession and accretion*. J Coastal Res, 723-744.

25- Crowell M, Douglas BC, Leatherman SP (1997) *On forecasting future US shoreline positions: a test of algorithms*. J Coastal Res, 1245-1255.

INTERNATIONAL JOURNAL OF
COASTAL & OFFSHORE ENGINEERING
IJCOE Vol.5/No. 4/Winter 2020 (9-17)

Available online at: www. Ijcoe.org

Probabilistic Seismic Direct Loss Estimation for Ports, Case study: Pars Asaluyeh port

Seyed Farshid Montazeri [1], Rouhollah Amirabadi [2]

[1] *M.S. Student, Department of Civil Engineering, University of Qom, Farshid91@gmail.com*
[2] *Assistant Professor, Department of Civil Engineering, University of Qom, r.amirabadi@qom.ac.ir*

ARTICLE INFO

Article History:
Received: 29 Apr. 2020
Accepted: 11 Jul. 2020

Keywords:
PEER-PBEE,
Seismic Risk Density
Economic Loss
Probabilistic Direct Loss estimation
Port of Pars Asaluyeh

ABSTRACT

Ports are the main avenue of global freight transport. In the past, experience has shown that ports are vulnerable to earthquakes, which cause evident economic damage. The port at Kobe, Japan, experienced economic losses of about $11 billion after an earthquake in 1995. The present study used the full-probabilistic PEER-PBEE framework to develop a comprehensive seismic risk assessment approach with which to estimate the total direct and indirect economic loss incurred by a port experiencing an earthquake. In the proposed methodology, the extent of direct economic loss due to the cost of repair of port structures in the Pars Asaluyeh port was estimated. Seismic risk density curves (SRDCs) were employed to determine the seismic performance of different port structures and pieces of equipment as well as the overall seismic performance of the port. The SRDCs show that the mooring structures and breakwater of the port showed appropriate seismic performance, while other port structures and equipment showed weak or average seismic performance.

1. Introduction

Earthquakes can cause major economic losses to the infrastructure of a country as well as loss of lives, social-psychological consequences, and environmental damage. The Great Hanshin earthquake in Kobe in 1995 is a good example. It caused $100 billion in direct economic losses, caused 6500 deaths, and injured 43,000 people [1]. Studies on the response of infrastructures, installations and lifelines after this earthquake can improve understanding of the extent of vulnerability of these structures.

The consequences of the Kobe earthquake revealed that ports are vulnerable lifelines. Among the lifelines of Kobe, which included utilities, telecommunications, water, natural gas, railways, highways, and the port, the results indicated that the port required the longest recovery time [2]. The effects from the earthquake included an increase in freight transport costs, reduction in income of a noticeable portion of the community, as well as noticeable a drop in rank of the Port of Kobe as the premier container port globally. Direct economic loss to the port caused by damage was $5.5 billion and economic loss caused by downtime was $6 billion during the year following the earthquake [3].

Studies on the Northridge [1994], Chi-Chi [1999], and Haiti [2010] earthquakes reveal similar results in relation to the high vulnerability of ports. Ports play a major role in national, regional, and global economies. About 90% of total cargo transit is delivered through ports [4]. The importance of ports and their vulnerability to earthquakes make seismic risk assessment and management of interest to researchers.

Pachakis and Kiremdijian [5,6] proposed a methodology for estimating physical damage due to earthquakes and loss due to downtime of a port system. In their model, a port was considered to be a complex of wharves and mooring structures, cargo handling equipment, accessways, warehouses, and infrastructures. Ichii [7] used a seismic risk density curve (SRDC) to evaluate the seismic status of port structures and categorized the structures based on function as having either strong, medium, or weak seismic performance levels.

Warner et al. [8-10] assessed the seismic risk of the port of Auckland and created a framework for seismic risk assessment of the entire port system. They also conducted a project for a seismic risk reduction program for the port of Portland. This included an assessment of acceptable risk which can be used as a guide for determining improvements required in

response to seismic activity to increase the seismic performance level of the entire port system.

Na and Shinozuka [11] proposed a methodology for estimating the effect of an earthquake on the performance of a port using fragility curves. They estimated direct losses due to an earthquake and economic loss due to downtime of the port system.

Amirabadi et al. [12] proposed a methodology to assess comprehensive seismic risk in ports that addresses five categories: estimation of life safety risks such as death and injury; direct and indirect economic losses; environmental risks; social, political, and ethical risks; and spiritual and psychological risks.

Burden et al. [13] developed the risk assessment framework proposed by PEER for assessing the seismic risk of ports. In order to consider port service interruption or port downtime, a term was added to the general relation for PEER-PBEE called "repair requirement".

Lam and Lassa [14] investigated the different risks threatening ports and proposed a method for evaluating them. Port facilities and structures were classified as either buildings, utility systems, or transportation infrastructure. The risks threatening marine transportation, particularly ports, included earthquake, tsunami, climate extremes, environmental risks, economic risks, policy risks, security risks, regular supply risks, and daily operational risks.

Iran is a country with a high risk of earthquake occurrence. The seismic risk status of important ports in Iran are shown in Figure 1. It can be seen that almost all main ports are located in regions with high seismic risk potential and it is imperative for these ports to consider seismic risk assessment.

In order to estimate the effect of earthquakes on ports, a methodology called comprehensive seismic risk assessment (CSRA) of ports has been proposed using the full-probabilistic PEER-PBEE framework. The proposed methodology provides the opportunity to accurately investigate the effects of an earthquake on ports, including the probability of failure of port structures and equipment, of secondary risks from the earthquake, of downtime of the port after the earthquake, the time required for recovery of the port, and direct and indirect economic and environmental losses incurred by the port.

The proposed methodology was used to estimate the direct economic loss due to an earthquake at Pars Asaluyeh port. A seismic risk density curve (SRDC) then was developed for each part of the port. These curves were used to assess the seismic performance of different parts of the port.

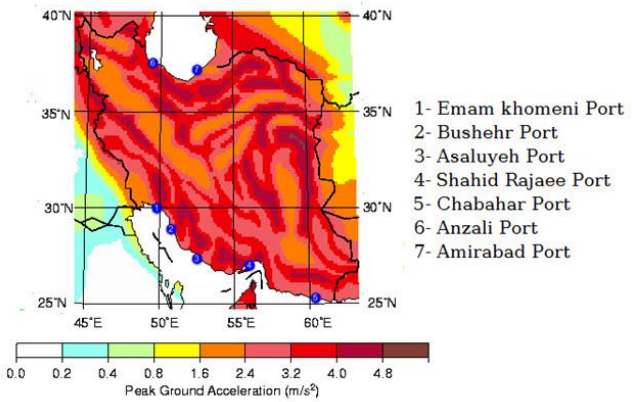

Figure 1. Hazard map showing seven major Iranian ports [15, 16]

The SRDC demonstrates the distribution of the probability density function for seismic risk. It was developed by multiplying the damage incurred by the probability density function of earthquake occurrence. The area below the SRDC represents the expected annual losses. The figure denotes the seismic performance of the structure and equipment. In this case, elliptical risk density curves represent weak seismic performance, hump-shaped risk density curves represent average seismic performance, and sharply-peaked risk density curves represent strong seismic performance [7]. Using the proposed methodology, the cumulative function of economic loss due to an earthquake for each component and the economic loss function for the entire port system was obtained. The SRDC provides an appropriate assessment of seismic performance of each component of the port.

2. Proposed Approach

The effects of earthquakes on ports are classified in the Seismic Guidelines for Ports [17] as being life safety, economic, environmental, political/ethical/aesthetic, and psychological risks. It is not possible to assess any of these risks using the current seismic design standards of port structures. Thus, the risk assessment framework proposed by PEER was developed and combined with the proposed CSRA for ports.

Statistics on recent earthquakes in the USA and Japan indicate that the resulting significant economic losses were beyond expectations. This fundamentally changed the concept of the seismic design of port structures. The most important reason for such changes was the lack of logical descriptions for some of the rules applied by designers and the lack of attention by employers to seismic-resistant retrofitting.

The most important reason for reliance on a performance-based design approach has been to encourage innovation in developing new methods to improve performance. In the seismic design standards for port structures, there exists a concept known as performance-based seismic design. It was developed using a number of performance objectives which

enable prediction of performance levels in order to determine the level of risk.

Although advances in development of performance-based seismic design have been remarkable, deficiencies exist. Development of a total probabilistic performance-based seismic risk assessment framework for port systems using the PEER-PBEE framework is an efficient method of comprehensively assessing the seismic risk of such a system. Using this framework, it is possible to correctly assess seismic risks to a port system. The general relation proposed in PEER-PBEE is as follows:

$$P(\mathrm{DV}) = \iiint P(DV|DM).P(DM|EDP).P(EDP|IM).f(IM)\,dDM\,dEDP\,dIM \quad \text{(R-1)}$$

The PEER risk assessment framework equation operates in four stages: hazard analysis, structural analysis, damage analysis, and loss analysis. In hazard analysis, the seismic hazard at a facility is assessed by producing sample ground-motion time histories with an intensity measure (IM) appropriate to different hazard levels. In the structural analysis phase, the response of the facility to a ground motion of given IM is calculated in terms of drift, acceleration, ground failure, stress, strain, and other engineering demand parameters (EDP). In the damage analysis stage, the EDPs are used with component fragility functions to determine the damage measure (DM) to the facility.

Once the DM has been determined, the repair efforts can be evaluated to determine the serviceability, repair costs, repair duration (total cost), and the potential for casualties. These measures are called decision variables (DV) because they can be used to influence stakeholder decisions about future performance [18]. In this study, the damage states were assumed to be discrete. Relation 1 can be rewritten for discrete damage states as follows:

$$P(\mathrm{DV}) = \sum_{i=1}^{NDS_i} \iint P(DV|DM).P_i(DM|EDP).P(EDP|IM).f(IM)\,dEDP\,dIM \quad \text{(R-2)}$$

Using the total probabilistic PEER-PBEE framework for the CSRA of ports, the total economic loss caused by an earthquake to a port can be calculated as the sum of direct economic loss, indirect economic loss, and environmental economic loss. Direct economic loss caused by an earthquake includes the cost of repair and renovation of different parts of a port. Indirect economic loss is damage caused by interruption of port services. In the proposed approach, loss due to death or socio-psychological consequences caused by an earthquake have been included. These cannot be estimated because they were not considered in the overall economic losses in the PEER-PBEE framework, which includes direct and indirect economic and environmental losses.

2.1. Proposed CSRA framework

Figure 2 shows the proposed CSRA framework. The approach is presented in ten steps that are distinguished by different colors. In step 1 (dark red box), the annual average hazard of earthquake occurrence at a port site is estimated. In step 2 (red box), the probability of direct damage due to an earthquake (primary hazard) is estimated using fragility curves. In step 3 (orange box), the performance reliability of the port as it relates to the primary hazard is estimated. Because a port system is composed of several components, the use of FTA is required in order to estimate reliability.

In step 4 (yellow box), the probability of secondary hazards caused by an earthquake, including fire following an earthquake, inundation, falling objects, release of hazardous materials, and explosions have been estimated. In step 5 (light green box), the consequences and damage due to secondary hazards in the port are estimated. In step 6 (green box), the total damage incurred due to primary and secondary hazards is estimated. In step 7 (light blue box), direct economic loss due to damage to structures and equipment at the port and the period required for recovery to resume operation are estimated. In step 8 (blue box), indirect economic loss due to downtime at the port is calculated. In step 9 (dark blue box), environmental, life safety and socio-psychological risks due to an earthquake are estimated. In step 10 (purple box), the total economic loss due to direct and indirect economic losses and environmental economic losses are calculated.

3. Case Study: Port of Pars Asaluyeh

The port studied in this research is at Pars Asaluyeh, the location of which is indicated in Figure 1. Pars Asaluyeh is a multipurpose port. Wharves 1, 2, 6, 7, 8, and 9 are for containers, wharves 3 and 4 are for exportation of sulfur and bulk materials, wharf 5 provides services to the installations of South Pars Gas Field, and wharf 10 is for exportation of gas condensate and fueling.

Seismic risk assessment in the Pars Asaluyeh port is important from several aspects. This port is located in a region with high seismic risk potential and is responsible for providing service to one of the largest gas fields in the world (South Pars Gas Field). Figure 4 is plan of the port. The structures are classified into the categories of mooring structures, breakwaters, infrastructures, and cargo handling structures. Classification of the structures and equipment has been based on the proposed methodology as shown in Figure5.

3.1. Probability function of earthquake occurrence at site of port

To estimate direct economic loss for Pars Asaluyeh port using the proposed methodology, the mean annual

probability of exceedance was estimated for an earthquake at the site of the port. The probability of earthquake occurrence was considered using the report provided by the Seismic Hazard and Geotechnical Hazard Zonation of Asaluyeh (910 ha) by the IIEES [20]. The curve of the probability of an increase in annual average earthquake risk for Asaluyeh region is provided in Figure 6 in the form of a complementary cumulative distribution function.

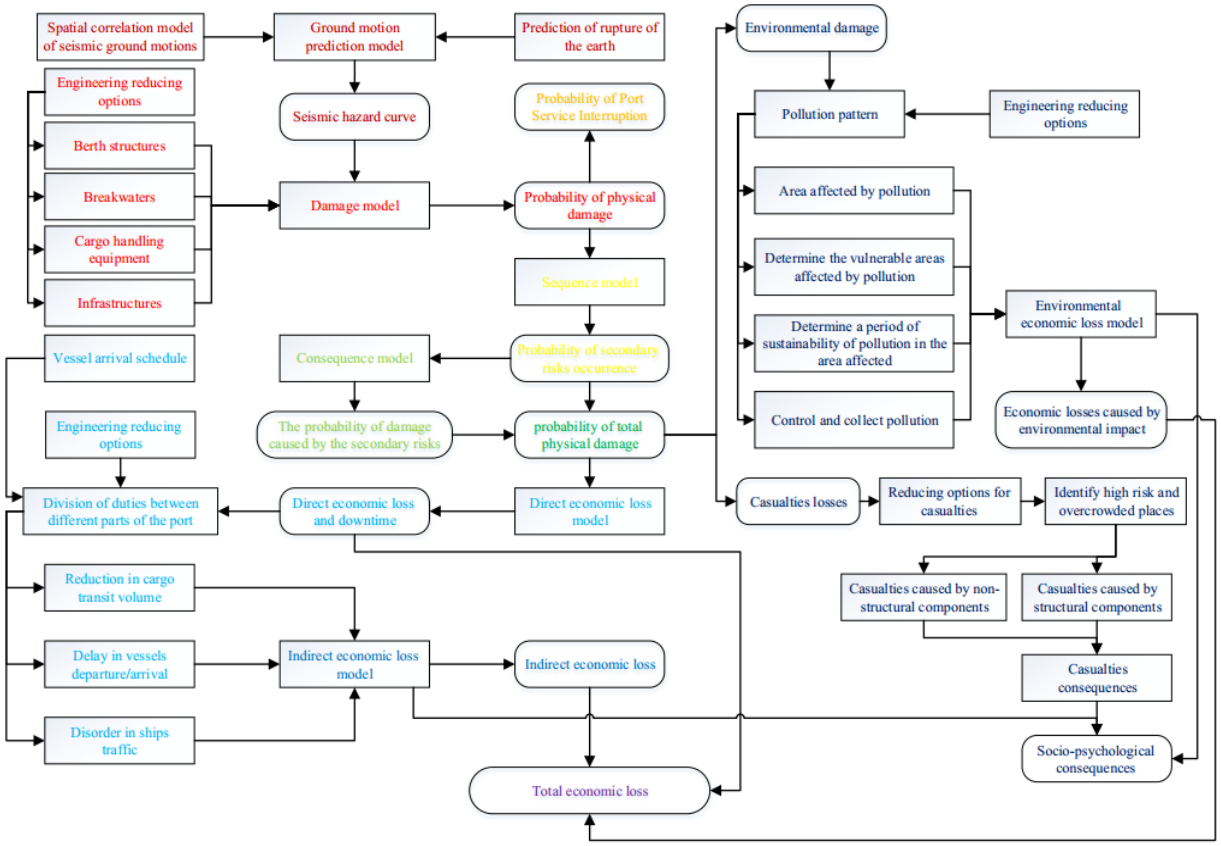

Figure 2. Framework of comprehensive seismic risk assessment of ports

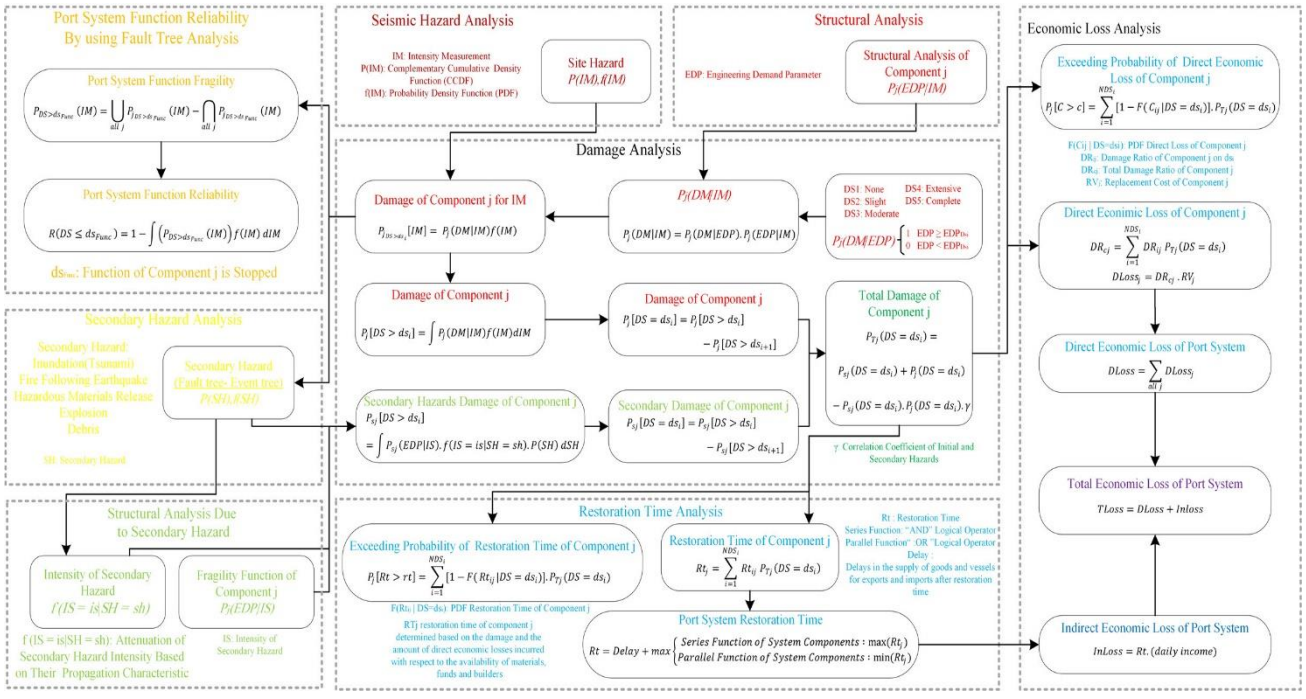

Figure 3. Probabilistic model framework of comprehensive seismic risk assessment of ports

Figure 4. Plan of Pars Asaluyeh port

3.2. Fragility curves for structures at port

After determining the earthquake risk function, the probability of direct damage due to an earthquake for each part and structure in the port should be determined. The development of fragility curves for the port structures were the next step toward estimating direct economic loss. A fragility curve is a logarithmic normal cumulative probability function which represents the probability of an increase in damage from a definite limit in a definite state of earthquake risk. These curves were based on the curves provided in HAZUS for different port structures based on their specifications [21]. The damage states in HAZUS were slight, moderate, extensive, and complete. Table 1 lists the means and standard deviations of the different port structures.

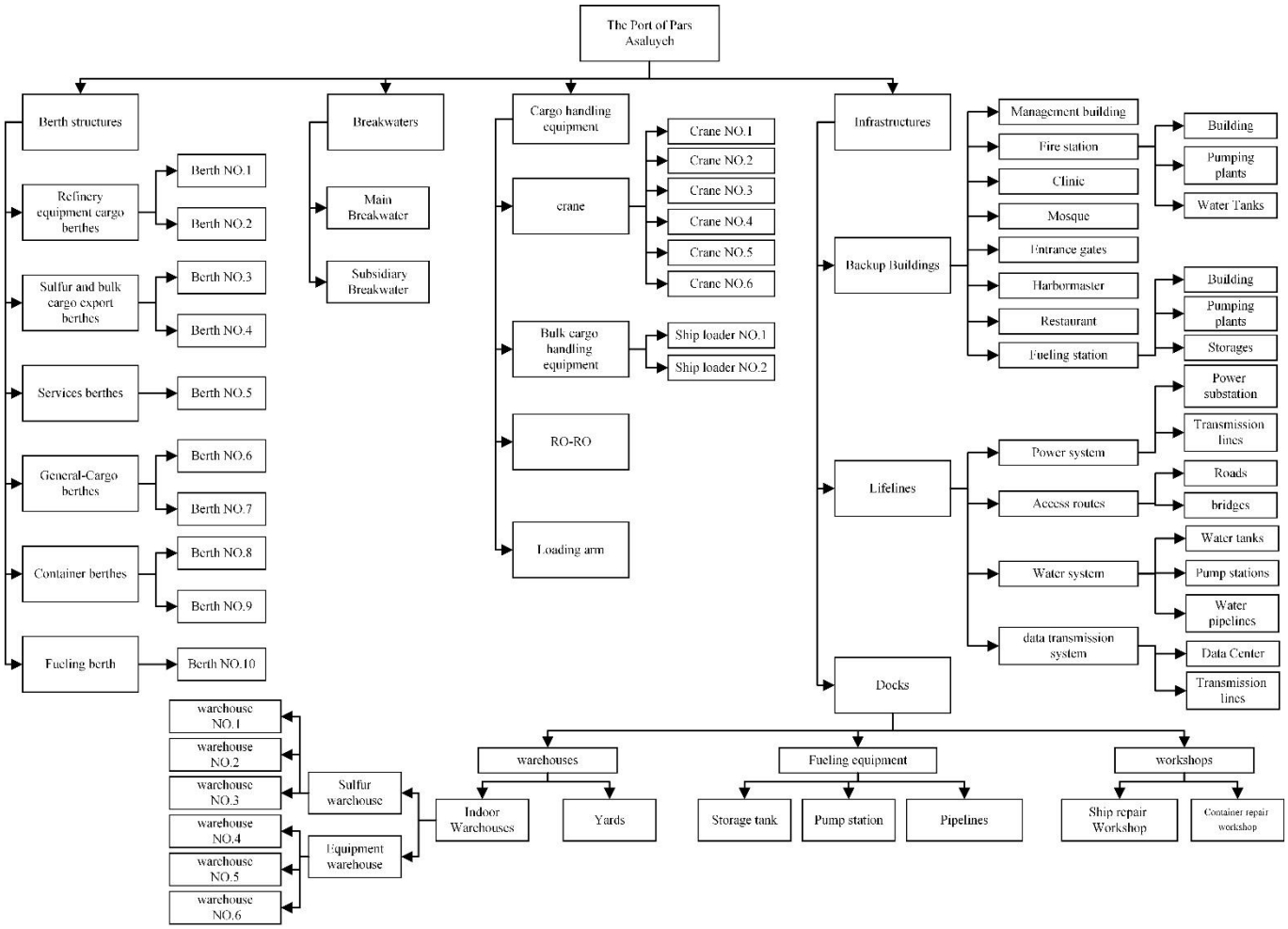

Figure 5. Classification of structures and equipment at port based on CSRA framework

In HAZUS, for structures such as breakwaters and wharves, fragility curves were defined based on permanent ground deformation. For other structures, they were defined based on peak ground acceleration. The method proposed by Saygili [19] was used to unify the differences. The curve of the occurrence of an earthquake in the Asaluyeh region and fragility curves of the port structures were used to estimate the probability of unserviceability of the port. Figures 7 and 8 provide the conditional probability curves for unserviceability of Pars Asaluyeh port based on different applications for the entire port.

3.3. Direct economic loss curves for different port structures

In the next step, in order to estimate the direct economic loss for the port, the damage and repair ratios and recovery costs of the equipment and different structures should be determined. The values proposed in HAZUS were used and provided in Table 2 [21].

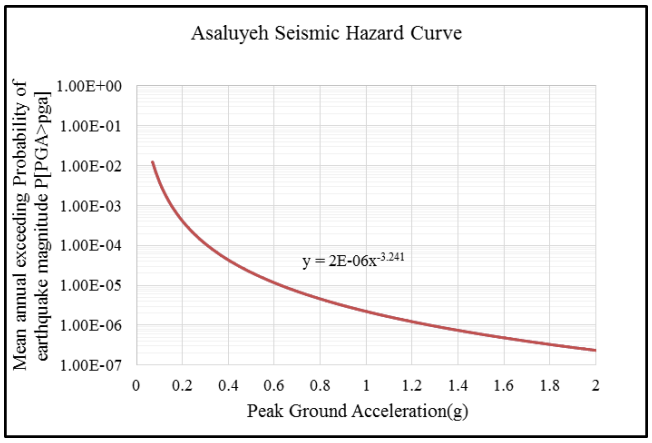

Figure 6. Mean annual probability of exceedance for an earthquake in Asaluyeh region

Table 1. Mean and standard deviations of fragility curves for port structures based on HAZUS

Structure	Slight		Moderate		Extensive		Complete	
	Median	β_i	Median	β_i	Median	β_i	Median	β_i
Wharf type1	20.32 cm	0.6	40.6 cm	0.6	60.9 cm	0.6	152.4 cm	0.6
Wharf type2	12.7 cm	0.6	30.4 cm	0.6	43.18 cm	0.6	109.2 cm	0.6
Breakwater	20.32 cm	0.6	40.6 cm	0.6	60.9 cm	0.6	152.4 cm	0.6
Crane	0.15 g	0.6	0.35 g	0.6	0.8 g	0.7	0.8 g	0.7
RoRo-Trailer	0.3 g	0.6	0.5 g	0.6	1 g	0.7	1 g	0.7
Storage	0.24 g	0.64	0.41 g	0.64	0.76 g	0.64	1.46 g	0.64
Fueling System	0.12 g	0.5	0.27 g	0.5	0.64 g	0.6	1.1 g	0.6
Fuel loading arm	0.15 g	0.6	0.35 g	0.6	0.8 g	0.7	0.8 g	0.7
Substation	0.15 g	0.6	0.25 g	0.5	0.35 g	0.4	0.7 g	0.4
Road	30 cm	0.7	60 cm	0.7	154 cm	0.7	154 cm	0.7
Bridge	10 cm	0.2	10 cm	0.2	10 cm	0.2	35 cm	0.2
Tower Control	0.12 g	0.64	0.23 g	0.64	0.57 g	0.64	1.07 g	0.64

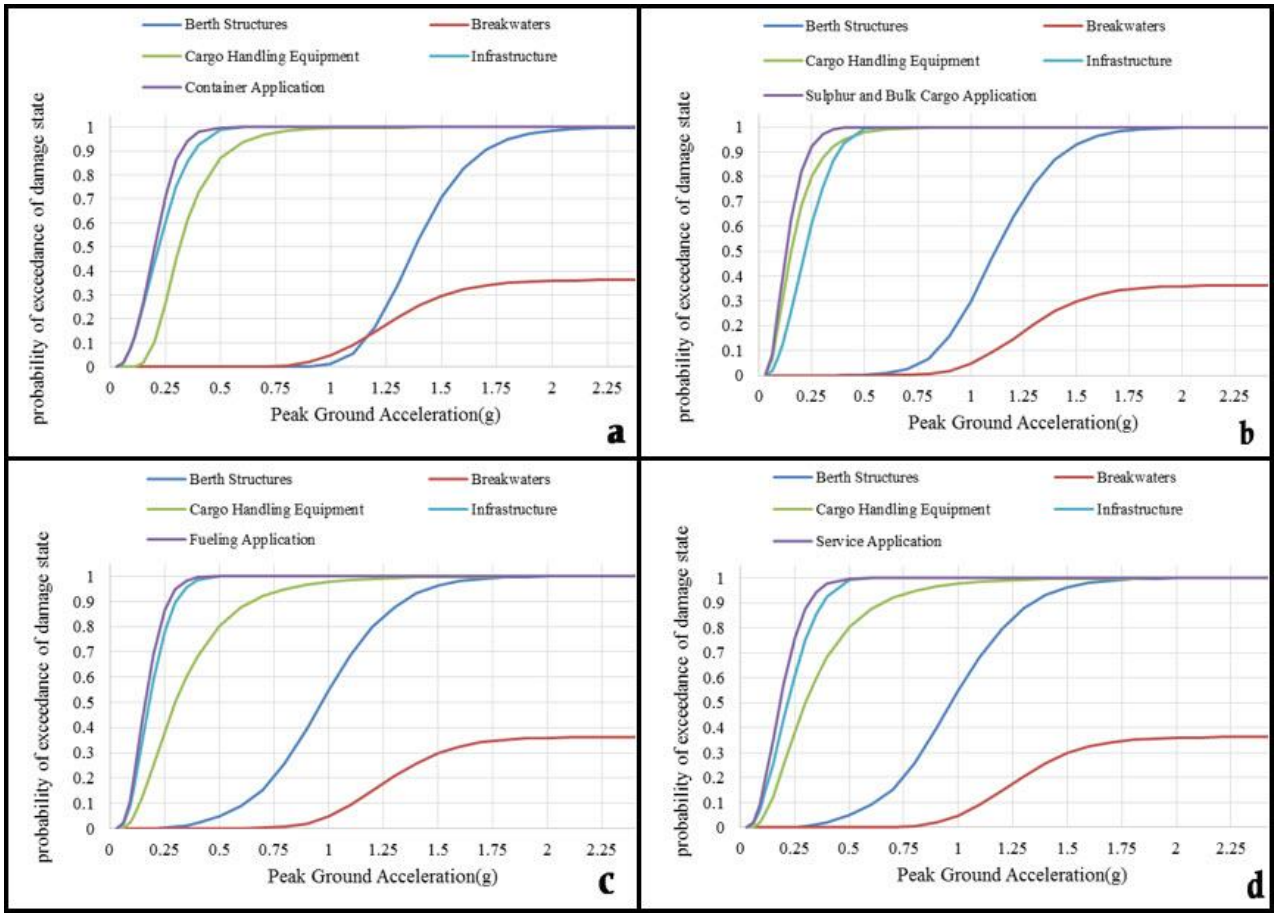

Figure 7. Conditional probability curve for unserviceability of port structures and equipment for Pars Asaluyeh port: (a) containers; (b) sulfur and bulk material exports; (c) fueling; (d) service to South Pars Gas Field.

The data from the fragility functions and damage and cost ratios for repair and recovery of the structures of the port system and direct economic losses for each structure can be estimated for different earthquake intensities or earthquake occurrence probabilities. Figure 9 shows the direct economic loss functions of the port structures and equipment estimated using the proposed methodology. The minimum direct economic loss at low earthquake intensities was for the mooring structures and breakwater of the port. For the high

intensities, the minimum direct economic loss was for infrastructures such as the pumping station, power posts, and warehouses. The differences relate to the higher costs of repair and recovery of the mooring structures and breakwater.

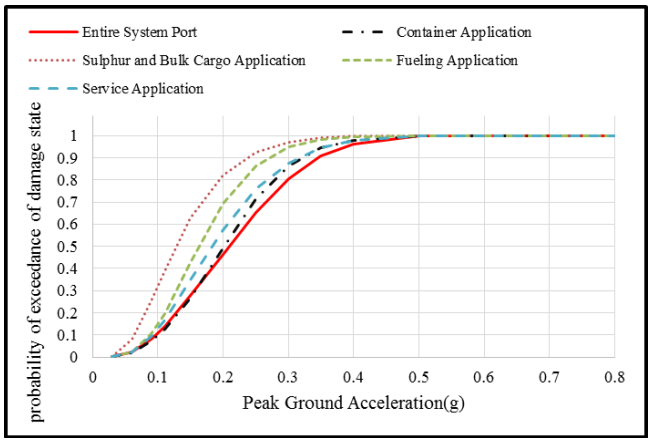

Figure 8. Conditional probability curve for unserviceability of entire system of Pars Asaluyeh port

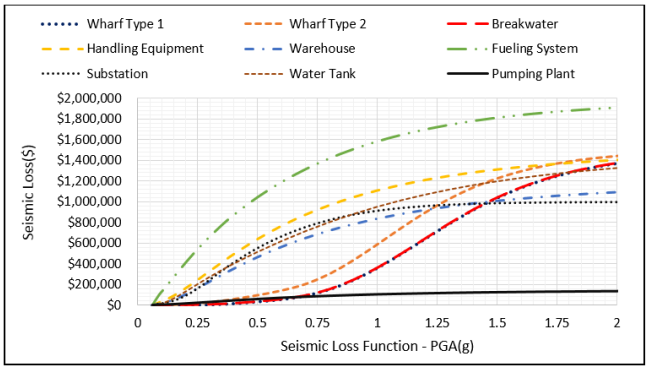

Figure 9. Direct economic loss for port structures vs. earthquake intensity

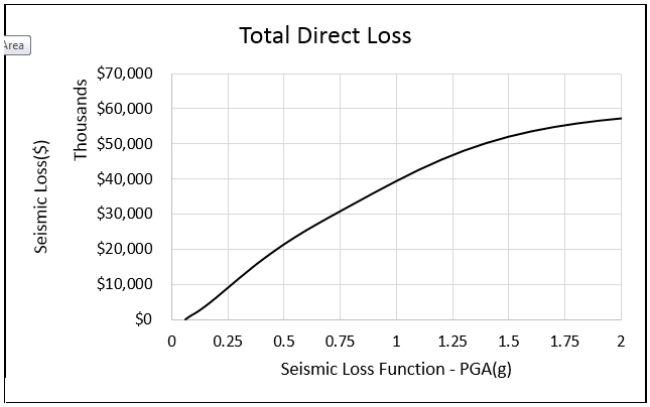

Figure 10. Direct economic loss function for entire port based vs. earthquake intensity

3.4. Direct economic loss curve of entire port system

By combining all direct economic loss functions based on the number and diversity of structures and equipment existing in the port, the total direct economic loss for the port can be calculated as shown in Figure 10. The figure indicates that, for low-intensity earthquakes, the

gradient of economic loss function for the entire port is larger and the gradient decreases with an increase in intensity of the earthquake. The reason for this is that, at lower earthquake intensities, damage increases at a higher rate than at higher earthquake intensities. Seismic retrofitting of port structures to decrease direct economic loss appears to be necessary.

Table 2. Damage, repair and recovery costs of equipment and structures of port based on HAZUS

Structure/equipment	Cost of repair/recovery ($1000)	Damage ratio per damage state			
		Slight	Moderate	Extensive	Complete
Wharf	1500	0.1	0.4	0.8	1
Breakwater	1500	0.1	0.4	0.8	1
Handling QUIP	2000	0.05	0.25	0.75	0.75
Storage	1200	0.1	0.4	0.8	1
Fueling system	2000	0.16	0.39	0.8	1
Substation	10000	0.05	0.11	0.55	1
Water tank	1500	0.2	0.4	0.8	1
Pumping plant	150	0.05	0.38	0.8	1
Control tower	5000	0.1	0.4	0.8	1
Buildings	1.5/m	0.09	0.35	0.73	1

4. SRDC for port structures

Risk density curves were used in order to assess the seismic performance of different port structures. The area below the SRDC represents the annual expected economic losses due to an earthquake. The risk-density curve denotes the annual distribution of risk probability density, which can be calculated using the earthquake risk probability density function for the site and the seismic economic loss function.

The earthquake risk curve can be calculated using the records of past earthquakes and/or active faults near the site. This curve represents the mean annual probability of exceedance of a definite earthquake magnitude. By applying a differential operator to this function, the earthquake risk probability density function can be obtained.

Figure 6 shows the curve for the mean annual exceedance of probability of an earthquake for the region. The loss function indicates the extent of loss incurred due to an earthquake of a specific magnitude. The SRDC function can be obtained by applying a multiplication operator to the probability density function and the economic loss function due to an earthquake.

Figure 6 represents the seismic performance status. The elliptical risk density curves represent weak seismic performance, the hump-shaped risk density curves represent average seismic performance, and the sharply-peaked risk density curve represents strong or high seismic performance. Using the SRDC results for the structures and equipment of the port, their seismic performance status can be assessed. Figure 11 shows

the SRDC for structures and port equipment. According to the shape of the curve, engineering judgment can be made about the level of seismic performance.

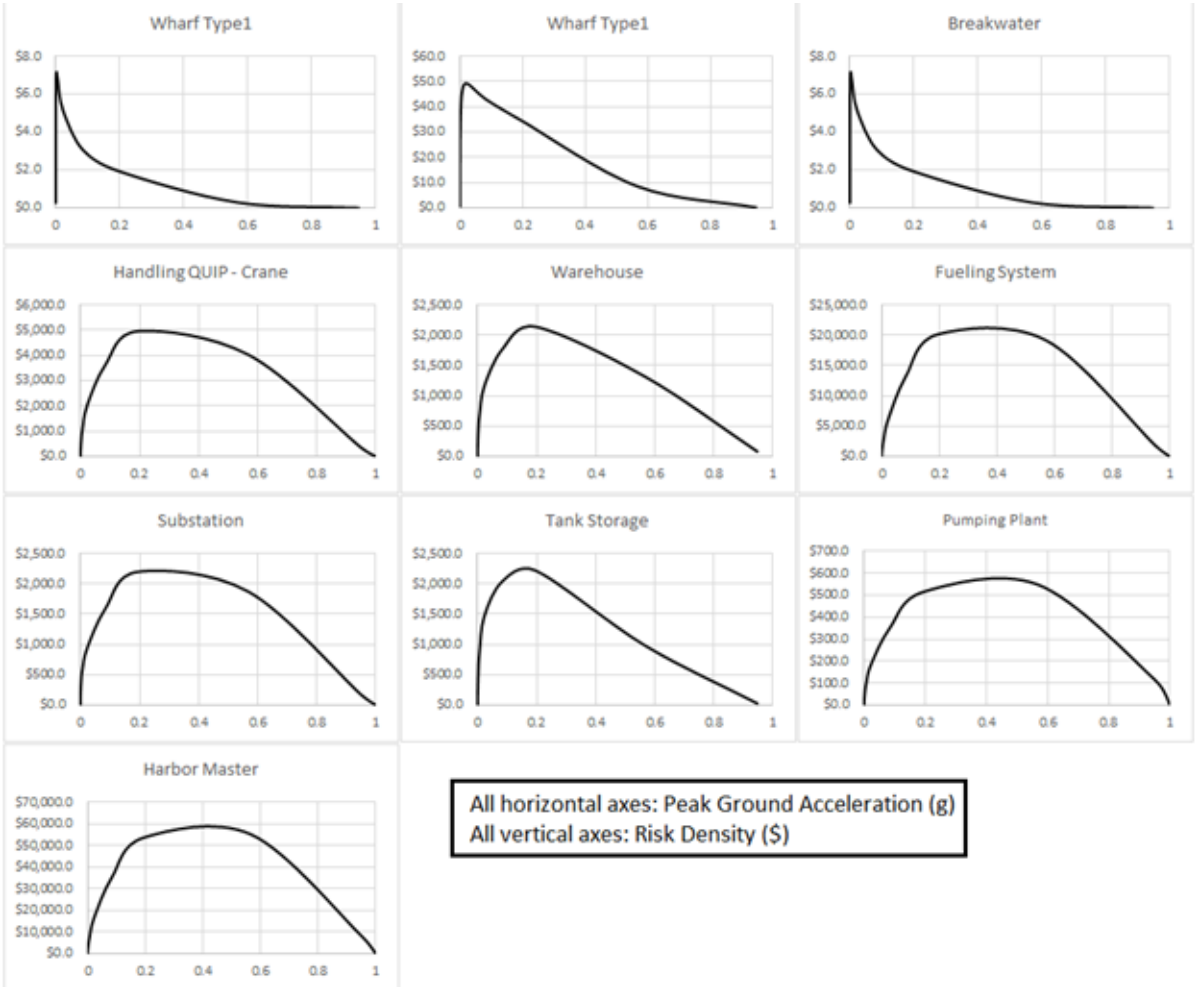

Figure 11: Seismic risk density curves for port equipment

Using the proposed methodology, the SRDCs were provided for different port structures. Because the SRDC curves for the breakwater and mooring structures type 1 and 2 have sharply-peaked risk density curves, they reflect appropriate seismic performance. Infrastructures such as storage tanks for liquids and cargo warehouses have hump-shaped risk density curves that denote average seismic performance. The curves for the pumping station, fueling system, cargo handling equipment, harbor master and power posts have elliptical risk density curves that denote weak seismic performance

5. Conclusion

The proposed methodology of comprehensive seismic risk assessment (CSRA) was used to extract the direct economic loss functions due to an earthquake for structures and equipment Pars Asaluyeh port. Figure 9 indicates that the minimum direct economic loss at low earthquake intensities was for the breakwater and mooring structures. At higher intensities, it was for pumping stations, power posts, and warehouses. It could be concluded that, at high earthquake intensities, the breakwater and mooring structures are more vulnerable than other port structures and will incur a higher cost for repair and recovery.

Seismic risk density curves (SRDCs) were used to accurately determine the seismic performance of the structures and equipment of Pars Asaluyeh port. The shapes of the SRDCs shown in Figure 11 indicate that the breakwater and mooring structures enjoy appropriate seismic performance and that the cargo handling equipment, pumping station, fueling system, harbor master, and power posts show weak seismic performance and require rehabilitation and retrofitting.

The conditional probability curves in Figure 7 for unserviceability of the port indicate that the infrastructure and cargo handling equipment are the cause of unserviceability. This conclusion agrees with engineering judgment in relation to the SRDCs.

6. Acknowledgements

The authors would like to thank the Pars Special Economic Energy Zone Organization for their financial support and their assistance in conducting this research. The authors also would like to thank Mr. Najafi, Director of Pars Asaluyeh Port, for his cooperation and patience during this research.

7. References

1. Okuyama, Y., D*isaster and economic structural change: case study on the 1995 Kobe earthquake.* Economic Systems Research, 2014. 26(1): p. 98-117.
2. Chang, S.E., *Transportation performance, disaster vulnerability, and long-term effects of earthquakes*. Second EuroConference on Global Change and Catastrophic Risk Management. Laxenburg, Austria, 2000.
3. Comartin, C.D., M. Greene, and S.K. Tubbesing, The Hyōgo-ken Nanbu Earthquake: *Great Hanshin Earthquake Disaster*, January 17, 1995: Preliminary Reconnaissance Report. 1995: Earthquake Engineering Research.
4. Na, U.J., S.R. Chaudhuri, and M. Shinozuka, P*erformance evaluation of pile-supported wharf under seismic loading*, in TCLEE 2009: Lifeline Earthquake Engineering in a Multihazard Environment. 2009. p .1-10.
5. Pachakis, D. and A.S. Kiremidjian, E*stimation of downtime-related revenue losses in seaports following scenario earthquakes*. Earthquake Spectra, 2004. 20(2): p. 427-449.
6. Pachakis, D. and A.S. Kiremidjian, *The use of simulation in disaster response planning and risk management of ports and harbors*, in Advancing Mitigation Technologies and Disaster Response for Lifeline Systems. 2003. p. 425-434.
7. Ichii, K., *Application of risk density analysis for seismic design: A gravity-type quay wall case .* WIT Transactions on Ecology and the Environment, 2004. 77.
8. Werner, S.D., S.E. Dickenson, and C.E. Taylor, *Seismic risk reduction at ports: Case studies and acceptable risk evaluation.* Journal of waterway, port, coastal, and ocean engineering, 1997. 1(6):23 p. 337-346.
9. Werner, S.D., et al. *Seismic risk analysis of Port of Oakland container berths. in Proc., 7th US National Conf. on Earthquake Engineering*. 2002. Earthquake Engineering Research Institute Boston.
10. Werner, S., G. Rix, and R. DesRoches. *Seismic risk management for seaports.* in 14th World Conference on Earthquake Engineering, Beijing, China. 2008.
11. Na, U.J. and M. Shinozuka, *Simulation-based seismic loss estimation of seaport transportation system.* Reliability Engineering & System Safety, 2009. 94(3): p. 722-731.
12. Amirabadi, R., et al., *Comprehensive Evaluation of Probabilistic Seismic Risk Methodology for Port Structures.* Journal of American Science, 2011. 7(7).
13. Burden, L.I., G. Rix, and S. Werner, *Development of a Risk Framework for Forecasting Earthquake Losses in Port Systems.* Earthquake Spectra, 2016. 32(1): p. 267-284.
14. Lam, J.S.L. and J.A. Lassa, *Risk assessment framework for exposure of cargo and ports to natural hazards and climate extremes.* Maritime Policy & Management, 2017. 44(1): p. 1-15.
15. Tavakoli, B. and M. Ghafory-Ashtiany, *Seismic hazard assessment of Iran. Annals of Geophysics*, 1999. 42(6).
16. Giardini, D., et al., *The GSHAP global seismic hazard map. Annals of Geophysics*, 1999. 42(6).
17. Werner, S.D., *Seismic guidelines for ports.* 1998: ASCE Publications.
18. Porter, K.A. *An overview of PEER's performance-based earthquake engineering methodology.* in Proceedings of ninth international conference on applications of statistics and probability in civil engineering. 2003.
19. Saygili, G. and E.M. Rathje, *Empirical predictive models for earthquake-induced sliding displacements of slopes.* Journal of Geotechnical and Geoenvironmental Engineering, 2008. 134(6): p. 790-803.
20. IIEES, *Seismic Hazard and Geotechnical Hazard Zonation of Assaluyeh (910 Hectare Area)*. 2001.
21. Hazus, E.L.E.M., *Technical manual. National Institute of Building for the Federal Emergency Management Agency*, Washington (DC), 1997.

INTERNATIONAL JOURNAL OF
COASTAL & OFFSHORE ENGINEERING
IJCOE Vol.5/No. 4/Winter 2020 (19-23)

Available online at: www. Ijcoe.org

Executive management engineering plans for comparison with tsunami damage

Mojtaba Zoljoodi [1], Reyhane Zoljoodi [2]

[1] faculty member and assistant professor, atmospheric science meteorological research center (ASMERC) m.zoljoodi@yahoo.com
[2] Bachelor candidate, Industrial Engineering, University of Tehran; reyhaneh.zoljoodi@ut.ac.ir*

ARTICLE INFO

Article History:
Received: 06 May. 2020
Accepted: 16 Aug. 2020

Keywords:
Tsunami
Makran
Storm
Tropical storm
Economy

ABSTRACT

A tsunami is a sea wave of local or distant origin that results from large-scale seafloor displacements associated with strong earthquakes, major submarine slides, or exploding volcanic islands. A tsunami can strike any coast at any time and we cannot predict exactly when or where they will occur. Undersea earthquakes most often cause tsunamis but submarine landslides or volcanic eruptions can also cause them. A tsunami can move as fast as a jet plane across the Open Ocean and can hit land with waves as high as 20 meters or more. The water may wash inland for several kilometers in flat lying areas, and can move up streams and rivers, destroying everything in its path. Waves may continue to strike the shoreline for many hours, and dangerous currents can continue for days following the event. Coastal areas endure Clear changes in response to ocean changes. The tsunami and tropical storms are among those changes. These changes should be note, Failure to pay attention to them makes opportunities become a threat. Tropical storms are one of the most dangerous hazards. In the first table some costs are mentioned.
When a tropical storm occurs, the water level along the waves in the sea changes. In these storms, strong winds are generated that revolve around a central core.it can move from ocean to coastal areas. The Makran seduction is due to the mountain range from Iran to Pakistan. The most important of these are Taftan and Bazman in Iran and Sultan in Pakistan. In hence The coastal area and sea play an important role in the development of country. Tropical storms and tsunamis are one of the most destructive phenomena in the world.it occurred in1945 in Iran, Mokran. The reason for this phenomenon was the large earthquake of 8.25 on the Mokran fault. This tsunami caused a lot of damage That killed more than 4,000 people in Pakistan. Tropical storms are important phenomena in the ocean area. The proper investment in different sectors and special attention to marine hazards and tsunami and also implementation of prevention plans are so necessary. Coastal areas influence economy by the knowledge of the potential of energy, transport, fisheries and tourism in addition to their political, strategic and social importance in the country's economy. Some plans are designed to reduce costs. Some of these programs are for training and some are to prevent damage. Financial limitation causes the need of prioritizing plans based on the knowledge of economical engineering in different periods of time. . In this case we present a modeling for prioritizing plans in order to Reduce the amount of Economical losses .with use NPV index to do the task .we have to calculate the amount of cost reduction for each plan. To find the extent of the damage reduction, 100 experts and organizations are surveyed and the results are estimated and then the cost of implementation of plans was found.
Historical accounts describe an earthquake and tsunami on 21 July AD 365 that destroyed cities and drowned thousands of people in coastal regions from the Nile Delta to modern-day Dubrovnik. The location and tectonic setting of this earthquake have been uncertain until now.

1. Introduction

The uplift of the sea floor associated with such an earthquake would have generated a damaging tsunami. There are multiple levels of tsunami hazard assessment (THA), including studies to investigate and document the frequency and severity of prehistoric and historic tsunami events, and numerical modeling studies with varying degrees of complexity.

It is obvious that hurricanes can have a destructive effect on reefs situated on the leeward sites of islands. However, also minor storms passing at relatively great distance can cause severe damage. Marine hazards along with damages to buildings and facilities have Economic and social impacts on human communities and coastal resident's malicious tsunamis are likely to occur in Iran. [Ref. 1] Marine risk management is the main way to reduce losses. That may cause the fishery industry to collapse. It may cause Loss of fishing line and loss of raw materials industries. Some costs are estimated in the table 1.

Table 1. costs of some type of hazards

Type of damage	Cost(dollar)
The amount of fish lost	31715517 $
The amount of shrimp lost	941875 $
Damage to boat and fishing boat	82144400 $
Damage to fishing boats	unknown
Production of canned fish	16500 $
Production of fish	11718750 $
Production of fish meal	296737357 $
Damage to other fishing infrastructure	unknown
Injuries to residents	unknown
Feeling insecure	unknown
Sum	423274399

Some losses cannot be estimated. We estimated these values using a survey of professors, experts, and organizations.

To prevent these damages, several schemes have been put forward, each with its own repercussions. These plans are explained in the chart below

Explanation of each plan to reduce costs of marine hazards:

- Plan1 Workshop for students of school
- Plan2 work shop for student of universities
- Plan3 workshop for people
- Plan4 Preventing human casualties
- Plan5 schedule for crisis from tsunami and costal storm
- Plan6 Forecast plan for merchant ships
- Plan7 Timely forecasting and notification
- Plan8 Pre-crisis Zone Management
- Plan9 Fire Fighting and Damage
- Plan10 Environmental Health and Disease Prevention
- Plan11 Emergency Communications in Crisis
- Plan 12 Establishing Public Securities in Times of Crisis (After Emptying Houses)
- Plan 13 Implementation of insurance plans for urban and rural activities Project
- Plan 14 Protections of Drinking Water Resources and Power Transmission Lines
- Plan 15 Reconstruction of urban and rural buildings and the last plan is to protect the artifacts
- Plan 16 to protect the artifacts

The country's budgetary constraint makes it necessary to prioritize projects. This prioritizing is based on engineering economy. Economical Costs of Possible Tsunami Damaging Sistan and Baluchestan province accounts for 40% of fishing industry in Iran. Physical units are the first step to estimate the direct effects of the damage. [Ref. 2] Indirect effects last up to two years. Indirect losses are losses of production capacity and loss of income. It can continue up to 4 or 5 years. Balance of payments, Inflation, and total employment. Table 2 shows the implementation cost of each plan. [Ref. 3]

Table 2. cost of each plan to reduce costs of marine hazards

Characteristic	Value
Workshop for school students	16 $
Workshop for university students	16 $
Workshop for people	84 $
Preventing human casualties	58 $
schedule for crisis	58 $
Forecast plan for merchant ships	41 $
Timely forecasting and notify	84 $
Pre-crisis Zone Management	41 $
Fire Fighting and Damage	84 $
Environmental health and Disease Prevention	58 $
Emergency Communications in Crisis	58 $
Establishing Public Security in Times of Crisis (After Emptying Houses)	58 $
Implementation of insurance plans	41 $
for urban and rural activities	100 $
Protection of Drinking Water Resources and Power Transmission Lines	116 $
Reconstruction of urban and rural buildings	167 $
protect the artefacts	58 $

[Ref. 4] [Ref. 5]

2. Results and Discussion

2.1.method

The purpose of this study is to examine plans to reduce losses. In Researches by National Iranian Oceanographic Research Institute Several plans are presented. Then, by NPV method the model was designed and prioritized. The NPV model is one of the most powerful indicators of macro decision making. It states for net present value . At first cost reduction for each plan is estimated in tabel 3.

To find the extent of the damage reduction, 100 experts and organizations were surveyed and the results were estimated as mentioned.

Table 3. Damage Reduction Due to Implementation of Each Project

Type of damage	Costs
• Plan1 Workshop for students of school	2000000
• Plan2 work shop for student of universities	2000000
• Plan3 workshop for people	4000000
• Plan4 Preventing human casualties	3000000
• Plan5 schedule for crisis from tsunami and costal storm	2000000
• Plan6 Forecast plan for merchant ships	1000000
• Plan7 Timely forecasting and notification	5000000
• Plan8 Pre-crisis Zone Management	7000000
• Plan9 Fire Fighting and Damage	10000000
• Plan10 Environmental Health and Disease Prevention	5000000
• Plan11 Emergency Communications in Crisis	100000000
• Plan 12 Establishing Public Security in Times of Crisis (After Emptying Houses)	20000000
• Plan 13 Implementation of insurance plans for urban and rural activities Project	30000000
• Plan 14 Protection of Drinking Water Resources and Power Transmission Lines	40000000
• Plan 15 Reconstruction of urban and rural buildings And the last plan is to protect the artifacts	55000000
• Plan 16 to protect the artifacts	10000000

Then By calculating NPV, each project is prioritized .

Net present value tells us what a stream of cash flows is worth based on a discount rate, or the rate of return needed to justify an investment. The profitability index helps make it possible to directly compare the NPV of one project to the NPV of another to find the project that offers the best rate of returning.npv is used in economic calculations and engineering economics and micro and macro economics.

2.2. Economical analyze

The last tsunami in the Makran area was 65 years ago. On average, tsunamis occur every 70 to 100 years. So the probability of a tsunami per year is between 1/70 and 1/100. As a result, the probability of a tsunami per year (p) is between two numbers.

$$0.01428571 > p > 0.01$$

X=Decision variable
W= Cost of implementing the project
S= The amount of the cost including the savings created by the plan
TC=(0.01428571x) si + wi
If yes $x = 1$
Otherwise x=0

Based on the figures presented in Table 1, with the implementation of the first plan and the second one it does not change the amount of costs widely but it can cause the reduction in psychological effects.

According to investment theories in the science of economic engineering, the following statements are defined:

Investments are called capital goods that increase the productive capacity of society.

In this discussion, the other can be said to be the implementation of a plan that empowers the region to face potential risks.

N.p.v net present value of any project is equal to the present value of project revenues minus the net cost of that project

If this indicator is positive, the project can be invested in. If N.p.v is negative, the investment will have a negative effect.

$$a = \frac{\mathrm{p}}{(1+i)} n$$

A= value of proceeds from the implementation of the plan at the present time
P= value of the proceeds of the project is the estimated interest rate per unit of project time
I= Interest rate per unit of project execution time
[Ref. 3]

n.p.v = TC – a

The larger the numerical value of the index above, the higher probability of implementation will be.
Since the inflation rate in Iran is 9.6, according to the report of the Central Bank of Iran, it is 0.8 monthly
The following calculations for the npv index are as mentioned (tabel4).

Table 4. NPV index calculation

plan	NPV index
• Plan1 Workshop for students of school	2499983300
• Plan2 work shop for student of universities	1/25E+11
• Plan3 workshop for people	9/83043E+14
• Plan4 Preventing human casualties	1/875E+12
• Plan5 schedule for crisis from tsunami and costal storm	4882812499
• Plan6 Forecast plan for merchant ships	2/44141E+15
• Plan7 Timely forecasting and notification	1/2207E+15
• Plan8 Pre-crisis Zone Management	1/70898E+15
• Plan9 Fire Fighting and Damage	2/44141E+15
• Plan10 Environmental Health and Disease Prevention	1/2207E+15
• Plan11 Emergency Communications in Crisis	2/44141E+15
• Plan 12 Establishing Public Security in Times of Crisis (After Emptying Houses)	4/88281E+15
• Plan 13 Implementation of insurance plans for urban and rural activities Project	7/32422E+15
• Plan 14 Protection of Drinking Water Resources and Power Transmission Lines	9/76562E+15
• Plan 15 Reconstruction of urban and rural buildings And the last plan is to protect the artifacts	1/34277E+16
• Plan 16 to protect the artifacts	2/44141E+15

At the result showed in table 5, First plan is a Workshop for students of school second is a work shop for students of universities
3rd plan is a workshop for people 4th plan is to prevent human casualties.5th plan is a schedule for crisis from tsunami and costal storm.
6th plan is a Forecast plan for merchant ships
7th plan Timely forecasting and notification.
Other priorities could be noticeable in special conditions.

Table 5. result (plans are mentioned respectively by priority)

priority	plan
first priority	• Plan4 Preventing human casualties
2th priority	• Plan11 Emergency Communications in Crisis
3th priority	• Plan 15 Reconstruction of urban and rural buildings And the last plan is to protect the artifacts
4th priority	• Plan 14 Protection of Drinking Water Resources and Power Transmission Lines
5th priority	• Plan 13 Implementation of insurance plans for urban and rural activities Project
6th priority	• Plan 12 Establishing Public Security in Times of Crisis (After Emptying Houses)
7th priority	• Plan9 Fire Fighting and Damage
8th priority	• Plan 16 to protect the artifacts
9th priority	• Plan6 Forecast plan for merchant ships
10th priority	• Plan8 Pre-crisis Zone Management
11th priority	• Plan7 Timely forecasting and notification
12th priority	• Plan10 Environmental Health and Disease Prevention

13th priority	• Plan3 workshop for people
14th priority	• Plan2 work shop for student of universities
15th priority	• Plan5 schedule for crisis from tsunami and costal storm
16th priority	• Plan1 Workshop for students of school

3. Conclusions

As we have seen, a plan to prevent human casualties is at the top priority. In times of crisis, a high percentage of costs will be reduced by implementing loss prevention and loss plan.The project is implemented by the Port Authority of the Police. The project cost $ 58 million. The next priority is the communication plan in the event of a crisis under the authority of the governor. Implementation of plans to deal with damages in a complex situation seems to be more efficient. This result is justified by the fact that marine hazards occur with less probability. Training programs are also usually long term.

Tsunamis and tropical storms rarely occur. But they cause a lot of damage. They can cause damage to various industries. Like the fishing and tourism industry. [Ref. 6] And because the coastal areas have the highest income through fishing some of these damages are irreparable. There were numerous ways to reduce costs, including training for different groups and prevention plan. 16 plans were designed in this area. First plan is Workshop for students of school Second is work shop for student of universities .3th plan is workshop for people 4th plan is to Preventing human casualties 5th plan is schedule for crisis from tsunami and costal storm.6th plan is Forecast plan for merchant ships.7th plan Timely forecasting and notification. Plan 8 Pre-crisis Zone Management. Plan 9 Fire Fighting and Damage .Plan 10 Environmental Health and Disease Prevention .Plan 11 Emergency Communications in Crisis .Plan 12 Establishing Public Security in Times of Crisis (After Emptying Houses).Plan 13 Implementation of insurance plans for urban and rural activities Project .14plan Protection of Drinking Water Resources and Power Transmission Lines ,Plan 15 Reconstruction of urban and rural buildings And the last plan is to protect the artifacts. Due to budget constraints, not all projects can be implemented. According to studies the plan "to prevent human casualties in times of crisis" is the first priority to implement. But training plans are also needed. Although training plans are in the thirteenth and fourteenth priorities. It looks like it should be merged with the fourth plan. So by weighing the issue of education and awareness and The Impact of Content and its Quality on Planning Workshops and informing the general public, especially education in schools and universities all priorities are important. [Ref. 7] The plan of emergency communications is also a second priority in times of crisis. So it will economically comply with the following table but the above mentioned content should be notice. [Ref. 8] [Ref. 9]

4. References

1- M.Heydar zadeM.D.Pirooz N.Zakeri, Ahmet C. Yalciner, Mohammad Mokhtari ,Asad Esmaeily (2008), *Historical tsunami in the Makran Subduction Zone off the southern coasts of Iran and Pakistan and results of numerical modeling*, Journal of Computational Physics, p.775-781.

2- Heydarzadeh, M., Dolatshahi Pirouz, M., Hajizadeh Zaker, N (2007), *evaluation the potential for tsunami in southern Iran*, international journal of civil engineering vol 4, p. 314-327

3- Hamidreza Mirzaei1, Bijan Yavar, Maisam Mirtaheri (2010), *Chabahar Free Trade & Industrial Zone (CFZ) Disaster Management Information System*, International Journal of Heat and Mass Transfer, p.1-3

4- M.s. sarkar(2018),), *Numerical modeling of tsunami in the Makran Subduction Zone – A case study on the 1945 event*, Journal of Operational Oceanography,Vol 12, p. 1-3.

5- S. Madani, S Khaleghi, M.R Akbarpour Jannat, (2017), *Assessing building vulnerability to tsunami using the PTVA-3 model: A case study of Chabahar Bay, Iran*, Natural Hazards.

6- M.M Beigi Kasvaei1, M.H Kazeminezhad, Abbas Y.Bakhtiary,(2019), *Numerical Study on Wave Induced Flow Field around a Vibrant Monopile Regarding Cross-Sectional Shape*, International journal of costal and offshore engineering. Vol3, p. 1-9.

7- S.Madani (2014)**,** *Damage Services Limitation of a possible tsunami in the Chabahar Bay section of the area*, International Conference on Sustainable Development, Strategies and Challenges Focusing on Agriculture, *Natural Resources*, Environment and Tourism, P .1-8.

8- S.Madani (2012), *Economic potentials of Iranian coasts in the direction of sea-based development*, 14th Marine Industry Conference, p. 1-10.

9-V. Khorsandi far, E.Shad (2014), *Understanding the environmental conditions of Makran beaches and modeling tropical storms for the development and operation of southern ports*, 10th Congress of Pioneers of Progress, p.1-7.

INTERNATIONAL JOURNAL OF
COASTAL & OFFSHORE ENGINEERING
IJCOE Vol.5/No. 4/Winter 2020 (25-33)

Available online at: www. Ijcoe.ir

Pile Apparent Fixity Length Estimation for the Jacket-type Offshore Wind Turbines under Lateral Loads Applicable to Fatigue Analysis

Amirarsalan Shahmohammadi[1], Naser Shabakhty[2*]

[1]*Department of Marine Structures, Science and Research Branch, Islamic Azad University, Tehran, Iran; a.shahmohammadi@srbiau.ac.ir*
[2*]*School of Civil Engineering, Iran University of Science and Technology, Tehran, Iran; Shabakhty@iust.ac.ir*

ARTICLE INFO

Article History:
Received: 16 Apr. 2020
Accepted: 08 Sep. 2020

Keywords: Offshore wind turbine; Jacket; Soil-pile interaction; fixity length; lateral loading

ABSTRACT

Modelling the soil-pile interaction using the Finite Element Method (FEM) might be a time-consuming process and required entirely specific soil properties. Moreover, most of the codes that have been developed for offshore wind turbines use one or more of some simplified linear foundation models suitable for dynamic analysis such as Apparent Fixity (AF) model. In the AF model for pile foundation systems, a fixity length level below the seabed is designated for the pile. It is assumed that the whole structure, including the pile and support structure, is cantilevered at the corresponding fixity length level without surrounding soil while has identical behavior to a pile penetrated the real soil. In this study, the apparent fixity length of the piles sustaining the OC4 offshore wind turbine on the seabed is estimated using a nonlinear soil-pile interaction analysis following a dynamic response analysis of the structure under lateral loads during turbine power production. Given the stiffness coefficients of the pile heads, different apparent fixity lengths are obtained, and the minimum one, verified by modal analysis, is also determined, which can be presumed in fatigue analysis. It is also demonstrated that the estimated minimum fixity length has a smaller value than the piles' critical length.

1. Introduction

Finding new energy resources, especially clean and renewable ones, have always been among the human's main concerns since the late 20th century. Wind energy is a sort of renewable and clean resources and is used to generate electrical power by application of wind turbines. Wind turbines, in terms of place of operation, are classified into onshore and offshore wind turbines (OWT). A wind farm is set up when several OWTs are placed at a specified location together. Since the earliest offshore wind farm was installed in Denmark in the 1990s, the development of this technology to achieve more reliable electrical power with reasonable cost has been the main purpose of experts involving in the offshore industry [1]. OWTs have various types of foundation systems and are designed considering different water depths, environmental conditions, and seabed soil properties. They are generally distinguished by their foundation systems, namely fixed and floating types. Monopile, jacket, tripod, and gravity-based foundations are fixed OWT and semi-sub, TLP, and spar foundation systems are those used as floating. Investigation of soil-pile interaction for fixed OWT is a complicated task and required nonlinear analyses. In order to assure the results are highly accurate, the Finite Element Method (FEM) is extensively used to examine soil-pile interaction using soil properties such as p-y curves. These curves are yielded from in-situ experiments, whereas some simplified methods approximately lead to reasonable outcomes concerning soil-pile interaction. In this regard, Bush and Manuel [2] investigated the effects of applying four different monopile foundation models for offshore wind turbines, including Fixed-Base (FB) and Flexible in shallow waters subjected to extreme loads with return periods of 20 years. Flexible models include the apparent fixity (AF) model, the Coupled Springs (CS) model, and the Distributed Springs (DS) model. In the FB model in which the structure connected rigidly to the seabed, the soil profile is not taken into account. In the AF model, the pile is assumed as a cantilever beam continued downward the seabed and fixed at a specific level where the pile has identical behaviour to the case in which it is embedded into the real soil profile. In the CS model, coupled rotational and translational springs on pile tip – seabed level – demonstrate the soil behaviour. In the DS model, linear elastic springs are placed along the pile and represent soil layers' stiffness values. These models are based on a study by Jonkman et al. [3] through which some simplified linear

foundation models derived by the Endowed Chair of Wind Energy (SWE) at the University of Stuttgart in Germany, appropriate to use in a dynamic analysis, have been presented. The use of the AF model is always accompanied by a challenging issue, to what length the pile has to be fixed below the seabed level. According to Barltrop and Adams [4], rough approximations to the apparent fixity lengths are 3.5D - 4.5D for stiff clays, 7D - 8.5D for very soft silts, and 6D in the general analyses where D is the pile diameter. This may, however, vary owing to different soil properties. Furthermore, given that each location has its particular sea states and environmental load conditions, it seems more rational to estimate an adequate specific apparent fixity length for each case. Akdag [5] performed an investigation of an alternative pile foundation for jacket OWT in Mustang Island with closely spaced double piles at the edge of the jacket, which led to a reduction in piles embedment length up to 50 %. Wei Shi et al.[6] investigated the effect of the soil-structure interaction on the response of an offshore wind turbine with a jacket-type foundation. They considered two different models of flexible foundation - the p-y model and the p-y model considering pile groups effect - to compare the dynamic responses with the fixed-base model. Moreover, they showed that influence of the soil-structure interaction on the response of the jacket foundation predicts that the flexible foundation model is necessary to estimate loads of the offshore wind turbine structure accurately. Khodair and Abdel-Mohti [7] studied soil-pile interaction for a composite pile using FEM and Finite Difference (FD) method. They used *Abaqus* and *SAP2000* for FEM and *LPILE* for the FD method. They found, finally, a close correlation between the results obtained by the FEM and the FD solution. Furthermore, the effect of applying an axial load to the pile on the produced bending moment and lateral displacement along the depth was minimal and negligible. The effect of the seabed slope on the piles' behaviour of a fixed offshore platform under lateral loads was investigated by Muthukkumaran and Arun [8]. Their results indicated that the lateral displacement at the pile tip, the seabed level, increases with the seabed slope. In the present study, initially, an aero-hydro-servo-elastic simulation of the OC4 offshore wind turbine [9] supported by a FB jacket is carried out using FAST [10]. Operational load conditions considering the fatigue analysis, which is the further concern of this study, are used to obtain the time history of shear forces and flexural moments at the sea bed level -leg bottoms. Subsequently, nonlinear soil-pile interaction analyses under lateral excitations are conducted using LPILE [11], which leads to piles lateral deflections given that penetration depth and the pile heads stiffness matrices. Ultimately, the apparent fixity lengths for the piles are estimated using Euler-Bernoulli beam theory and the minimum applicable fixity length verified by modal analysis is chosen.

2. Modelling Considerations

The reference jacket "UPWIND" described by Vorpahl and Popko [12] supporting a 5MW baseline wind turbine [13], developed at the National Renewable Energy Laboratory (NREL) of the United States, is considered here as a case study. It has a hub with a diameter of 3 meters located 90.55 meters upward from the mean sea level. Rotor diameter and mass are 126 meters and 110000 kg, respectively, with a rated speed of 12.1 rpm. Besides, it has a cut-in and a cut-out wind speed of 3 and 25 m/s, respectively, where the rated wind speed is between these two with a value of 11.4 m/s. A conical linearly tapered tower with a length of 68 meters and diameters of 4 and 5.6 meters at the top and the end, respectively, is connected to the rotor and nacelle assembly (RNA). There is, also, a Transition Piece (TP), a concrete block with a mass of 666 t and dimensions of 4×9.6×9.6 meters placed at the elevation 16.15 meters upward from mean sea level onto the jacket. A four-legged jacket with a length of 66.15 meters excluding the part penetrated the TP (70.15 meters, including TP) supports the RNA and tower in a water depth of 50 meters. It is fixed on the seabed using four steel piles with an outer diameter of 2.082 meters embedded through the seabed with a penetration depth of 45 meters. Figure 1 represents the corresponding OWT mentioned above.

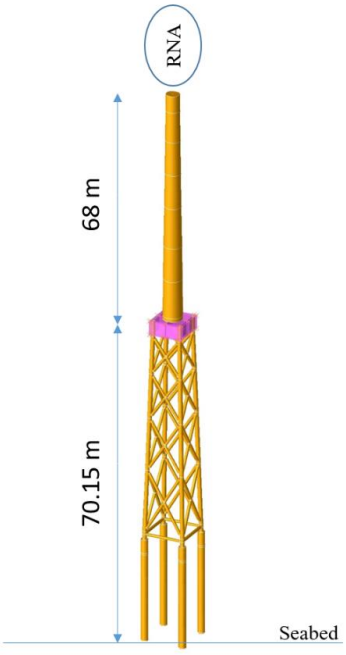

Figure 1. 5MW jacket-type OWT configuration

The soil profile used in this study is entirely based on the Upwind design basis presented by Fischer et al.[14] in which two different API-Sand [14-16] profiles, namely hard and soft, are presented. Soil parameters, including soil buoyant unit weight y', internal friction angle φ, and the undrained shear strength Cu within the

soil layers, can be found in table 1. The soft profile is taken into account here- as a conservative point of view. In order to simulate the OWT, FAST v.8 [17] is used, and as for the nonlinear soil-pile interaction analysis, the LPILE programme is adopted.

Table 1. Soil Profile Properties

Depth (m)	y' (KN/m^3)	Φ (degree)	Cu (Pa)
0-3	10	36	-
3-5	10	33	-
5-7	10	26	60000
7-10	10	37	-
10-15	10	35	-
15-50	10	37.5	-

3. Dynamic Response Analysis

In order to obtain time histories of shear forces and flexural moments at leg bottoms in the FB model, dynamic response analysis is required. In this regard, FAST v.8 is used to simulate all aerodynamics and hydrodynamics aspects of environmental loads on OWT within the power production for 630 seconds. It should be noted that, according to Jonkman and Buhl [10] and Jonkman [18], the first 30 seconds are neglected to eliminate start-up transition behaviour as the system is assumed asymptotically stable. Since the ultimate purpose of the present study is fatigue damage analysis, from the first design situation, namely power production, second Design Load Case (1.2 DLC), which is the only one to be analysed in Fatigue Limit State (FLS), recommended by IEC 61400-3 [19] and given in the Upwind project design basis, must be considered for the simulations here. According to IEC 61400-3, concerning the 1.2 DLC; a Normal Turbulence model (NTM) with a turbulence intensity of 0.14 [14] as well as the joint probability distribution of the corresponding significant wave heights H_s, peak spectral period T_p and wind speed at hub height V_{hub} for the normal sea state are considered. The corresponding three-dimensional joint probability distribution is presented by Fischer et al.[14]. Moreover, based on the 1.2 DLC descriptions in IEC 61400-3, currents effects are neglected, and the wind and wave are aligned in terms of direction (co-directional). The structure is subjected to wave and wind loads from the direction of 0˚ [20, 21], as seen in figure 2. According to the Upwind project design basis, a lumped scatter diagram, including 17 different sea states, should be taken into account for fatigue analysis. However, as the primary purpose of the present study is estimating the apparent fixity length of the piles under operational load conditions and not to estimate the fatigue damage, all the 17 sea states are not considered as it is quite time-consuming. Instead, two sea states with the most frequency of occurrence within wind turbine service time were chosen based on the joint probability distribution given by the Upwind design basis. Also, as the cut-out wind speed for the 5MW offshore wind turbine is 25 m/s, one more sea state with V_{hub}[1] $= 24$ m/s is taken into consideration to cover the highest wind speed before the turbine shutdown. Table 2 shows the selected sea states properties. Regarding the wind spectrum, the Kaimal wind speed density spectrum is commonly used for offshore wind energy applications [22]. Also, the Power Law wind profile is used here for mean wind speed. Moreover, aerodynamic power is sensitive to blade pitch angle [23-25]. Once the wind speed exceeds the optimal 5MW turbine's speed, which is 11.4 m /s, the initial pitch angle of the blades (0°) will increase by the pitch controller relative to the corresponding wind speed. As a result, there will be different pitch angles that are proportional to the wind speeds up to the cut-out speed. These angles given by Jonkman et al. [13] are applied to the FAST's blades and rotor analysis module, namely ElastoDyn. As for the present study, only two wind speeds, 12 and 24 m/s are subject to change pitch angle to 3.83° and 22.35°, respectively.

Table 2. Sea States Properties

Sea state	V_{hub} (m/s)	H_s (m)	T_p (sec)
1	8	1	6
2	12	1.5	6
3	24	3.5	8

In order to generate stochastic waves and wind fields, wave and wind random seeds number for each particular simulation have to be changed. Turbulent wind fields are generated via TURBSIM [26] in which each random wind seed is changed by adding a small constant value for each simulation. Likewise, the same process is undergone in FAST to generate stochastic waves. As this procedure could be continued infinitely, a sufficient number of simulations need to be determined. Therefore, a statistical convergence criterion was considered, which could indicate the maximum number of simulations needed for each sea state as well as making our model uncertainty as least as a reasonable amount. Statistical criteria such as mean value, standard deviation, and skewness were investigated for each of the output results of simulations. Despite their variations were small comparing each other, it was not that convincing regarding our purpose. Hence the coefficient of variation (COV) of the output of the simulations –

Shear forces and Flexural moments – was obtained looking for results with equal or less than 5%. The results were reasonably acceptable after **eight simulations for sea state 1, eight simulations for sea state 2, and five simulations for sea state 3**. As it is

[1] Wind speed at hub height

shown in table 3, approximately all the values are less than 5%, which is quite reasonable in engineering problems.

Table 3. COV of the shear forces (F) and flexural moments (M) at jacket legs bottom

Sea state	F %	M %	F %	M %	F %	M %	F %	M %
1	5.11	4.93	3.78	3.67	3.42	3.71	2.75	3.02
2	1.61	1.70	1.09	1.19	1.33	1.50	0.91	1.08
3	2.10	2.20	1.13	1.12	1.26	1.45	0.74	0.88
Loc.	Leg bottom 1		Leg bottom 2		Leg bottom 3		Leg bottom 4	

4. Nonlinear Soil – Pile Interaction Analysis

As mentioned earlier, the investigation of the soil-pile interaction under applied lateral loads is required in order to find an adequate apparent fixity length of the piles. According to Randolph and Gourvenec [27] and Det Norsk Veritas (DNV) [28], Lateral loads applied to offshore wind turbines are broadly dominant for anchor piles and monopile foundations. In contrast, for jacket support structures, the piles are mainly axially loaded. Furthermore, it is also mentioned in DNV that in dynamic analysis for pile foundation systems, p-y curves are used to show soil-pile interaction, which means lateral loading would have a pivotal role in pile foundation systems. Thus soil-pile interaction analyses were conducted under lateral excitations using LPILE - known as a programme able to perform nonlinear soil-pile interaction analyses. Piles arrangement is shown in figure 2. The SubDyn module, which is responsible for dynamic structural analysis in FAST, can output either static components or dynamic components rather than the actual reaction loads, which cannot be computed efficiently for lattice structure with closed loops. The static components, however, are usually quite close to true reaction loads [29]. Thus, they are used here as shear forces and flexural moments time histories at the legs bottom yielded from FAST simulations of the FB jacket support structure. As the legs bottom are aligned with pile heads, the phrase “pile head” will be using in the following. More than 12 thousand contemporaneous shear forces and moments corresponding to each time step yielded from every single simulation and taking into account all of them was a laborious process. Therefore they were used to plot bivariate histograms via MATLAB [30] looking for the most frequent coupled shear force-flexural moment applied to the legs bottom. One of such histograms can be seen in figure 3.

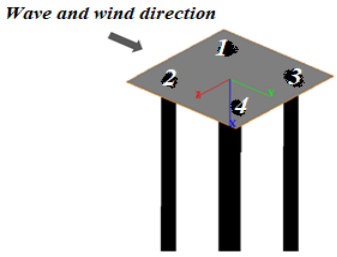

Figure 2. Piles arrangement to wave and wind direction

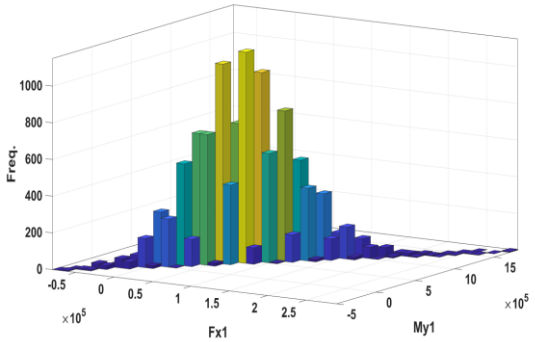

Figure 3. Sim.1, Sea state 1, coupled shear force (F)-flexural moment (M) histogram

The most frequent bins of the coupled shear forces and flexural moments containing more than one thousand values were found. The midpoints of the bins (F_x, M_y) are taken as the corresponding simulations indicator of the shear forces and flexural moments applied to each pile head. The midpoints are the obtained medians of the shear forces and moments relevant to each pile head corresponding most frequent range. Tables 4-6 represent the midpoint values for each simulation.

Table 4. Midpoint values - sea state 1

Simulation	Case	Leg bottom 1	Leg bottom 2	Leg bottom 3	Leg bottom 4
1	Shear force (N)	7.44E+04	8.55E+04	1.15E+05	1.15E+05
	Moment (N.m)	4.71E+05	5.35E+05	6.46E+05	6.44E+05
2	Shear force (N)	7.46E+04	8.47E+04	1.15E+05	1.15E+05
	Moment (N.m)	4.70E+05	5.33E+05	6.43E+05	6.45E+05

3	Shear force (N)	6.98E+04	6.99E+04	1.30E+05	1.30E+05
	Moment (N.m)	4.41E+05	4.41E+05	7.38E+05	7.31E+05
4	Shear force (N)	5.51E+04	6.99E+04	1.15E+05	1.29E+05
	Moment (N.m)	3.48E+05	4.40E+05	6.43E+05	7.32E+05
5	Shear force (N)	7.52E+04	7.02E+04	1.15E+05	1.15E+05
	Moment (N.m)	4.69E+05	4.44E+05	6.44E+05	6.44E+05
6	Shear force (N)	7.49E+04	5.52E+04	1.15E+05	1.15E+05
	Moment (N.m)	4.72E+05	3.47E+05	6.46E+05	6.44E+05
7	Shear force (N)	5.52E+04	7.52E+04	1.16E+05	1.15E+05
	Moment (N.m)	3.45E+05	4.72E+05	6.45E+05	6.42E+05
8	Shear force (N)	7.05E+04	7.02E+04	1.30E+05	1.10E+05
	Moment (N.m)	4.40E+05	4.41E+05	7.38E+05	6.11E+05

Table 5. Midpoint values - sea state 2

Simulation	Case	Leg bottom 1	Leg bottom 2	Leg bottom 3	Leg bottom 4
1	Shear force (N)	1.11E+05	1.11E+05	1.70E+05	1.51E+05
	Moment (N.m)	6.73E+05	6.73E+05	9.68E+05	8.44E+05
2	Shear force (N)	1.50E+05	1.10E+05	1.90E+05	1.70E+05
	Moment (N.m)	9.18E+05	6.70E+05	1.09E+06	9.65E+05
3	Shear force (N)	1.10E+05	1.10E+05	1.50E+05	1.50E+05
	Moment (N.m)	6.67E+05	6.68E+05	8.44E+05	8.39E+05
4	Shear force (N)	1.10E+05	9.11E+04	1.70E+05	1.50E+05
	Moment (N.m)	6.71E+05	5.49E+05	9.69E+05	8.43E+05
5	Shear force (N)	1.10E+05	1.10E+05	1.50E+05	1.50E+05
	Moment (N.m)	6.72E+05	6.73E+05	8.46E+05	8.39E+05
6	Shear force (N)	1.10E+05	1.10E+05	1.15E+05	1.15E+05
	Moment (N.m)	6.67E+05	6.71E+05	1.50E+05	1.50E+05
7	Shear force (N)	1.10E+05	1.10E+05	1.50E+05	1.50E+05
	Moment (N.m)	6.68E+05	6.72E+05	8.42E+05	8.41E+05
8	Shear force (N)	1.10E+05	1.11E+05	1.70E+05	1.51E+05
	Moment (N.m)	6.64E+05	6.72E+05	9.69E+05	8.41E+05

Table 6. Midpoint values - sea state 3

Simulation	Case	Leg bottom 1	Leg bottom 2	Leg bottom 3	Leg bottom 4
1	Shear force (N)	7.48E+04	4.60E+04	1.34E+05	1.05E+05
	Moment (N.m)	4.77E+05	2.85E+05	7.73E+05	5.83E+05
2	Shear force (N)	7.52E+04	4.66E+04	1.35E+05	1.35E+05
	Moment (N.m)	4.72E+05	2.87E+05	7.76E+05	7.74E+05
3	Shear force (N)	7.54E+04	4.59E+04	1.36E+05	1.34E+05
	Moment (N.m)	4.75E+05	2.87E+05	7.76E+05	7.66E+05
4	Shear force (N)	7.42E+04	7.56E+04	1.65E+05	1.06E+05
	Moment (N.m)	4.69E+05	4.77E+05	9.63E+05	5.77E+05
5	Shear force (N)	7.47E+04	7.47E+04	1.35E+05	1.34E+05
	Moment (N.m)	4.78E+05	4.71E+05	7.75E+05	7.69E+05

Midpoint values are used as load cases in the LPILE to simulate soil-pile interaction for each sea state. Piles lateral deflections and the pile heads stiffness matrices were yielded from LPILE. Lateral deflections of the piles within the penetration depth are shown in figures 4-7.

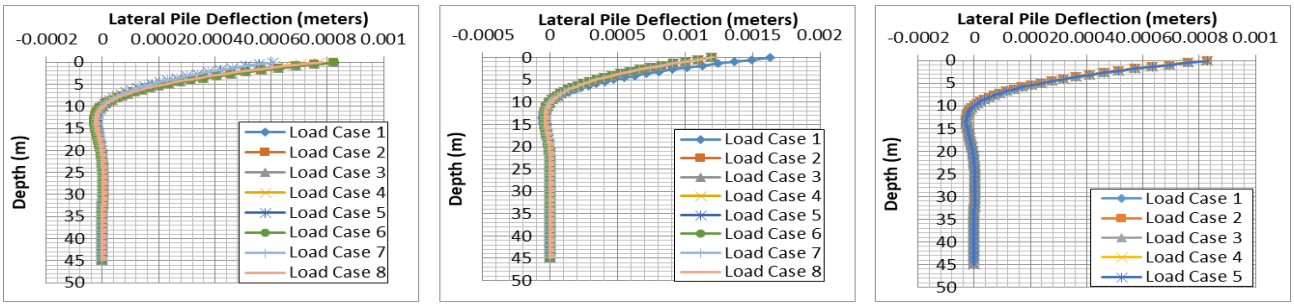

Figure 4. Pile 1 lateral deflections under sea state 1(A), 2(B), 3(C)

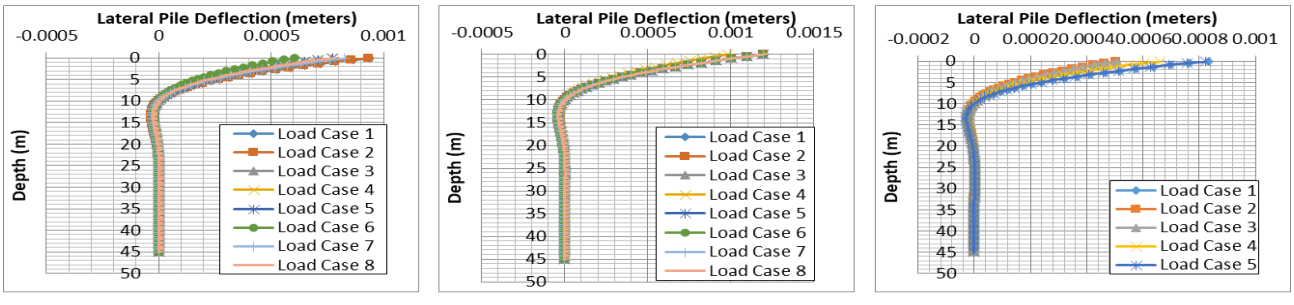

Figure 5. Pile 2 lateral deflections under sea state 1(a), 2(b), 3(c)

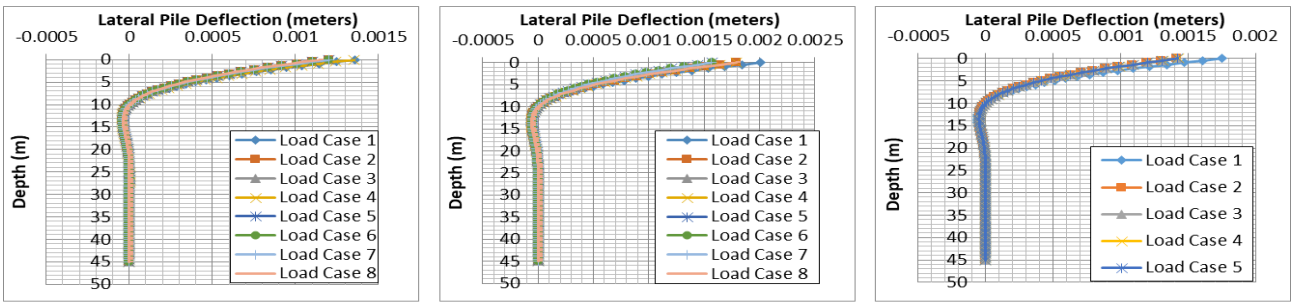

Figure 6. Pile 3 lateral deflections under sea state 1(A), 2(B), 3(C)

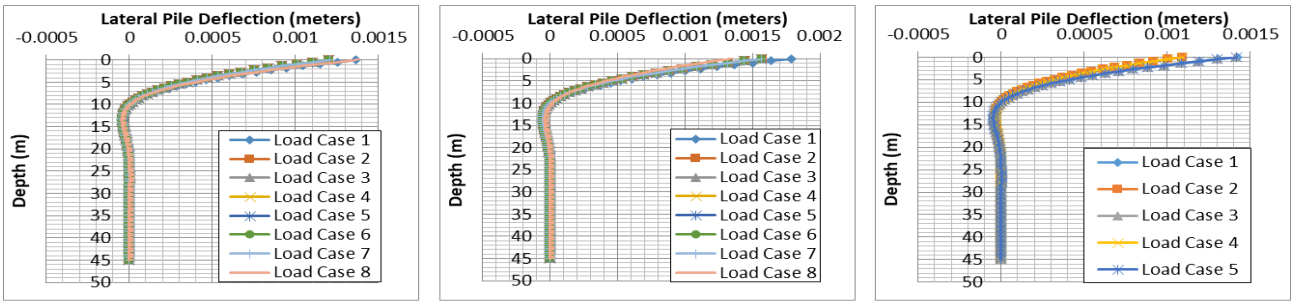

Figure 7. Pile 4 lateral deflections under sea state 1(a), 2(b), 3(c)

As it was mentioned earlier, in the AF model, the pile is presumed to be penetrated the seabed and fixed at a level where the same behaviour of the pile embedded in real soil is expected. As only translational and rotational displacements are involved, the pile heads 2×2 stiffness matrices (Eq.1) are obtained via LPILE. Moreover, it can be seen that the piles' deflections are quite small to the piles' lengths. Thus the Euler-Bernoulli beam theory would apply to the piles. As a result, the obtained matrices can be equalized to a two degree of the freedom stiffness matrix of a cantilevered Bernoulli beam (Eq.2) to find the apparent fixity length of the piles.

$$\begin{bmatrix} K_{22} & K_{23} \\ K_{32} & K_{33} \end{bmatrix} \begin{bmatrix} w \\ \theta \end{bmatrix} = \begin{bmatrix} F \\ M \end{bmatrix} \quad (1)$$

$$\begin{bmatrix} \frac{12EI}{L^3} & -\frac{6EI}{L^2} \\ -\frac{6EI}{L^2} & \frac{4EI}{L} \end{bmatrix} \begin{bmatrix} w \\ \theta \end{bmatrix} = \begin{bmatrix} F \\ M \end{bmatrix} \quad (2)$$

As for equations 1 and 2, *w*, *θ, F*, *M* are translational displacement, rotational displacement, applied shear force, and flexural moment, respectively. Also, K_{22}, K_{23}, K_{32}, K_{33} indicate stiffness coefficient related to shear force, coupled shear force-moment, coupled moment-shear force, and moment applied to the pile head taking the values 434775 KN/m, 1837296 KN/rad, 1836188 KN-m/m, 12951078 KN-m/rad, respectively. It should be noted here, as the piles' deflections were quite small under each state, the stiffness coefficients – obtained from LPILE – were the same for each sea state. The bending stiffness (*EI*) obtained from LPILE, also, is held constant along the piles and takes a value of 4.02×10^7 KN.m^2.

5. Results and Discussion

Pile heads, and cantilevered Euler-Bernoulli beam stiffness matrices (Eq.1, Eq.2) were equalized assuming that applied shear forces and flexural moments (*F*, *M*) to the pile heads are the same in both FB jacket and a flexible one. Nonetheless, the loads experienced by the FB model at the legs bottom (pile heads) are not the same as those applied to a flexible model in reality. According to Bush and Manuel [2] – given that the *OC4* project soil properties – the statistical criteria such as standard deviations and mean values of shear forces and flexural moments at pile heads are altered less than one per cent comparing FB model to flexible model. As a result, the translational and rotational displacements (*w*, *θ*) are taken similar for both stiffness matrices above. Hence the first terms of Eq.1 and Eq.2 should be equal, and they can be written as Eq.3.

$$\begin{bmatrix} \frac{12EI}{L^3} & -\frac{6EI}{L^2} \\ -\frac{6EI}{L^2} & \frac{4EI}{L} \end{bmatrix} = \begin{bmatrix} K_{22} & K_{23} \\ K_{32} & K_{33} \end{bmatrix} \quad (3)$$

Eventually, the apparent fixity lengths (*L*) corresponding to each stiffness coefficient were obtained which are given in table 8

Table 7. Estimated apparent fixity lengths for different stiffness coefficients

Stiffness coefficient	Apparent fixity length (m)
$\mathbf{K_{22}}$	10.35 (~ 5D)
$\mathbf{K_{23}}$	11.46 (~ 5.5D)
$\mathbf{K_{32}}$	11.45 (~ 5.5D)
$\mathbf{K_{33}}$	12.41 (~ 5.96D)

Modal analyses were performed via BMODES [31]- a Finite Element (FE) code for modal analysis of blades and tower- for different apparent fixity lengths looking for the natural frequency of the structure. The fixity length values recommended by Barltrop and Adams, 6D for general calculations, and 8D as a mean value for soft soil profiles, are considered as well as the values yielded from this study – presented in table 7. Modal analysis results are presented in Table 8.

Table 8. Natural frequencies of the structure for different pile fixity length

Apparent Fixity Length (m)	Structure Natural Frequency (Hz)
6D (12.46)	0.309
8D (16.64)	0.303
5D (10.35)	0.430
5.5D (11.46)	0.426
5.5D (11.45)	0.428
5.96D (12.41)	0.311

According to the Upwind final report [32], the structural natural frequency of the OC4 offshore wind turbine supported by a jacket should be in a range between 0.222 Hz and 0.31 Hz. Apart from the fixity length of 6D and 8D, 5.96D (12.41 m) is the only fixity length, which leads to a natural frequency appropriate to the interval mentioned above. It can be seen that it is the minimum apparent fixity length of the piles that would be adjusted concerning the corresponding natural frequency of the structure.

6. Summary and Conclusions

This paper presents a method to estimate adequate apparent fixity length for the piles in OC4 OWT under lateral loading, taking into account nonlinear soil-pile interaction. Initially, a FB jacket substructure for OC4 OWT is assumed and simulated under Normal load conditions using FAST to obtain the dynamic response of the structure. Subsequently, load reactions at the legs bottom are considered as applied loads to the pile-heads in order to conduct nonlinear soil-pile interaction analysis in a geotechnical programme, namely LPILE. As a result, piles lateral deflection and stiffness matrices of the pile heads are obtained. Pile heads stiffness matrices are individually compared with the stiffness matrix of a cantilevered Bernoulli beam at its free head to find the apparent fixity length of the piles. Concerning each stiffness coefficient, a particular fixity length is obtained. It observed that the piles had deflected increasingly up to 13 meters of depth below the seabed. Afterwards, the deflection descended until they have almost returned to the preloaded condition. Additionally, several modal analyses were conducted for the structure considering different piles' fixity length. Apart from fixity lengths of 6D and 8D, which are extensively used in literature, 5.96D (12.41 m) was the only fixity length, which leads to a natural frequency compatible with the allowable interval given by OC4 OWT design basis. In other words, according to the natural frequencies, the minimum apparent fixity length for lateral loading condition was considered as $L_{AF} = 12.41$ meters downward the seabed. Besides, among the obtained fixity lengths, this level is the closest value to 13, where the piles stop to deflect. Therefore, it can be concluded that the adequate piles' apparent fixity length for the OC4 OWT under lateral loading during power production can be chosen from one of the following values: 6D (12.46m) and 8D (16.64m), recommended by Barltrop and Adams, and the minimum length of 5.96D (12.41m) proven in this study and they are all suitable assumptions applicable to fatigue analysis when lateral loading is dominant.

Acknowledgement

The authors gratefully acknowledge Dr Jason Jonkman at the National Renewable Energy Laboratory (NREL) of the United States for his supports and recommendations with the FAST code and the 5 MW wind turbine model utilized in this study.

List of Symbols

EI	Bending stiffness
k	Stiffness coefficient
W	Translational displacement
θ	Rotational displacement
F	Shear force
M	Flexural moment
H_s	Significant wave height
T_p	Spectral period
V_{hub}	Wind speed at hub height
COV	Coefficient of variation

8. References

1. Ng, C. and L. Ran, *Offshore wind farms: Technologies, design and operation*. 2016: Woodhead Publishing.
2. Bush, E. and L. Manuel. *The influence of foundation modeling assumptions on long-term load prediction for offshore wind turbines*. in *ASME 2009 28th International Conference on Ocean, Offshore and Arctic Engineering*. 2009. American Society of Mechanical Engineers.
3. Jonkman, J., S. Butterfield, P. Passon, T. Larsen, T. Camp, J. Nichols, J. Azcona, and A. Martinez, *Offshore code comparison collaboration within IEA wind annex XXIII: phase II results regarding monopile foundation modeling*. 2008, National Renewable Energy Lab.(NREL), Golden, CO (United States).
4. Barltrop, N.D. and A.J. Adams, *Dynamics of fixed marine structures*. Vol. 91. 2013: Butterworth-Heinemann.
5. Akdag, C.T.J.A.O.R., *Behavior of closely spaced double-pile-supported jacket foundations for offshore wind energy converters.* 2016. 58: p. 164-177.
6. Shi, W., H.C. Park, C.W. Chung, H.K. Shin, S.H. Kim, S.S. Lee, C.W.J.I.J.o.P.E. Kim, and M.-G. Technology, *Soil-structure interaction on the response of jacket-type offshore wind turbine*. 2015. 2(2): p. 139-148.
7. Khodair, Y., A.J.I.J.o.C.S. Abdel-Mohti, and Materials, *Numerical analysis of pile–soil interaction under axial and lateral loads.* 2014. 8(3): p. 239-249.
8. Muthukkumaran, K., K.J.J.o.O.E. Arun, and M. Energy, *Erratum to: Effect of seabed slope on the pile behaviour of a fixed offshore platform under lateral forces.* 2015. 1(3): p. 223-236.
9. Popko, W., F. Vorpahl, A. Zuga, M. Kohlmeier, J. Jonkman, A. Robertson, T.J. Larsen, A. Yde, K. Sætertrø, and K.M. Okstad. *Offshore Code Comparison Collaboration Continuation (OC4), Phase 1-Results of Coupled Simulations of an Offshore Wind Turbine With Jacket Support Structure*. in *The Twenty-second International Offshore and Polar Engineering Conference*. 2012. International Society of Offshore and Polar Engineers.
10. Jonkman, J.M. and M.L. Buhl Jr, *FAST user's guide.* National Renewable Energy Laboratory, Golden, CO, Technical Report No. NREL/EL-500-38230, 2005.

11. Reese, L., S. Wang, W. Isenhower, J. Arrellaga, and J. Hendrix, *User's manual of LPILE plus 5.0 for windows.* Ensoft Inc., Austin, TX, 2004.
12. Vorpahl, F., W. Popko, and D. Kaufer, *Description of a basic model of the "UpWind reference jacket" for code comparison in the OC4 project under IEA Wind Annex XXX*. Fraunhofer Institute for Wind Energy and Energy System Technology (IWES), Germany, 2011.
13. Jonkman, J., S. Butterfield, W. Musial, and G. Scott, *Definition of a 5-MW reference wind turbine for offshore system development.* National Renewable Energy Laboratory, Golden, CO, Technical Report No. NREL/TP-500-38060, 2009.
14. Fischer, T., W. De Vries, and B. Schmidt, *UpWind Design Basis (WP4: Offshore foundations and support structures)*. 2010.
15. Passon, P., *Memorandum: derivation and description of the soil-pile-interaction models.* IEA-Annex XXIIII Subtask, 2006. 2.
16. RP2A-WSD, A. *Recommended practice for planning, designing and constructing fixed offshore platforms–working stress design–*. in *Twenty-*. 2000.
17. Jonkman, B. and J. Jonkman, *FAST v8. 16.00 a–bjj*. National Renewable Energy Laboratory, 2016.
18. Jonkman, J.M., *Dynamics modeling and loads analysis of an offshore floating wind turbine*. 2007, National Renewable Energy Lab.(NREL), Golden, CO (United States).
19. 61400-3, I., *Wind Turbines–Part 3: Design Requirements for Offshore Wind Turbines.* Tech. Rep., 2009.
20. Jonkman, J., G. Hayman, B. Jonkman, and R. Damiani, *AeroDyn v15 User's Guide and Theory Manual*. NREL Draft Report, 2015.
21. Jonkman, J., A. Robertson, and G. Hayman, *HydroDyn user's guide and theory manual*. National Renewable Energy Laboratory, 2014.
22. Turbines–Part, I.E.C.J.W., *IEC 61400-1*. 2005. 1.
23. Bargi, K., R. Dezvareh, S.A.J.E.E. Mousavi, and E. Vibration, *Contribution of tuned liquid column gas dampers to the performance of offshore wind turbines under wind, wave, and seismic excitations.* 2016. 15(3): p. 551-561.
24. Dezvareh, R., K. Bargi, S.A.J.S. Mousavi, and I. Engineering, *Control of wind/wave-induced vibrations of jacket-type offshore wind turbines through tuned liquid column gas dampers.* 2016. 12(3): p. 312-326.
25. Dezvareh, R.J.I.J.o.C. and O. Engineering, *Application of Soft Computing in the Design and Optimisation of Tuned Liquid Column–Gas Damper for Use in Offshore Wind Turbines.* 2019. 2(4): p. 47-57.
26. Jonkman, B.J., *TurbSim user's guide: Version 1.50.* 2009.
27. Randolph, M., S. Gourvenec, D. White, and M. Cassidy, *Offshore geotechnical engineering*. Vol. 2. 2011: Spon Press New York.
28. DNV, G., *Support structures for wind turbines.* Standard DNV GL-ST-0126, 2016.
29. Damiani, R., J. Jonkman, and G. Hayman, *SubDyn User's Guide and Theory Manual*. 2015, National Renewable Energy Lab.(NREL), Golden, CO (United States).
30. Guide, M.U.s., *The mathworks.* Inc., Natick, MA, 1998. 5: p. 333.
31. Bir Gunjit, S.J.N.R.E.L., Golden, CO, USA, *User's Guide to BModes*. 2007.
32. De Vries, W., N.K. Vemula, P. Passon, T. Fischer, D. Kaufer, D. Matha, B. Schmidt, and F. Vorpahl, *Final report WP 4.2: support structure concepts for deep water sites: deliverable D4. 2.8 (WP4: offshore foundations and support structures)*. 2011.

INTERNATIONAL JOURNAL OF
COASTAL & OFFSHORE ENGINEERING
IJCOE Vol.5/No. 4/Winter 2020 (35-46)

Available online at: www. Ijcoe.org

Experimental Performance Evaluation of a Hydraulic PTO System for Centipede Wave Energy Converter

Mozhgan Aghanezhad [1], Rouzbeh Shafaghat [2*], Rezvan Alamian[3]

[1] *MSc Student, Sea-Based Energy Research group, Babol Noshirvani University of Technology; mozhganaghanezhad@nit.ac.ir*
[2*] *Associated Professor, Sea-Based Energy Research group, Babol Noshirvani University of Technology; rshafaghat@nit.ac.ir*
[3] *Senior Research Associate, Sea-Based Energy Research group, Babol Noshirvani University of Technology; ralamian@nit.ac.ir*

ARTICLE INFO

Article History:
Received: 16 Jun. 2020
Accepted: 08 Sep. 2020

Keywords:
Marine Energy
Centipede Wave Energy Converter
Hydraulic PTO
Experimental Analysis
Optimization

ABSTRACT

In the past decade, ocean and marine waves like other renewable energy sources attracted attention due to its high energy density. The most important part of a wave energy converter (WEC) is power take-off (PTO) system. In this study, a proper hydraulic power take-off system for centipede WECs has been evaluated and analyzed in experimental scale. Experimental analysis has been done in dry conditions. Important parameters are resistant load of rheostats and the opening percent of the flow control valve. System input is the wave force, which is modeled as an external mechanical force applied to the end of the lever. Resistant load of rheostats is changeable in the range of 9.5 to 55 ohms. In addition, according to the range of valve opening, six positions are selected to study. Results in this research show that, as resistance load increases, output power and efficiency, are enhanced significantly. On the other hand, in all the resistive loads tested, there is a maximum point (2 rev. valve opening) for efficiency, which shows the positive effect of controlling the input flow to the Hydro Motor (HM). The efficiency in this position of the flow control valve opening has enhanced by 40% compared to neighbor situations.

1. Introduction

Nowadays, human lifestyle and living standards have been changed. Besides, increasing energy consumption in all aspects of life is a force to use more and more energy. Oil crisis, reducing fossil resources, and increasing global warming have led human thought to use renewable resources, re-produced every day. Among them, utilization of natural sources like sun, wind, water and ocean are on top. Likewise, international treaties as Paris Agreement and Kyoto Protocol are motivation and encourage for activists in this context [1-3]. It is worth noting that extracting marine energy as a major and promising source, with having more available energy potential (between 15 to 20 times more) than wind or solar energy, has inspired enormous interest [4].

A brief insight into geographical situation of Iran, indicates more than 20% of the population, business centers, recreation centers and residential areas are focused near 2700 km shoreline of Iran [5]. Therefore, strategic attention to different types of harnessing wave energy is very important for generating electrical power. In this regard, Caspian Sea as the largest lake in the world, despite being closed compared to other open waters, has a great potential of extracting energy due to its continuous waves [6].

Wave energy converter is one of the latest technology in the world, produce energy from ocean and seas. The requirement for such projects to be economical is the definition and implementation of coherent research projects in laboratory and semi-industrial dimensions, in order to evaluate the system and the parameters affecting it. Over the past decades, a wide variety of WECs have been developed and can be said: hundreds of prototypes have been registered to extract wave energy so far. In general WECs can be classified according to three characteristics: location (onshore, nearshore and offshore), size (point absorber, terminator and attenuator) and working principle (overtopping, pressure differential, impact and floating structure) [3].

In order to utilize the WECs, lots of researches has spurred. In 2007 Waters et al. have studied a full scale prototype of a point absorber WEC in the Swedish west

coast [7]. Tests have been done for different wave climate. It has been indicated that, for resistive loads, optimal load is existed. Many researches have been done to study different shapes of buoys. Sarlak et al. optimized the buoy configuration in heave and pitch mode [8]. Yousefi et al. in 2016 examined the Wavestar WEC under the Caspian Sea parameters. They studied parameters such as arm length, buoy dimension, wave period and wave height [6]. An experimental study has investigated on the Centipede WEC of attenuator type, with 6 spherical buoys by Alamian et al. in 2019 [4]. This study has been done in the wave tank of the Babol Noshirvani University of Technology and main parameters were amplitude and period of different sea waves.

One of the most important parts of any wave energy converter is the power take-off system. In this regard, the fundamental issue in the operation of WECs is controlling PTO to achieve optimum energy from waves. This has massive impact on maximizing the WEC utilization; especially on large scale wave power plants. Henderson in 2006 applied active control for PTO to maximize power capture across a range of sea-states and improve survivability [9]. Drew et al. in 2009 introduced the state of WEC technology at the time, established different device types, classified PTO systems and considered some of the control strategies to enhance the efficiency of point absorber-type WECs [10]. In 2014, Hansen et al. developed a new PTO based on discrete hydraulics (using multi-chambered cylinders) named as Discrete Displacement Cylinder (DDC); to improve the power production of the 1 MW wave energy converter, Wavestar [11]. Nguyen et al. in 2016 showed the high potential of improvement brought by Model Predicting Control (MPC) in terms of harvested power [12].

In spite of substantial impact of applying control system to PTO on power quality and quantity (Lopes et al. in 2009 [13] and Kramer et al. in 2011 [14]), the adjustments of PTO system components is also very important. Accordingly, optimized power extraction can be achieved by defining proper resistant load, input fluid flow limitation to HM and specific input condition in hydraulic PTO system. In this research, performance of WEC is evaluated; considering flow control valve opening and resistant load (in electrical circuit) as important parameters. For quantitative analysis, output power (watts) and more importantly, total efficiency of the system are analyzed. Other parameters like HM pressure difference, rotational velocity of coupled HM and generator shaft, voltage and current are recording by camera (Nikon, L830).

According to the defined goals, in order to describe the problem first, the desired power take-off system is introduced; then in research method section, laboratory equipment, test method, and how to process the output data are considered. In the following, system efficiency is analyzed and results are presented. In the conclusion section, the most important results are explained.

2. Problem Definition

2.1. Power take-off system

The desired hydraulic power take-off system is designed for Centipede WEC (namely IRWEC2). The first step in developing process was done successfully in the form of experimental investigation at Sea-Based Energy Research Group of Babol Noshirvani University of Technology (Figure 1) [4]. In this laboratory model, mechanical power take-off system was used. Two configurations including 6 and 10 buoys were tested in several wave amplitudes and wave periods, and output power were surveyed [4].

(a)

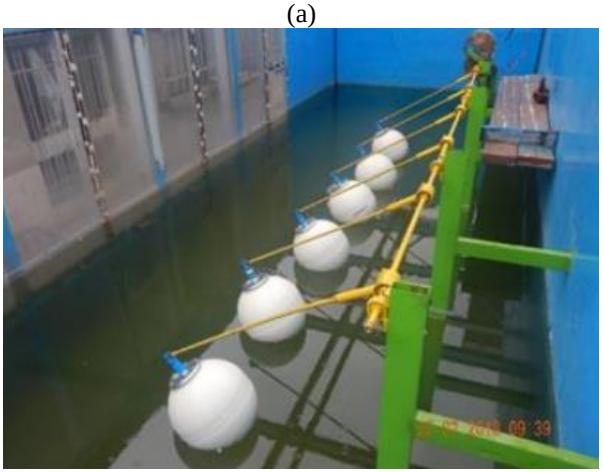

(b)

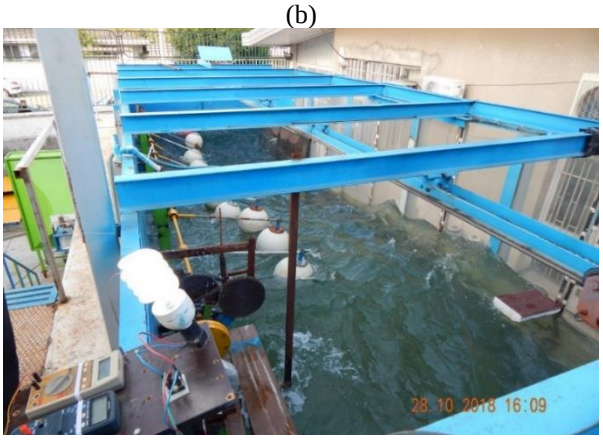

Figure 1. Centipede WEC that was built and tested in Sea-Based Energy Research Group of Babol Noshirvani University of Technology with mechanical PTO system; (a): 6 arms centipede WEC, (b): 10 arms centipede WEC

In the second step of developing process in larger scale, for extracting more power, a hydraulic power take-off system is chosen due to its well adapted characteristics to sea waves (large forces at low frequencies). Schematic plan of hydraulic PTO system in IRWEC2 is shown in Figure 2 In this study, before launching the WEC to wave tank, dry tests are implemented on hydraulic PTO outside the wave tank. The ultimate goal is parametric evaluation and achievement of appropriate operation points for PTO system.

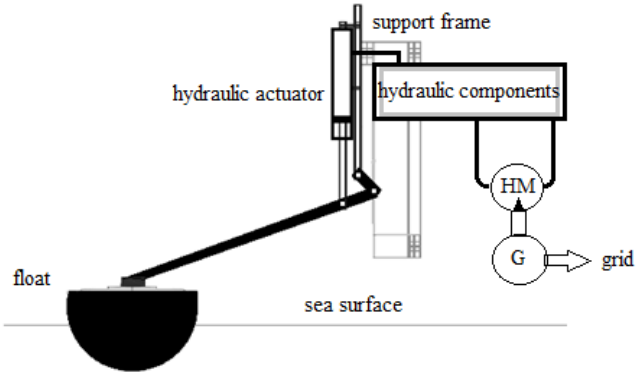

Figure 2. General schematic of Centipede WEC with hydraulic PTO system

2.2. Caspian Sea Waves

Before installing PTO system on WEC, ensuring of optimal system performance according to wave characteristics of the target sea is very important. As the WEC is developed to operate in the Caspian Sea, experimental wave modeling in laboratory is based on its wave condition. Figure 3 illustrates time-averaged wave energy per unit length of the wave front for mean wave period and significant wave height of the Caspian Sea near the Babolsar. The color scale represents total annual energy per unit length of wave front, the bold numbers indicate the occurrence of sea states in number of hours per year.

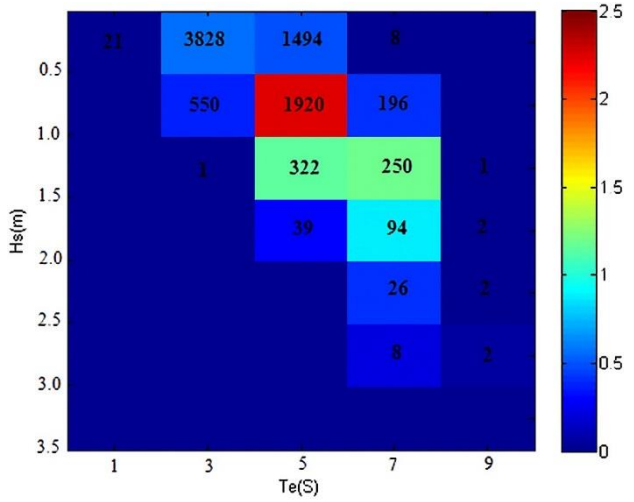

Figure 3. Combined scatter and energy diagrams of the annual energy corresponding to sea states in different ranges of Hs and Te for Caspian Sea (near Babolsar) [15]

As can be seen in this figure, significant wave height (Hs) within the ranges of 0.5 to 1 m and mean wave period (Te) between 4 and 6 s, satisfies both maximum energy and occurrences. Therefore, the significant wave height of 70 cm is selected for evaluating the WEC. Regarding to wave period; as period decreases, force applied to WEC increases and critical condition may occur. Therefore 2 seconds wave period can be considered.

3. Research Method

3.1. Laboratory Equipment

As shown in Figure 2, hemisphere buoy is connected to the support frame and hydraulic actuator by an arm. To investigate dry tests, in the absence of buoy, equivalent force is applied to the lever (110 cm arm in Figure 4-a). Transmission mechanism is 4-bar linkage (Figure 4-b, c). Sinusoidal input wave moves the buoy in heave direction and activates the hydraulic actuator. Hydraulic cylinder has a stroke of 245 (mm), but according to test requirements, 12 (cm) displacement is sufficient. Hydraulic actuator along with other existing components provide a certain pressure difference for HM. Output rotational motion of the HM, by coupling to the generator produces electricity. Figure 5 depicts P&ID diagram for hydraulic PTO system and related equipment.

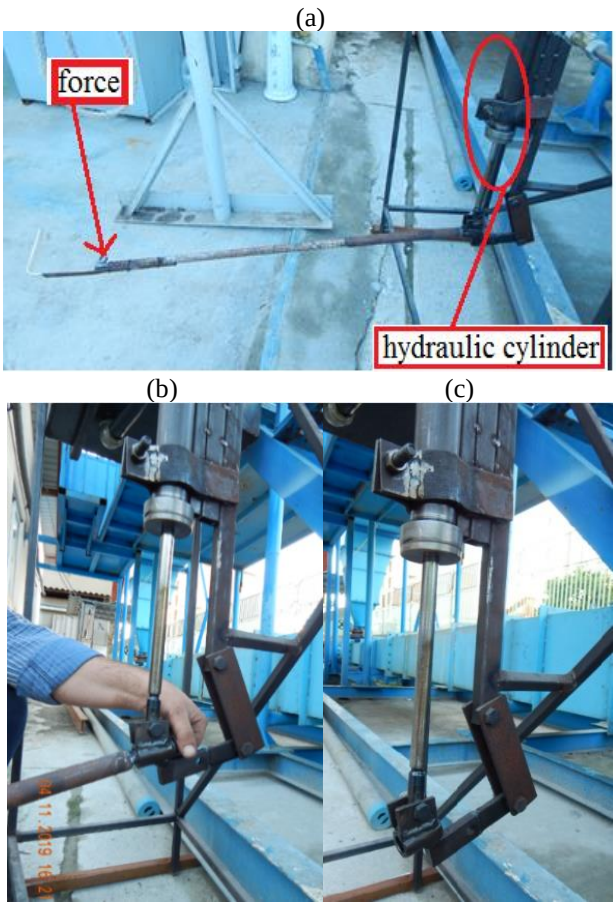

Figure 4. Lever and piston motion mechanisms of WEC

Final set-up for testing hydraulic PTO is illustrated in Figure 6. It's noteworthy that a 50 liters capacity oil tank is used for keeping, purify and cooling the circulating oil. Circulating oil is a hydraulic oil named HLP 51524 part 2. Used hydraulic actuator is a single-acting hydraulic cylinder and 2 check valves are used on both sides of the cylinder to prevent back flow.

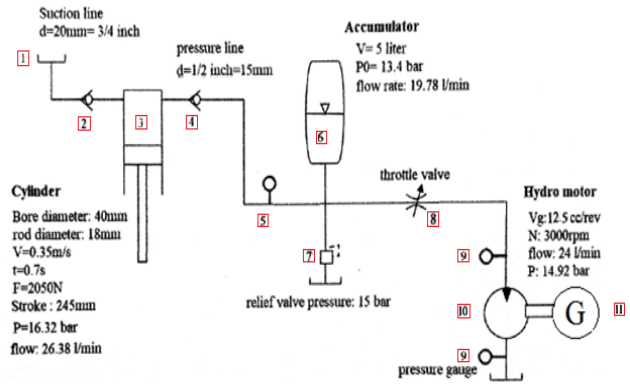

Figure 5. Schematic of hydraulic circuit and components

Figure 6. Test setup for centipede WEC

An accumulator is used to prevent oscillations and regulate system pressure. By locating a flow control valve before HM, input flow rate (velocity) is controlled. A relief valve is installed after the accumulator and before the flow control valve to prevent undesirable increase in pressure and to protect the pressure-sensitive parts and equipment. The pressure is relieved by allowing the pressurized fluid to flow from an auxiliary passage out of the system, when necessary. To measure the pressure, there are 3 pressure gauges in hydraulic circuit; one in charge line and two of them are on both input and output flow of the HM. HM is a gerotor (inner gear motor) type motor with 12.5 cc displacement. A brief technical information on mentioned equipment are pointed out in Table 1.

Table 1. Technical information of setup components.

	name	Technical information	accuracy
1	Oil tank	Tank capacity: 50 liter	-
2	Check valve	A one-way spring-ball valve (3/4 in), between oil tank and cylinder	-
3	Hydraulic cylinder	Single-acting cylinder, 18 mm rod diameter, 245 mm displacement	-
4	Check valve	A one-way spring-ball valve (1/2 in), between cylinder and accumulator	-
5	Pressure gauge	Liquid filled 40 bar gauge	±0.5%
6	Accumulator	5 liter capacity	-
7	Relief valve	Pressure relief valve se at 15 bar	-
8	Control valve	Needle valve	-
9	Pressure gauge	Liquid filled 25 bar gauge	±0.5%
10	Hydro motor	12.5 cc gerotor	-
11	Generator	Axial-Flux Permanent Magnets Generator (AFPMG) TGET260-I-0.1KW	-
12	Hydraulic oil	HLP 51524 part 2	-
13	Multi meter	HIOKI 3256-DIGITAL Hi TESTER	±0.6%
14	Multi meter	HIOKI 3200- DIGITAL Hi TESTER	±1.5%
15	Force gauge	Radex force gauge	±0.05%
16	Tachometer	Lutron tachometer DT-2268 (contact-laser)	±0.05%

As mentioned before, in the absence of buoy, for modeling its motion, applying a sinusoidal mechanical force (excitation force for cylinder) to the end of arm can move the hydraulic cylinder. According to Figure 7, the force is applied to the end of lever (arm) by rope and pulley system. In addition, this force is measured by a digital force gauge.

The generator coupled to HM is an Axial-Flux Permanent Magnets Generator (Figure 8). As figure shows, a rheostat is used to apply resistant load. Also, the electric current passing through the rheostat and its voltage are measured by two multimeters. Output data from the measurement equipment (tachometer, pressure gauges, rheostat and multimeters) is recorded by a camera for subsequent analysis. It should be noted that the output current of generator is three-phase at first; the three-phase output is rectified by a bridge rectifier (Figure 9).

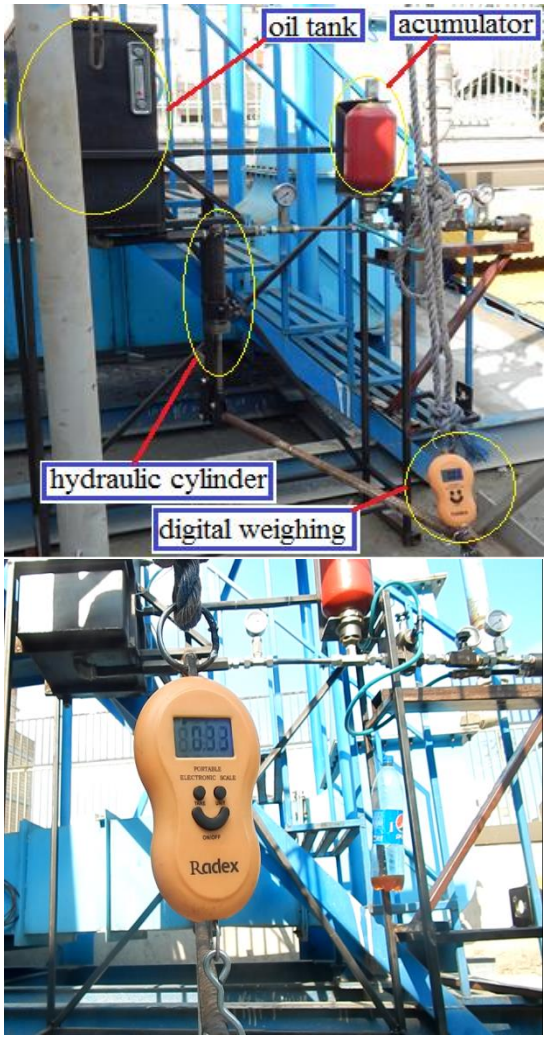

Figure 7. Mechanical force measurement in hydraulic PTO system

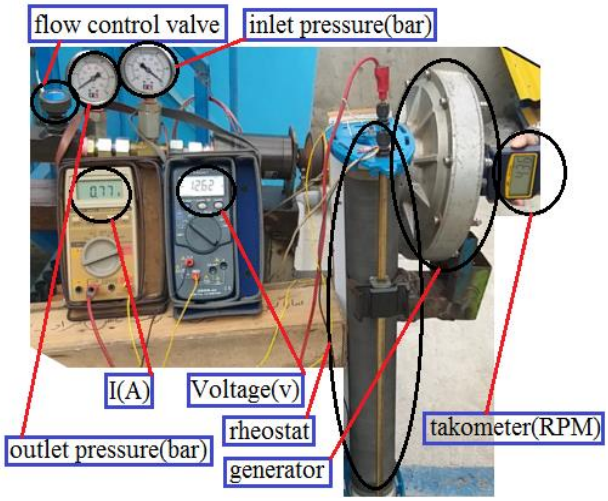

Figure 8. Set-up of measuring instruments

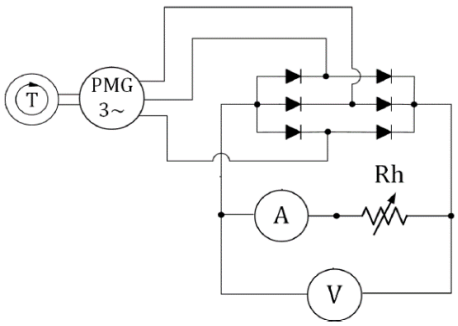

Figure 9. Electric circuit including Diode Bridge (bridge rectifier), rheostat and voltage and current measurement elements

3.2. Test procedure

As mentioned earlier, in order to perform experimental tests, it is important to pay attention to two parameters, the amount of opening of the flow control valve and the amount of load applied by the rheostat. Flow control valve has a manual regulator that is opened in the range of [0.5 to 3] revolution with the step of 0.5 rev. (Figure 10). For exact adjustment of the control valve opening in the defined modes, the control valve body and also the valve is marked at fully closed stage (Figure 10-a). In Figures 10-b and 10-c, valve opening process is depicted clearly.

(a)

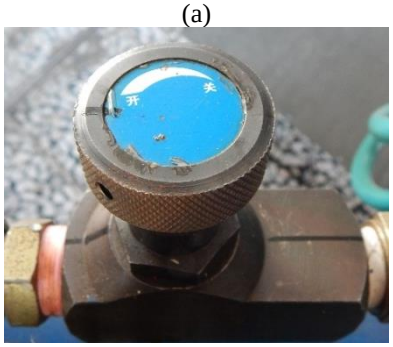

(b)

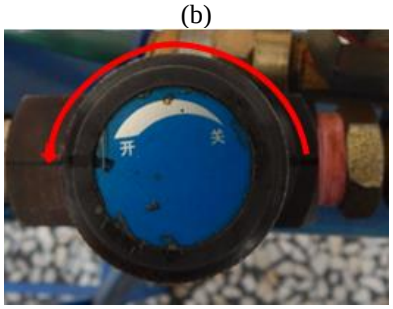

(c)

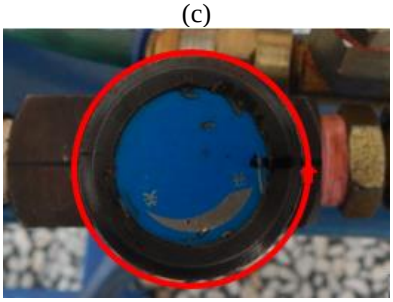

Figure 10. Flow control valve and related settings for opening positions

Continuity in HM output shaft is of high importance; thus in fully closed fluid path (closed control valve) by applying mechanical force to lever, both accumulator charging and pressure difference can be provided (for HM). After the accumulator has been charged, hydraulic fluid flows through the HM. In this status; by applying continues mechanical force to lever, continues rotation of HM and then generator is enabled. As it is clear in Figure 6, three pressure gauges are installed in hydraulic path. The first one is before accumulator that measures its pressure. The second and the third one are before and after he HM, respectively. At first, input path for hydraulic oil is closed, then mechanical force increases the line pressure. At this time, the application of mechanical force continues until the line pressure (first gauge) reaches 30 bar and accumulator is charged. Hence, the fear of pressure drop during testing or data collection reduces. If the pressure is reduced, the mechanical force will be compensated by continuing to apply force to the lever. At this stage, after opening the control valve, pressure increases suddenly in second gauge. Then by rotating common shaft of HM and generator, power production initiates. Discharging hydraulic oil passing the third gauge, returns to oil tank. The third gauge shows the pressure of discharging hydraulic fluid that almost all the time is zero; means the HM converts all the fluid pressure to work. Contemplative point is fluid pressure loss in the hydraulic circuit. Experiments have shown that maximum pressure difference value between first and second gauges is about 1 bar; but significant pressure difference is before and after the HM. As a result, the most dissipation (power transmission) is observed at this zone.

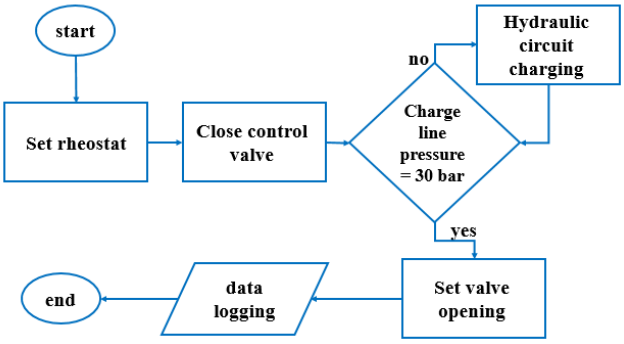

Figure 11. Test flowchart

In each mode of control valve, load of rheostat changes in the range [0 -55] ohms; exactly are set on values of 9.5, 22, 34, 39, 44.5, 50, and 54.8 ohms. Output data in this stage are voltage and current, measured by a pair of multi meters. In addition, for detailed study, force gauge measures the applied force, when lever goes up to the end of its course (in half of the modeled wave period). Therefore, the lever returns to its initial position under the influence of weight and the mechanical force is zero. Procedure of the test is shown in form of a flowchart in Figure 11.

4. Output data processing

4.1. Mechanical force

One of the measured parameters is mechanical force. Due to the lever motion type, quadratic polynomial interpolation is used for the obtained data (Figure 12). Measured force in different modes of control valve is provided in Figure 13. A common point in all situation is measured force convergence to constant value. This constant value of mechanical force is used for calculation. Also, due to the slight difference in the data of the interpolation polynomial and the measured data, the values of the interpolation polynomial are used in the calculations.

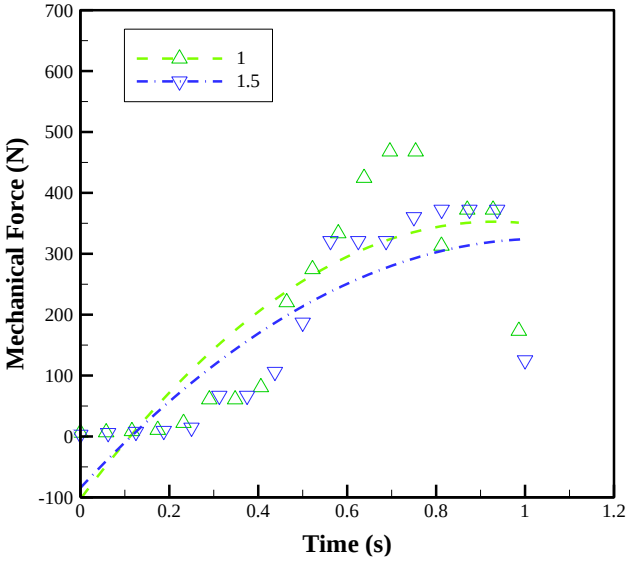

Figure 12. Applied mechanical force diagrams in 1 and 1.5 rev positions and related quadratic curve fitting

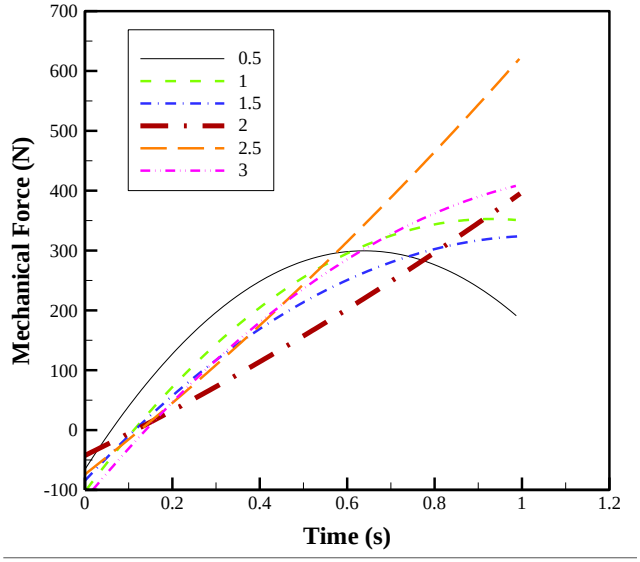

Figure 13. Applied mechanical force curves in all valve positions

By measuring the applied mechanical force to lever, input mechanical power to the system in all valve situations is calculated. Mechanical force period is almost fixed and is near 2 seconds and its stroke is 70 cm. Lever velocity and input mechanical power are defined as below:

$$P_{in}(w) = F_{avg}.v \quad (1)$$

$$v(\frac{m}{s}) = \frac{\Delta x}{t} = \frac{0.7}{1} = 0.7(\frac{m}{s}) \quad (2)$$

Where P_{in} is input power (W), F_{avg} is the mean force applied to the lever (N), v is lever velocity $(^{m}/_{s})$, Δx is lever stroke (m) and t is time (s).

4.2. Hydraulic (hydro) power

As mentioned, with flowing of hydraulic oil through various elements of the hydraulic circuit, pressure drop and dissipation occur; however, with the passage of hydraulic oil through the HM, there is a huge difference in pressure, of which only part of the potential generated is used to generate power, and the rest is wasted in the form of dissipation. So the produced power can be obtained by Eq.(3) [16]:

$$P_{HM}(w) = Q * \Delta p * \frac{\eta_t}{600} * 1000 \quad (3)$$

Q is HM flow rate $(^{l}/_{min})$, Δp is HM pressure difference (bar), and η_t is HM efficiency. Pressure difference is recorded during the test and HM flow rate can be achieved by rotational velocity of the HM shaft, as follows.

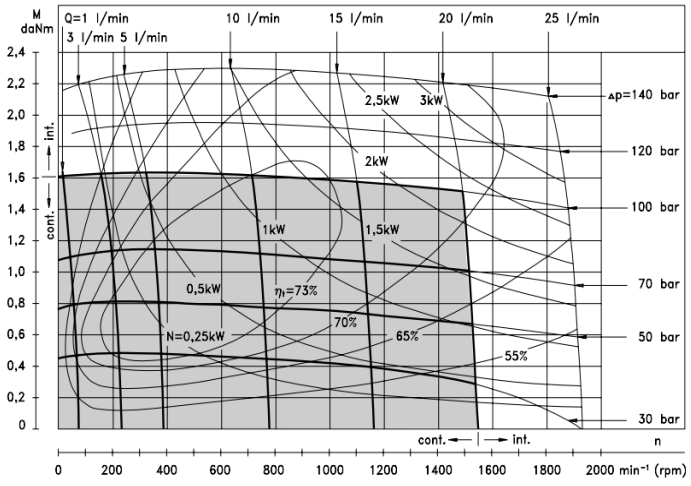

Figure 14. Hydro motor performance diagram [17]

$$Q\left(^{l}/_{min}\right) = \frac{\omega(RPM) * V_g(cm^3)}{1000} \quad (4)$$

V_g is HM displacement (fixed value) and ω is rotational velocity of the HM shaft. By using flow rate and pressure difference, the efficiency of the hydro motor can be read on its performance diagram (Figure 14).

4.3. Electrical power

By measuring electric voltage and current, generator power as output of the system can be written as Eq.(5):

$$P_G(w) = V.I \quad (5)$$

I is current intensity (A) an V is electric voltage (V). To display the trend of electrical power variations per control valve position change, curve fitting is used. A pair of sample for 34 and 50 ohms resistance are presented in Figure 15.

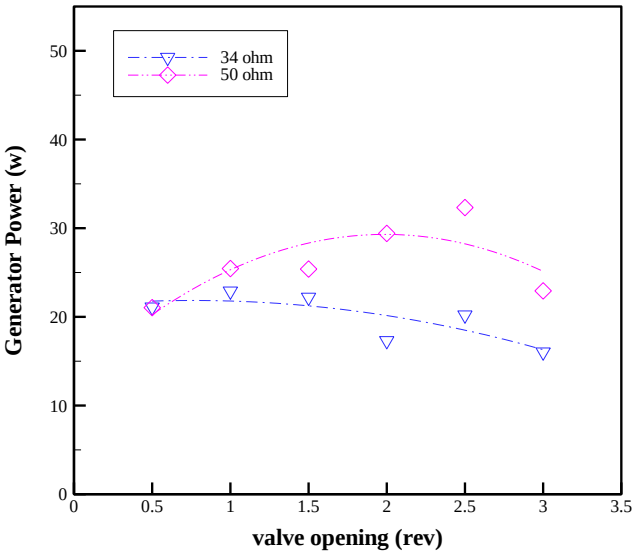

Figure 15. Curve fitting on calculated electrical power

4.4. Wasted power

Wasted power is actually the power that generator cannot convert it to output electricity. For better comparison, the parameter GDP is defined as dissipated power percentage (Generator Damping Percentage) (Eq.(6)).

$$GDP = (1 - \frac{P_G}{P_{HM}}) * 100 \quad (6)$$

In the previous equation, P_G is generator output power and P_{HM} is HM output power. Figure 16 illustrates dissipated power percentage for generator. In this figure, experimental data are fitted by quadratic polynomial curve. Comparing damping percentage in these two cases shows that high resistances wastes less power.

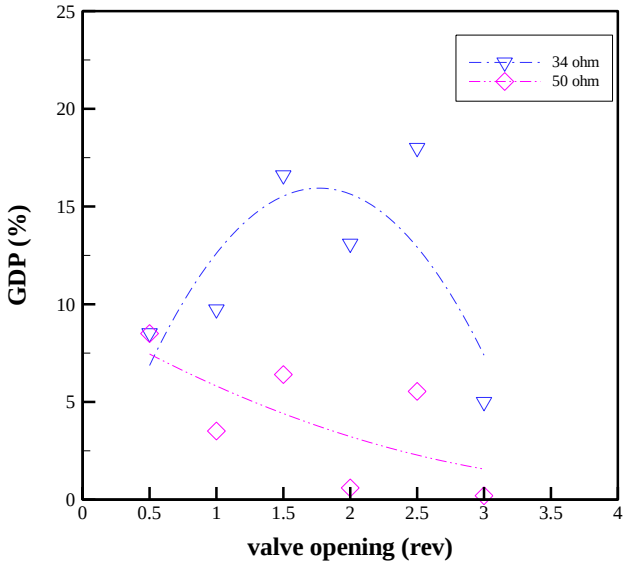

Figure 16. Dissipated power percentage for Generator

4.5. System efficiency

According to mechanical and electrical power (input and output power, respectively), whole WEC system efficiency (including PTO and the absorber efficiency) can be calculated as Eq.(7):

$$\eta_{WEC} = \frac{P_G}{P_{in}} * 100 \qquad (7)$$

P_{in} is input mechanical power. It is worth noting that for displaying the WEC efficiency trend, curve fitting is used. A sample of result for 34 and 50 ohms resistance can be seen in Figure 17.

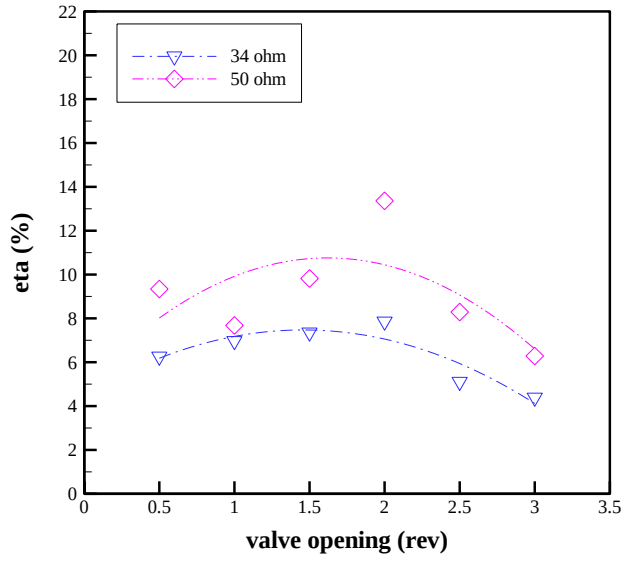

Figure 17. WEC system efficiency and related quadratic curve fitting for 2 different load values

5. Results and Discussion

Due to calculation procedure, the results are provided herein, in order to determine the best valve opening position and also the most suitable value of resistance. In this regard, to calculate the total efficiency of PTO, first, input and then, output values (mechanical and electrical powers, respectively) are calculated. Furthermore, for more detailed description, related diagrams to obtained results will be provided.

Figure 18 represents the results of input mechanical power in all control valve positions. As can be seen, applied mechanical force to the lever is not equal in all test conditions; but it should be reminded that the force period and course are always constant which are equal to 2 seconds and 70 cm, respectively. As a result, the stable input power has different values.

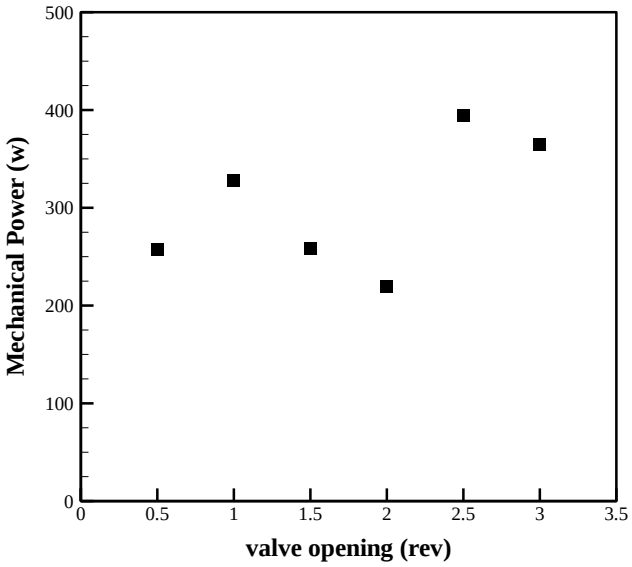

Figure 18. Input mechanical power per valve opening positions

Figure 19 displays generator electrical power in different control valve positions and loads. Considering this figure, output power almost enhances by increasing the resistance of rheostat. Nevertheless, in 22, 50, and 54.8 ohms, the extremums can be seen.

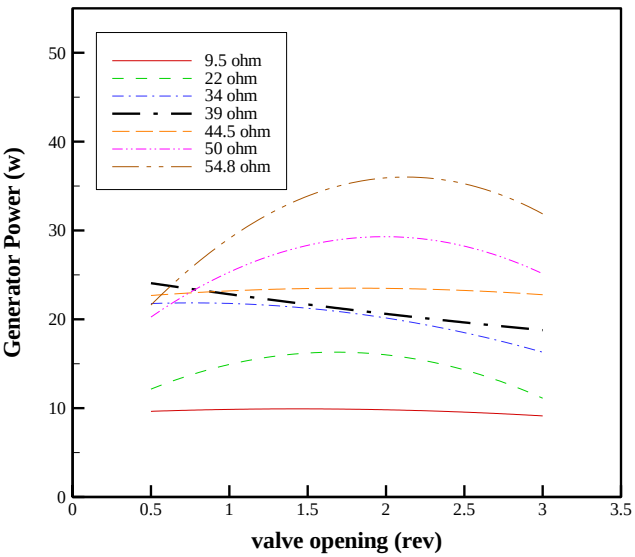

Figure 19. Output power of generator for all valve opening positions in various resistant loads

By determining input and output power to the system, WEC efficiency is presented in the form of Figure 20. Efficiency of WEC system in six control valve positions and seven different resistant load values are drawn using interpolation curves. As can be seen, by increasing the resistance, efficiency increases, too. The maximum system efficiency happens in high resistances and in 2 rev. valve opening. This trend applies to3 different values of rheostat. In fact, the diagram shows that, a maximum point exists between the two positions 1.5 and 2 rev; but, this maximum in low resistance happens between 1 and 1.5 rev. After position 2.5 rev. and in 3 rev, a severe drop can be seen. This result is true for all 7 resistance, so the existence of an extremum point has occurred according to the initial assumption.

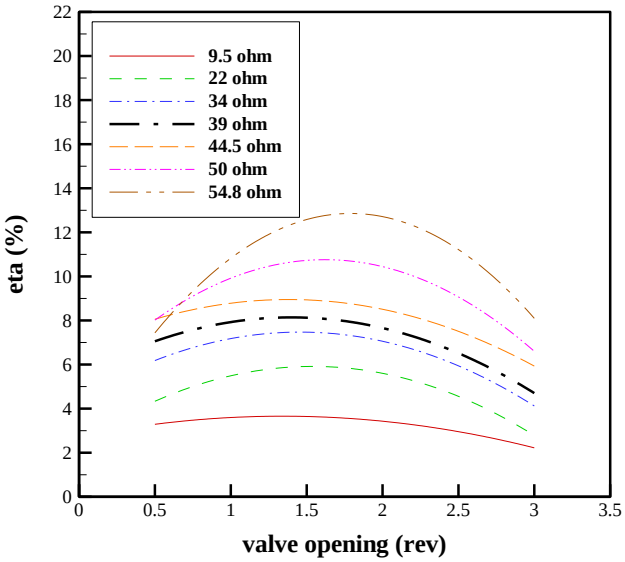

Figure 20. System efficiency curve fitting per all valve opening positions in 7 resistant loads

Figure 20 clearly shows the importance of control valve and rheostat setting. In the position 2 rev, variation of rheostat value from 9.5 to 54.8 ohms, increases the efficiency up to 250%. Also, changes in this parameter in other situations can lead to 170% increment (at least) in the efficiency. In all 7 different resistances, efficiency in 2 rev. valve opening position shows an enhancement of at least 6% and at most 36% compared to its previous position (1.5 rev. valve opening). Also, efficiency of this position, in comparison to the next position (2.5 rev. valve opening) increases at least 28% and at most 73%. Average efficiency enhancement is about 40% over all tests by changing the valve position. It is clear that the changes in the efficiency of this particular position compared to the 0.5 and 3 rev. positions are more than above values.

Figure 21 shows the effect of resistance changes on efficiency better. As noted before, system efficiency increases by increasing the resistant load. The important point in this diagram is that the diagrams of the positions of 0.5, 1, 1.5 and 3 openings are approaching their maximum. Due to this observation, it can be predicted that an extremum point exists for each specific situation of the PTO system. But this statement cannot be seen for 1.5 and 2 rev. positions; means that extremum point for these positions occur in higher loads while other situations are very close to extreme point and after reaching the maximum, efficiency decreases. High efficiency value of position 2 rev. among all valve positions can be observed clearly.

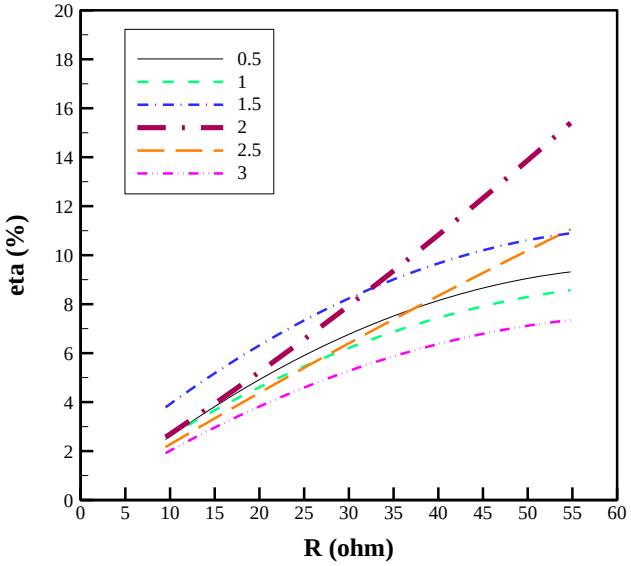

Figure 21. System efficiency per load changes

Pursuant to Figure 21, in the maximum resistance value, efficiency is declined in positions of 0.5 and 1 rev. and then is rised in 2 rev. situation; again from position of 2 rev. to the position of 3 rev, reduction trend can be seen. Actually, the figure shows the contrast between 1.5 and 2 rev. positions. Before 35 ohms resistances, 1.5 rev. valve opening provides more efficiency; and then after 35ohms, the most efficiency belongs to 2 rev. valve opening. As well, Figure 20 confirms this result.

As it is clear in Figure 22, at low resistant loads, generator power dissipation is so high; reaches 45% in 9.5 ohms resistance. Also, it can be seen that the dissipation enhances by increasing the resistance; until it reaches below 5% in 54.8 ohms. Due to previous results, maximum power production and efficiency and of course the least power dissipation are occurred in 54.8 ohm resistance.

According to the presented results, the position of 2 rev. valve opening with a resistance of 54.8 ohms gives the best response to the defined inputs. For better analysis, the output voltage and current diagrams as well as the output power are presented for this optimal position (Figures 23 and 24); In this case, the maximum power generated is 31 watts.

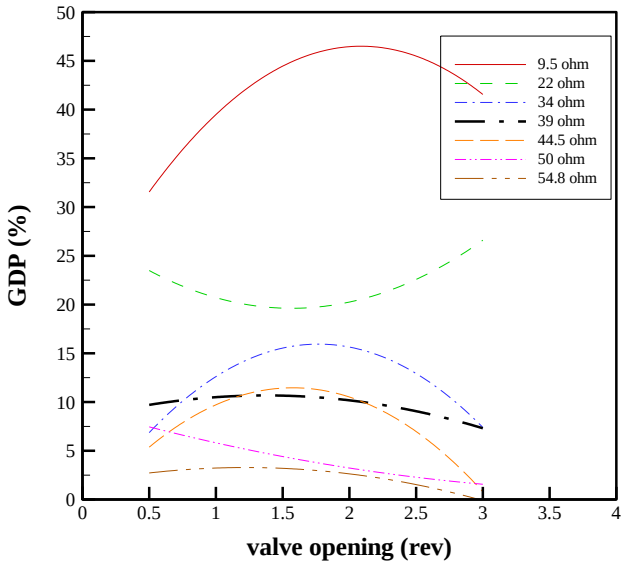

Figure 22. Dissipated power percentage per valve opening situations in 7 resistant loads

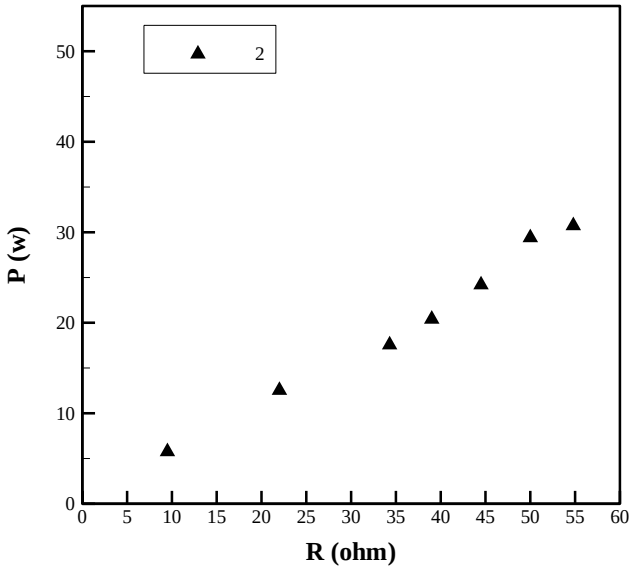

Figure 24. Output power for 2 rev position during test

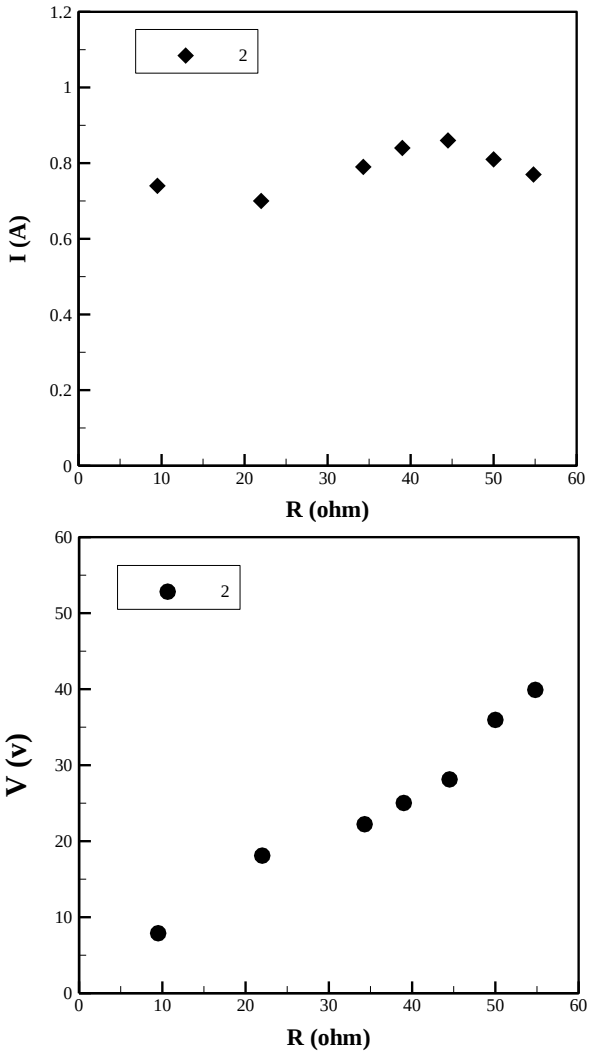

Figure 23. Voltage and current diagrams for 2 rev position during test

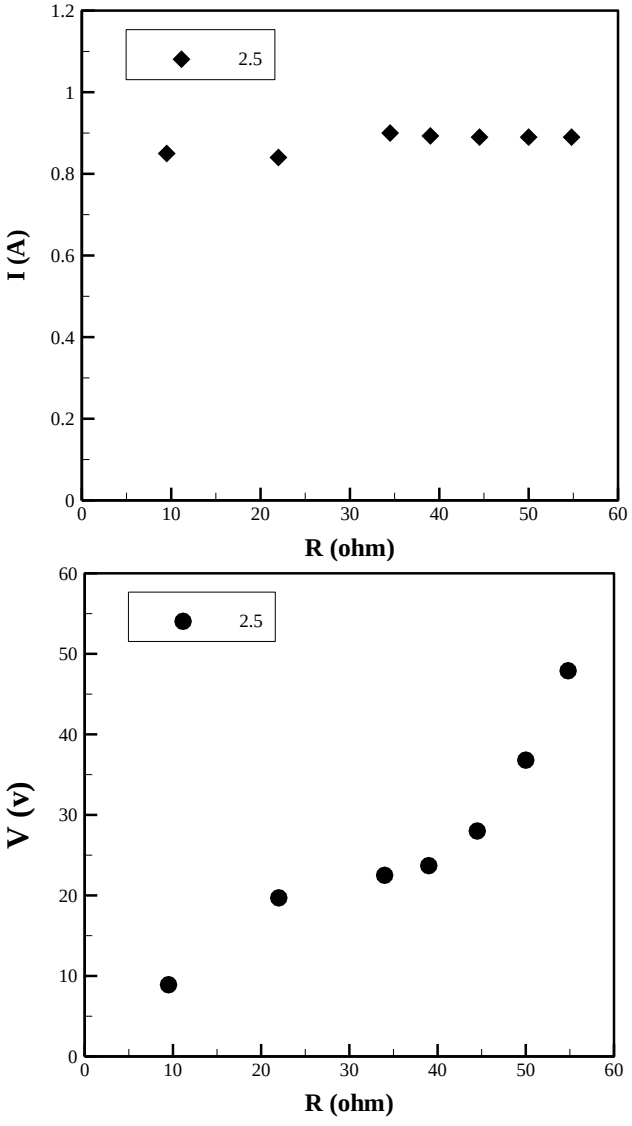

Figure 25. Voltage and current diagrams for 2.5 rev position during test

Figures 25 and 26 show generator output voltage, current, and power in 2.5 rev. valve opening. It is clear that output power rises to more than 42 watts. Produced power in this position is more than others; but about efficiency, 2 rev. valve opening case is higher.

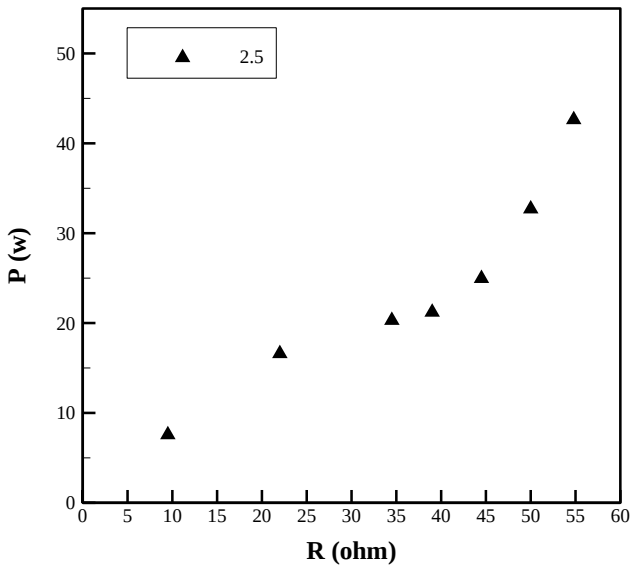

Figure 26. Output power for 2.5 rev position during test

In order to adapt test result to practical situation, it is needed to test the WEC in the wave tank. In this regard, some changes are necessary i.e. a proper buoy and an elongated arm, with an appropriate mechanism transferring wave energy to hydraulic cylinder more efficient. Then Froude similarity is used as follows:

$$\frac{H_2}{H_1} = \alpha_L \tag{8}$$

$$\frac{T_2}{T_1} = {\alpha_L}^2 \tag{9}$$

Here H and T represent wave height and wave period respectively and α_L is a dimension ratio between prototype and actual model.

6. Conclusions

In this investigation, performance of a hydraulic power take-off system in an attenuator wave energy converter named centipede WEC is analyzed experimentally. Dry case experiment condition is provided for the test unit to carry out the defined tests out of the wave tank. For modeling the effect of input wave on hydraulic actuator, an external mechanical force is used. Hydraulic PTO system response to input power is analyzed and evaluated. In this regard, resistance value of rheostat and control valve opening positions as main variables, are described to control WEC system efficiency. The output of the PTO system is evaluated as electrical power proportional to the defined load; also, measured generator voltage and current are analyzed. Significant result are as follows:

- Resistant load variations affect the output power and efficiency dramatically. For instance, according to certain inputs, efficiency improve from 4.2% in 9.5 ohms resistance to 14.7% in 54.8 ohms resistance.
- WEC system efficiency for particular positions like 0.5, 1, 1.5 and 3 rev. valve opening approaches to the maximum of the diagram; means in such conditions, the diagram reach to its peak for a specific resistance. In this condition, increasing resistance to higher values is not beneficial and causes losses and increases costs.
- In all seven resistances, changing control valve opening has a positive effect. In a certain position, maximum value can be achieved; the maximum point for 9.5 to 35 ohms resistances is occurred on 1.5 rev. valve opening and for resistances above 35 ohms is occurred on 2 rev. control valve opening.
- Maximum generator output power can be achieved in 2.5 rev. control valve opening; however, in 2 rev. position, the maximum efficiency is occurred. In implementation plans, this survey can be helpful for reducing costs.

Acknowledgment

The results presented in this article are the outcome of a research project approved by the Supreme Council for Science, Research and Technology (SCSRT). We would like to express our gratitude for the spiritual and funding support of the Mazandaran Provincial Government, the Deputy Governor for Economic Affairs and Resource Development.

List of Symbols

F_{avg}	Average force applied to the lever $[N]$
GDP	Generator Damping Percentage [%]
H_1	Prototype wave height $[m]$
H_2	Real model wave height $[m]$
I	Current $[A]$
P_G	Generator output power $[w]$
P_{HM}	Hydro Motor output power $[w]$
P_{in}	Mechanical inlet power $[w]$
Q	HM flow rate $[{}^{l}/_{min}]$
t	Time $[s]$
T_1	Prototype wave period $[s]$
T_2	Real model wave period $[s]$
v	Averaged velocity of lever $[{}^{m}/_{s}]$

V	Voltage $[V]$
V_g	Hydro motor displacement $[cm^3]$
Δp	Pressure difference $[bar]$
Δx	Stroke $[m]$
ω	HM rotational velocity $[RPM]$
η_{WEC}	Total system efficiency [%]
η_t	HM efficiency [%]
α_L	dimension ratio

9. References

[1] J. Falnes, "A review of wave-energy extraction," *Marine structures*, vol. 20, no. 4, pp. 185-201, 2007.

[2] I. López, J. Andreu, S. Ceballos, I. M. de Alegría, and I. Kortabarria, "Review of wave energy technologies and the necessary power-equipment," *Renewable and sustainable energy reviews*, vol. 27, pp. 413-434, 2013.

[3] M. Den Elzen, A. Admiraal, M. Roelfsema, H. van Soest, A. Hof, and N. Forsell, "Contribution of the G20 economies to the global impact of the Paris agreement climate proposals," *Climatic Change*, vol. 137, no. 3-4, pp. 655-665, 2016.

[4] R. Alamian, R. Shafaghat, and M. Ghasemi, "Experimental evaluation of attenuator WEC in a laboratory wave tank," (in eng), *Journal Of Marine Engineering*, Research Paper vol. 14, no. 28, pp. 1-9, 2019.

[5] M. Negahdari, H. Dalayeli, and M. Moghadas, "modelling and analyzing piont absorber WEC for a cylinderical buoy in heave motion," (in persian), 1394.

[6] P. Yoosefi Khiabani, M. A. Abbaszadeh, A. Khorshid, and M. M. Ettefagh, "Investigation of WaveStar Energy Converter Performance in Caspian Sea Using Regular Wave and Froude-Krylov Force," (in persian), *Journal Of Marine Engineering*, Research Paper vol. 12, no. 23, pp. 45-55, 2016.

[7] R. Waters *et al.*, "Experimental results from sea trials of an offshore wave energy system," *Applied Physics Letters*, vol. 90, no. 3, p. 034105, 2007.

[8] H. Sarlak, M. S. Seif, and M. Abbaspour, "Experimental investigation of offshore wave buoy performance," *Journal of Marine Engineering*, vol. 6, no. 11, pp. 0-0, 2010.

[9] R. Henderson, "Design, simulation, and testing of a novel hydraulic power take-off system for the Pelamis wave energy converter," *Renewable energy*, vol. 31, no. 2, pp. 271-283, 2006.

[10] B. Drew, A. Plummer, and N. Sahinkaya, "A review of wave energy converter technology," vol. 223, ed: Sage Publications Sage UK: London, England, 2009, pp. 887-902.

[11] R. Hansen, T. Andersen, H. Pedersen, and A. Hansen, "Control of a 420 kn discrete displacement cylinder drive for the wavestar wave energy converter," in *ASME/BATH 2014 Symposium on Fluid Power and Motion Control*, 2014: American Society of Mechanical Engineers Digital Collection.

[12] H.-N. Nguyen, G. Sabiron, P. Tona, M. M. Kramer, and E. Vidal Sanchez, "Experimental validation of a nonlinear MPC strategy for a wave energy converter prototype," in *ASME 2016 35th International Conference on Ocean, Offshore and Arctic Engineering*, 2016: American Society of Mechanical Engineers Digital Collection.

[13] M. Lopes, J. Hals, R. Gomes, T. Moan, L. Gato, and A. d. O. Falcão, "Experimental and numerical investigation of non-predictive phase-control strategies for a point-absorbing wave energy converter," *Ocean Engineering*, vol. 36, no. 5, pp. 386-402, 2009.

[14] M. Kramer, L. Marquis, and P. Frigaard, "Performance evaluation of the wavestar prototype," in *Proceedings of the 9th European Wave and Tidal Energy Conference, Southampton, UK*, 2011, pp. 5-9: Citeseer.

[15] R. Alamian, R. Shafaghat, R. Bayani, and A. H. Amouei, "An experimental evaluation of the effects of sea depth, wave energy converter's draft and position of centre of gravity on the performance of a point absorber wave energy converter," *Journal of Marine Engineering & Technology*, vol. 16, no. 2, pp. 70-83, 2017.

[16] "Hydraulic Motors, Variable Displacement," in *HY30-8223/UK*, P. Hannifin, Ed., ed. sweden, 2014.

[17] "HYDRAULIC MOTORS MM," ed.

INTERNATIONAL JOURNAL OF
COASTAL & OFFSHORE ENGINEERING
IJCOE Vol.5/No. 4/Winter 2020 (47-53)

Available online at: www. Ijcoe.org

Fishing Port Pollution due to the Vessel Activities along Bandar Abbas Coast, Iran

Zabihollah Khakpoor [1], Mehrnaz Farzingohar[*1], Mohammad Ahmadizadeh Shaghooei[2], Alireza Soory[3]

[1,1]Department of Non Living Marine and Atmospheric Science, Faculty of Marine Science and Technology, University of Hormozgan, Bandar Abbas 3995, Iran*

[2]Head of Shahid Haghani passenger port, Bandar Abbas, Ayatollah Taleghani Boulevard, Shahid Haqqani Passenger Port

[3]Department Marine Environment, Faculty of Marine Science and Technology, University of Hormozgan, Bandar Abbas 3995, Iran

ARTICLE INFO

Article History:
Received: 30 Aug. 2020
Accepted: 21 Sep. 2020

Keywords:
Oil spill
Sediment Analysis
Bandar Abbas
Fishing Port
Heavy metal

ABSTRACT

Bandar Abbas fish quays activities impacted on chemical compounds of the coasts. Three stations as Posht e Shahr (Ps), Sayadan (Sa) and Shilat (Sh) were selected to investigate the oil spill pollution and heavy metal concentrations in the regions. The sediment samples were collected in June and November 2017 then extracted. The highest concentrations were Fe>Zn> Pb>Cu>Cd respectively in the Sh quay. The cluster results indicated that Ni and Zn have the same sources but Pb, Cu and Cd were from different sources. Ni and Zn entered the environment due to the activities of ship repairs and coastal construction. Pb, Cu and Cd sources were from oil spills of fishing boats. The ERLQ and ERMQ toxicity rates of Ni at Ps and Sa were at the occasional but the Sh was at the frequent occurrence level. In November, the Cd toxicity at Sh was at occasional level. The new rules needed to control the pollution of quays operation.

1. Introduction

The Persian Gulf, which located at latitude of 24 ° to 30 °N and longitude of 47 ° to 57 ° E, is one of the most important waterways in the world. About 60% of the world's marine oil tanker transports via this area [1]. It is the third largest gulf in the world after the Gulf of Mexico and the Hudson Bay [2]. The concentration of elements in the sediment structure depends on their concentrations in the local environment and their bioavailability. That is why, in various studies, especially those having environmental, time and spatial limitations, they are used as indicators for environmental health assessments [3,4]. Metals are naturally found in aquatic environments, but their concentrations are increased recently, which have severe impacts on shallow coastal areas [5]. According to various studies, the concentrations of minor metals are influenced by many activities, and unique impacts on the concentrations, so they are known as the detectors [6,7]. The effects of various human activities can be measured by the concentrations of the minor metals which trapped in the sediments or the corals aragonite [8]. Bandar Abbas is the largest city and capital of Hormozgan Province in the north coast of the Persian Gulf. It is located in the south of Iran with GIS: 27 ° 18'32 "N 56 ° 26'66" E. The present study aimed to investigate the concentrations of the heavy metals around three fishing quays in Bandar Abbas city coastline. Due to the great amount of activities as boats and ship transportation it caused to release the oil into the sea water and sand coast on surrounded area which is effected on the chemical properties [9].

2. Materials and methodology

To determine the concentrations of heavy metals, three stations fisheries port, namely Posht e Shahr (Ps), Sayadan (Sa) and Shilat (Sh), were selected to collect the water and sediment samples. Table 1 shows the geographic coordinates of all three stations and Fig. 1 shows the stations location on the map.

Table 1: Sampling stations GIS, Study Location

Number	Station	E	N
1	Ps	56°15'3.11"	27° 9'57.46"
2	Sa	56°15'55.45"	27°10'3.17"
3	Sh	56°19'9.29"	27°10'51.33"

Field studies and sampling were conducted in two period of time: first in June and the second in November 2017. The samples were collected from the beach and surface sediment and water. Sampling was performed three times at each station. Each samples is collected by core grab and put into the PVC containers. The samples were transferred to the lab then freeze and prepared for the analysis. According to MOOPAM instruction in 1983 which is used for similar studies in this area, after drying the sediment, 0.2% of each bottle content was digested with hydrofluoric acid (HF) and nitric acid-chloride acid (1.4%) solution in teflon containers then homogenized and filtered [10]. Finally, 50 ml distilled water was added to them. The absorption of each metal was measured by using of the Flame Atomic absorption Spectrometer (M5, manufactured by Thermo Company).

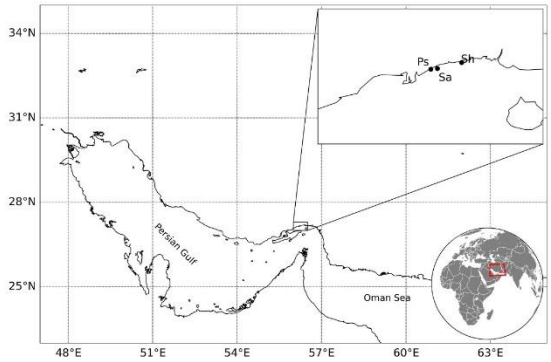

Figure. 1. Stations Location in Persian Gulf, Bandar Abbas coastline, south of Iran

Finally, the samples were distilled in 50 m of water [11] then extracted. The obtained values were analyzed by Minitab software. Moreover, One Way ANOVA test was used to compare the amount of different metals in the studied area [12]. Afterward, the Cluster K-Means technique is applied and the general statuses of the first metals were compared base on the clustering of each station, finally the heavy metals are classified. The dendrogram diagram was drawn according to the Cluster output that indicated which metals or stations had the same status or the same origin [13]. The Principal Component Analysis (PCA) was used to determine the first and second main components. The correlation coefficients between metals were defined by Pierson Coefficient and finally, the toxicity and the concentrations were compared according to the international standards [14].

3. Results

The analysis of the sediment samples data which obtained from the two sampling stages of the three coastal stations are shown in Tables 2, 3. Cadmium, lead, copper, zinc and nickel extracted.

Table 2:Heavy metals concentration (g/Kg Dry weight) for the three stations, June 2017

Station/Sample No		Cd	Pb	Cu	Zn	Ni
Ps	1	0.95	15.46	10.34	35.1	51.24
	2	1.09	17.76	8.48	29.73	44.22
	3	1.13	18.22	9.09	27.63	41.04
Sa	1	0.66	10.37	6.4	19.45	19.95
	2	0.79	6.65	7.98	37.13	19.97
	3	0.68	11.65	8.9	25.31	24.52
Sh	1	1.36	16.01	16.55	48.57	70.96
	2	1.64	16.75	19.16	51.4	66.17
	3	1.74	15.06	16.09	47.82	62.01
Maximum		0.66	6.65	6.4	19.45	19.95
Minimum		1.74	18.22	19.16	51.4	70.96
Average	**St.1**	1.06	17.15	9.3	30.82	45.5
	St.2	0.71	9.56	7.76	27.3	21.48
	St.3	1.58	15.94	17.27	49.26	66.38

Table 3:Heavy metals concentration (g/Kg Dry weight) for the three stations, November 2017

Station/Sample No		Cd	Pb	Cu	Zn	Ni
	1	1.03	17.02	9.33	25.46	48.07
Ps	2	0.91	18.21	9.12	27.31	51.23
	3	0.98	15.23	8.56	24.13	40.98
	1	0.58	9.89	7.02	26.13	23.06
Sa	2	0.88	8.24	7.11	24.03	21.25
	3	0.73	6.89	6.14	22.12	26.34
	1	0.98	14.12	13.21	39.89	68.76
Sh	2	0.95	13.69	18.14	41.06	65.89
	3	1.01	15.01	14.12	38.88	71.16
Maximum		0.58	6.89	6.14	22.12	21.25
Minimum		1.03	18.21	18.14	41.06	71.16
	St.1	0.97	16.82	9	25.63	46.76
Average	**St.2**	0.73	8.34	6.76	24.09	23.55
	St.3	0.98	14.27	15.16	39.94	68.6

3.1. One-way analysis of variance (One Way ANOVA)

The P-Value obtained for One Way ANOVA test related to the collected samples of June (R-sq = 72.42) and November (R-sq = 75.16) was 0.000. The results indicated that the concentrations of various metals were not the same. The results of Tukey's test showed that in both samples of Ps station in the June and November, Ni and Zn were placed in the first and Pb, Cu and Cd were in the second class. It should be noted that in one-way analysis of variance, those elements with similar behavior and source were in the same class.

Clustering

In terms of station

As shown in Figure 2, about the samples that collected in June, three repetitions of Sh and Ps stations were placed in the same cluster, but three repetitions of Sa Fish quay station were placed in a separate cluster. It indicated that Shilat (Sh) and Posht e Shahr (Ps) stations had the same statuses but Sayadan (Sa) had a different status.

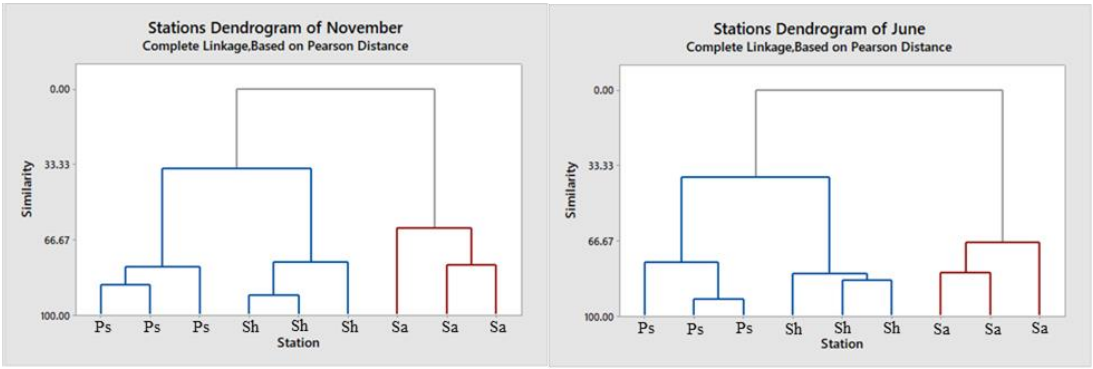

Figure. 2. Dendrogram of the Stations (Similar Data are in the Same Group)

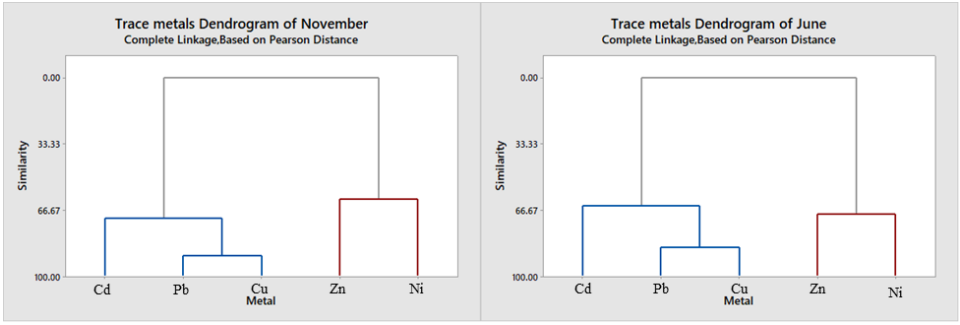

Figure. 3. Dendogram of the Metals (Similar Data are in the Same Group)

In terms of metal type

The results of the sample extract was consistent and compatible with the results of the Anova one-way analysis, represented by a dendrogram (Figure 3). The elements represented in one cluster are due to the same source.

Principal Component Analysis (PCA) chart:

The PCA graph, shown in Figure 4, illustrated which metals play a more important role, as well as the metals classification.

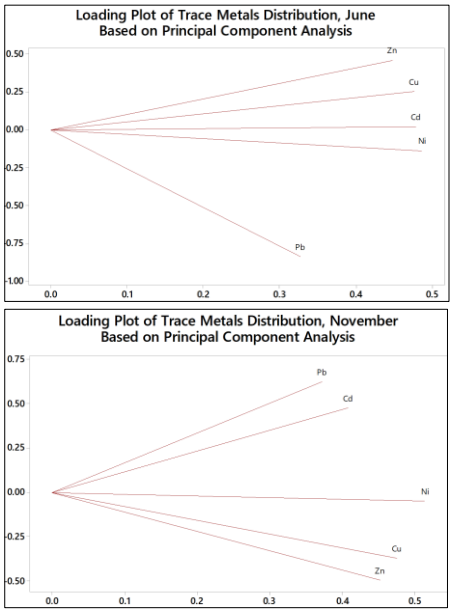

Figure. 4. Loading plot of Principal component for June and Nov samples

Correlation between metals using Pearson correlation coefficient

This coefficient is used to represent the correlation between the elements, the greater coefficient, and the stronger correlation. The correlation had a direct relation if the coefficient value is positive and negative for versa (table 4). In June the positive correlated is between Ni and Pb, Cu and Zn. The Negative correlated is between Cu and Cd, Zn and Cd, Pb. In November Cd with Cu, Zinc and Ni as well Ni with Zn are positive correlated and negative correlated with Pb and Cd.

Table 4: Correlation Coefficient of Pearson

Correlation: Cd, Pb, Cu, Zn, Ni, June

Correlations

	Cd	Pb	Cu	Zn
Pb	0.604			
Cu	0.895	0.450		
Zn	0.847	0.277	0.925	
Ni	0.884	0.723	0.892	0.827

Correlation: Cd, Pb, Cu, Zn, Ni, November

Correlations

	Cd	Pb	Cu	Zn
Pb	0.694			
Cu	0.545	0.423		
Zn	0.430	0.330	0.940	
Ni	0.712	0.681	0.876	0.876

Ecological Impact

Metal contamination in sediments may cause toxicity in sediment-dwelling organisms [15,16]. The effects-range low (ERL) and effects-range median (ERM) sediment quality guidelines [15] were used to characterize the potential toxicity of sediments due to their metal (Cd, Cu, Pb, Ni and Zn) contamination. Metal concentrations below the ERL, at or above the ERL but below the ERM, and at or above the ERM are associated with, respectively, Rare, occasional, and frequent occurrence of toxic effects. For each metal, two quotients namely the effects-range low quotient (ERLQ) and effects-range median quotient (ERMQ) were derived by dividing the measured metal concentration by its corresponding ERL and ERM concentrations, respectively. Within this approach, an ERLQ <1 indicated that toxic effects would Rarely occur; an ERLQ > 1 but ERMQ<1 indicated that toxic effects would occur occasionally; whereas an ERMQ > 1 indicated that toxic effects would occur frequently (Table 5-8) [17].

Table 5: Sediment quality, values of ERL, ERM (Lang et al., 1995), ISQG and PEL (CCME, 2002) (ppm in dry weight) and the relative percentages of biological (ERL: Effect Range Low& ERM: Effect Range Medium)

Substance	ISQG	ERL	PEL	ERM	%<=ISQ	<ERL	ISQ<%<PEL	ERL-ERM	%>=PEL	>ERM
Cd	0.7	1	4	10	6	7	20	37	66	71
Cu	18.7	34	108	270	9	9	22	29	56	84
Ni		21		52		2		17		17
Pb	30.2	47	112	218	6	8	26	36	58	90
Zn	124.0	150	271	410	4	6	27	47	65	70

Table 6: ERLQ values of metals for sediment of three stations, June 2017

Station/Sample No		ERLQ (Cd)	ERLQ (Cu)	ERLQ (Pb)	ERLQ (Ni)	ERLQ (Zn)
	1-1	0.8583333	0.2744118	0.362128	2.289048	0.169733
PS	1-2	0.7583333	0.2682353	0.387447	2.439524	0.182067
	1-3	0.8166667	0.2517647	0.324043	1.951429	0.160867
	2-1	0.4833333	0.2064706	0.210426	1.098095	0.1742
SA	2-2	0.7333333	0.2091176	0.175319	1.011905	0.1602
	2-3	0.6083333	0.1805882	0.146596	1.254286	0.147467
	3-1	0.8166667	0.3885294	0.300426	3.274286	0.265933
SH	3-2	0.7916667	0.5335294	0.291277	3.137619	0.273733
	3-3	0.8416667	0.4152941	0.319362	3.388571	0.2592
Average		0.7453704	0.3031046	0.279669	2.204974	0.199267
Total Average		0.7464768				

Table 7: ERLQ values of metals for sediment of three stations, November 2017

Station/Sample No		ERLQ (Cd)	ERLQ (Cu)	ERLQ (Pb)	ERLQ (Ni)	ERLQ (Zn)
	1-1	0.7916667	0.3041176	0.328936	2.44	0.234
PS	1-2	0.9083333	0.2494118	0.377872	2.105714	0.1982
	1-3	0.9416667	0.2673529	0.38766	1.954286	0.1842
	2-1	0.55	0.1882353	0.220638	0.95	0.129667
Sa	2-2	0.6583333	0.2347059	0.141489	0.950952	0.247533
	2-3	0.5666667	0.2617647	0.247872	1.167619	0.168733
	3-1	1.1333333	0.4867647	0.340638	3.379048	0.3238
Sh	3-2	1.3666667	0.5635294	0.356383	3.150952	0.342667
	3-3	1.45	0.4732353	0.320426	2.952857	0.3188
Average		0.9296296	0.3365686	0.302435	2.116825	0.238622
Total Average		0.7848162				

Table 85: ERMQ values of heavy metals, for sediment of three station, June 2017

Station/Sample No		ERMQ (Cd)	ERMQ (Cu)	ERMQ (Pb)	ERMQ (Ni)	ERMQ (Zn)
	1-1	0.107292	0.034556	0.077364	0.924423	0.062098
Ps	1-2	0.094792	0.033778	0.082773	0.985192	0.06661
	1-3	0.102083	0.031704	0.069227	0.788077	0.058854
	2-1	0.060417	0.026	0.044955	0.443462	0.063732
Sa	2-2	0.091667	0.026333	0.037455	0.408654	0.05861
	2-3	0.076042	0.022741	0.031318	0.506538	0.053951
	3-1	0.102083	0.048926	0.064182	1.322308	0.097293
S	3-2	0.098958	0.067185	0.062227	1.267115	0.100146
	3-3	0.105208	0.052296	0.068227	1.368462	0.094829
Average		0.093171	0.038169	0.059747	0.89047	0.072902
Total Average		0.230892				

Table 9: ERMQ values of heavy metals, for sediment of three station, November 2017

Station/Sample No		ERMQ (Cd)	ERMQ (Cu)	ERMQ (Pb)	ERMQ (Ni)	ERMQ (Zn)
Ps	1-1	0.0989583	0.0382963	0.070273	0.985385	0.08561
	1-2	0.1135417	0.0314074	0.080727	0.850385	0.072512
	1-3	0.1177083	0.0336667	0.082818	0.789231	0.06739
Sa	2-1	0.06875	0.0237037	0.047136	0.383654	0.047439
	2-2	0.0822917	0.0295556	0.030227	0.384038	0.090561
	2-3	0.0708333	0.032963	0.052955	0.471538	0.061732
Sh	3-1	0.1416667	0.0612963	0.072773	1.364615	0.118463
	3-2	0.1708333	0.070963	0.076136	1.2725	0.125366
	3-3	0.18125	0.0595926	0.068455	1.1925	0.116634
Average		0.1162037	0.0423827	0.064611	0.854872	0.087301
Total Average		0.233074				

4. Discussion and Conclusion

The result of one-way analysis of variance and Dendrogram (Fig. 3) of the cluster are indicated that Ni and Zn had the same sources but the Pb, Cu and Cd had different sources. It seems that Ni and Zn entered the environment due to the dispersed fishing tools, repairment and harbor construction. The Pb, Cu and Cd entered this area through oil spills release from fishing boats. According to the obtained clustering results in (Fig. 2), it seems that Posht e Shahr and Shilat stations were more impacted by similar activates as fishing, but Sayadan station was affected by various sources in addition to fishing boats, maintenances, dyeing, refueling and coastal construction. According to the results of the Principal Component Analysis (Fig. 10), it is observed that in the in June, Cu, Ni, and Zn are placed in the first principal component group (PCA1). Hence Pb and Cd are placed in the second principal component group (PCA2), and in the samples of November, all elements, except Pb, are placed in the first principal component group (PCA1) and Pb is placed in the second principal component group (PCA2). The results of Pearson correlation coefficient, clarified the highest correlation between Cu and Zn. As well as Cu with Cd in the samples of November were (0.925 and 0.895, respectively). This indicated a close relative between Cd and Zn with Cu which was again consistent with the results of one-way analysis and clustering. The ERLQ and ERMQ toxicity values indicated that in both sampling series, Ni pollution at Ps and Sa stations was at the occasional level and at station Sh, it was at the frequent occurrence level. Moreover, in November, Cd toxicity was at the occasional level at Sh station. Pollutions of all other elements were at the rare level, which proved that there was no risk. Only Ni toxicity was at the occasional level, and the average toxicity of other metals were at the rare level. Based on the results and local observations, it is clear that the fishing boat activities, which cause to release oil and gasoline spills are the main source of the dispersion of heavy metals as Ni and Pb in these three stations. Additionally, various fishing tools and equipment as well as metal wastes are also the sources of Fe and Cd in such ports. Moreover, due to the direction of prevailing wind in this region which is from south west, the floated oil spills on the water surface were transferred to the eastern coast of Bandar Abbas. The weathered spills are trapped within sand and increased the concentration of heavy metals in the coastal port sediment in this area [18]. In general, it is necessary to develop more rules by local law enforcement agencies and prevent of oil release through boats. As well making a suitable place regarding to the environmental protection issues for the solid wastes and unused instruments in these areas would reduce the leave or accumulation of these substances in the sea and coast. A new standard instruction according to the environment is very effective for the ships and boats discharge.

Acknowledgment

The authors and researchers of this study would like to thank the Department of Environment, Hormozgan Province, Bandar Abbas and their skilled lab personnel for providing the laboratory materials and guidance at all stages of testing and analysis of the samples.

5. References

1-Reynolds, R.M. (1993) Physical oceanography of the Gulf, Strait of Hormuz, and the Gulf of Oman—Results from the Mt Mitchell expedition. Marine Pollution Bulletin 27, 35-59.

2-Hajrasouliha, O., Hassanzadeh, S. (2015) The impact of wind stress in modeling of oil pollution diffusion in the Persian Gulf. Journal of Bioremediation & Biodegredation 6, 1.

3-Saeedi, M., Hosseinzadeh, M., Jamshidi, A., Pajooheshfar, S. (2009) Assessment of heavy metals contamination and leaching characteristics in

highway side soils, Iran. Environmental monitoring and assessment 151, 231-241.

4-Saha, N., Webb, G.E., Zhao, J.-X. (2016) Coral skeletal geochemistry as a monitor of inshore water quality. Science of The Total Environment 566, 652-684.

5-Monikh, F.A., Peery, S., Karami, O., Hosseini, M., Bastami, A.A., Ghasemi, A.F. (2012) Distribution of metals in the tissues of benthic, Euryglossa orientalis and Cynoglossus arel., and Bentho-Pelagic, Johnius belangerii., Fish from three estuaries, Persian Gulf. Bulletin of environmental contamination and toxicology 89, 489-494.

6-Jiang, W., Yu, K.-F., Song, Y.-X., Zhao, J.-X., Feng, Y.-X., Wang, Y.-H., Xu, S.-D. (2017) Coral trace metal of natural and anthropogenic influences in the northern South China Sea. Science of The Total Environment 607, 195-203.

7-Nguyen, A., Zhao, J., Feng, Y., Hu, W., Yu, K., Gasparon, M., Pham, T., Clark, T. (2013) Impact of recent coastal development and human activities on Nha Trang Bay, Vietnam: evidence from a Porites lutea geochemical record. Coral Reefs 32, 181-193.

8-Tarek Abdel-Aziz M. A., Dar, Mahmoud A. (2009) Ability of corals to accumulate heavy metals, Northern Red Sea, Egypt. Environ Earth Sci (2010), 59: 1525-1534.

9-Tornero, V., Hanke G. (2016) Chemical contaminants entering the marine environment from sea-based sources: A review with a focus on European seas, Marine Pollution Bulletin 112, 17–38.

10-Badri, M., Aston, S. (1983) Observations on heavy metal geochemical associations in polluted and non-polluted estuarine sediments. Environmental Pollution Series B, Chemical and Physical 6, 181-193.

11-MOOPAM, M.J.R.O.f.t.p.o.M.E. (1983) Manaul of Oceanographic Observation and Pollution Analysis.

12-Tabari, S., Saravi, S.S.S., Bandany, G.A., Dehghan, A., Shokrzadeh, M.J.T., health, i. (2010) Heavy metals (Zn, Pb, Cd and Cr) in fish, water and sediments sampled form Southern Caspian Sea, Iran. 26, 649-656.

13-Alkarkhi, A.F., Ismail, N., Ahmed, A., Mat Easa, A.J.E.m., assessment (2009) Analysis of heavy metal concentrations in sediments of selected estuaries of Malaysia—a statistical assessment.

14-Sekabira, K., Origa, H.O., Basamba, T., Mutumba, G., Kakudidi, E.J.I.J.o.E.S., Technology (2010) Assessment of heavy metal pollution in the urban stream sediments and its tributaries. 7, 435-446.

15-Long, E.R., Macdonald, D.D., Smith, S.L., Calder, F.D.J.E.m. (1995) Incidence of adverse biological effects within ranges of chemical concentrations in marine and estuarine sediments. 19, 81-97.

16-Long, E.R.J.E.S., Technology (2006) Calculation and uses of mean sediment quality guideline quotients: a critical review. 40, 1726-1736.

17-Botwe, B.O., Alfonso, L., Nyarko, E., Lens, P.N.J.E.E.S. (2017) Metal distribution and fractionation in surface sediments of coastal Tema Harbour (Ghana) and its ecological implications. 76, 514.

18-Farzingohar, M., Ibrahim, Z.Z., Yasemi, M.J.I.J.o.F.S. (2011) Oil spill modeling of diesel and gasoline with GNOME around Rajaee Port of Bandar Abbas, Iran. 10, 35-46.